System and Media Optimizations for improved HAMR Performance

A DISSERTATION

SUBMITTED TO THE FACULTY OF THE GRADUATE SCHOOL

OF THE UNIVERSITY OF MINNESOTA

BY

NIRANJAN NATEKAR

IN PARTIAL FULFILLMENT OF THE REQUIREMENTS

FOR THE DEGREE OF

DOCTOR OF PHILOSOPHY

ADVISER: RANDALL H. VICTORA

AUGUST 2020

Acknowledgements

The journey of attaining a PhD is like a marathon, not a sprint. And just like an athlete who wishes to finish the marathon successfully needs a good coach, a graduate student hoping to finish his PhD needs a PhD adviser who will guide him successfully towards his goal. In addition to a good adviser, he needs a support system that would encourage him to keep going every time the PhD research journey takes an unpleasant detour.

First and foremost, I would like to thank my PhD adviser, Prof. Randall H. Victora, who has been incredibly supportive and patient in helping me wade the murky and complicated waters of research. His interminable knowledge in the field of magnetism and data storage coupled with his ability to explain complex concepts in a simple way has helped me simplify difficult problem statements to find solutions. At the same time, he has always allowed me to make mistakes, encouraged me to learn from them and provided advice that would prove immensely helpful in the future as I become a part of the data storage industry. It has been an honor and a privilege to be his student.

As a student at the University of Minnesota, I have been lucky to have the company of several exceptional professors who have been an integral part of my research as well as academic coursework. I would like to thank Prof. Jian-Ping Wang, Prof. P. Paul Ruden and Prof. Jasmine Foo for taking out the time to be a part of my PhD defense committee and guiding my thesis. I would also like to thank Prof. Beth Stadler for her help and advice especially during the PhD qualification exams.

I have enjoyed the company of several professional colleagues who have contributed to my research in different ways as well as kept me company. I would like to thank these colleagues, Wei-Heng Hsu, Aneesh Venugopal, Dr. Tao Qu, Yijia Liu, Kun Xue, Dr. Rizvi Ahmed, Dr. Ali Ghoreyshi, Dr. Yipeng Jiao, Dr. Zengyuan Liu and Dr. Pin-Wei Huang who have all been a part of the MINT center. I would also like to thank my

colleagues from other research groups, Karthik Srinivasan, Joseph Um, Reza Zamani and Dr. Kai Wu.

The one set of people who have been my companions since day one of this journey is my fiancé, my family and my in-laws. My fiancé, Aditi Bapat has especially played an important role in helping me sustain the momentum of research and my confidence especially in difficult situations. I have been lucky to have these people by my side in this arduous journey.

Finally, I would like to thank my friends, Surabhi Talele, Abhishek Sathe, Ketaki Katdare, Siddhee Sahasrabudhe, Ninad Diwanji, Shruti Mahale, Rahul Mhatre, Saloni Rokde, Kunal Garde, Soniya Mantri and Vamsi Yadav Chavali who have always stood by me during the time I pursued my PhD at the University of Minnesota.

Dedication

With gratitude to my beloved parents, fiancé and my family

Abstract

It is said that data never sleeps. It has a ubiquitous presence and is being generated at an exceptional pace from different sources. The insurmountable demand for data must be met with an equally fast paced data supply which has led to the development of data servers by companies like Microsoft and Google. In spite of facing an existential crisis due to the development of SSD's, the Compound Annual Growth Rate (CAGR) of ~ 40% maintained by the HDD industry has ensured that these devices are a necessity when it comes to large scale data storage. The growth of the HDD industry is helped by the fact that a huge amount of research is dedicated to developing new data recording technologies to improve the storage capacity of HDD's. Significant investment has gone into developing a new data recording technology called Heat Assisted Magnetic Recording (HAMR) that is expected to improve the storage density up to at least 5Tb/in^2. In conjunction with other improvements (like the development of Bit Patterned Media BPM), the expected density output for HAMR can be even higher.

The optimization of the HAMR technology has focused on different aspects of the HAMR system, optical, magnetic, mechanical and electrical. In this thesis, different system and media optimizations that may help improve the HAMR performance are explored. The effect of doped $L1_0$ FePt media, which is an extremely popular HAMR media, is considered to understand how a change in its Curie temperature (T_c) can actually influence its intrinsic magnetic properties. This is followed by the implementation of micromagnetic simulations with the use of the stochastic Landau Lifshitz Gilbert (LLG) equation that is used to mimic the magnetization dynamics of grains. These simulations are used to vary the media properties and HAMR process parameters to optimize a thin 3nm (write layer)/6nm (storage layer) Thermal Exchange Coupled Composite (ECC) HAMR media. Introducing finite exchange coupling between the grains of the write layer and scaling the damping in the write layer are techniques that can help reduce the DC noise and improve the Signal to Noise Ratio (SNR). The Ensemble Waveform Analysis technique identifies Transition SNR as the main cause of

SNR variation. This optimization process lends credence to the idea that a thinner composite media may be used to realize significant enhancements of SNR. Micromagnetic simulations are also used to address an important issue related to HAMR; the high temperature for writing data can cause heating issues with long term HAMR use. A low temperature Thermal ECC media is proposed that can significantly reduce the writing temperature (by about 34%) and that can reduce the peak temperature of the heat spot used to heat the media in the HAMR process by 200K.

This is followed by an analytical formulation that is derived to calculate the transition jitter in the HAMR process. The jitter is known to depend on the grain size as well as the heat spot thermal gradient. It also depends on the Voronoi Grain Size Distribution, as well as exhibiting a surprising nonlinear dependence on the reader width. By combining the noise due to these dependencies the analytical formulation can be derived. This simple formulation provides both physical insight and conserves computational time relative to lengthy (and complex) recording simulations. A detailed analysis of the Adjacent Track Erasure (ATE) in the HAMR process is also explored. The numerical extent of ATE in different HAMR media is established and techniques are implemented using micromagnetic simulations in an attempt to reduce the ATE effect. A hypothesis is established to explain the presence of extent of ATE in different HAMR media.

Research in the area of HAMR process and system optimization is of huge importance especially since the data storage industry has invested a lot in terms of research and manpower in this technology. Potential directions of research include techniques to reduce the ATE, improving the designs of different HAMR system components and developing better data post processing techniques like Neural Networks and 2D detectors.

Contents

List of Tables

List of Figures

Chapter 1

Introduction

The idea of generation and storage of data has been around since a long time almost since the first computer (the Electronic Numerical Integrator And Computer ENIAC) was developed in 1946[1]. The first computer occupied about 1,800 square feet and used about 18,000 vacuum tubes, weighing almost 50 tons. The earliest computers did not have any storage capacity. Programs had to be entered manually to run them and this generated the idea of permanently storing data using the power of computers. The most primitive form of data storage was paper tapes where programs and data were recorded using holes punched into paper tapes or punch cards to represent a "1", and paper blocks to represent a "0" (or vice versa)[2]. This type of storage was used for many years until the creation of magnetic tapes. This was discarded quickly when the need to access data randomly (and not sequentially) was felt. Disk drive development was impacted massively when IBM announced, in May 1955, a product that offered unprecedented random-access storage to 5 million characters each with 6 bits[3].

The amount of data generated every day is hard to quantify due to the innumerable sources and forms of data. Just to illustrate the magnitude of data being generated every day, it is predicted that the popular social media website Instagram has users posting about 50,000 photos per minute, about 15 million text messages are exchanged every minute and Google conducts about 3.6 million searches every minute[4]. Fig 1.1 shows the expected size of the global datasphere which is expected to reach 175 ZB by 2025[5][6]. Fig 1.2 gives an illustration of the amount of data generated every day[7]. It is clear that companies and individual users need cheap modes of data storage to ensure that vast amounts of data can be stored and accessed without any issues.

From the very first disk drive design, the development of Hard Disk Drive (HDD) designs and capacities today has been stupendous. Today, HDD's are commonly used in

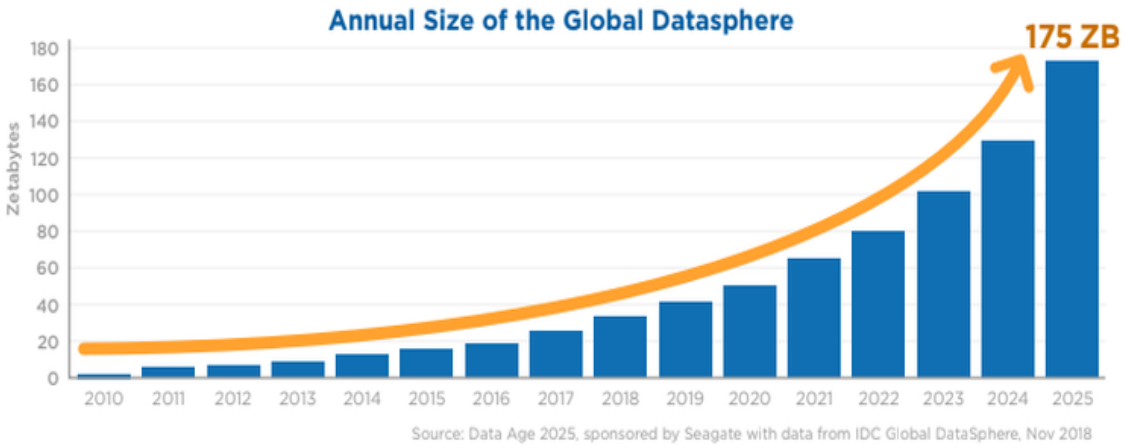

Fig. 1.1 Size of the global datasphere[5][6]

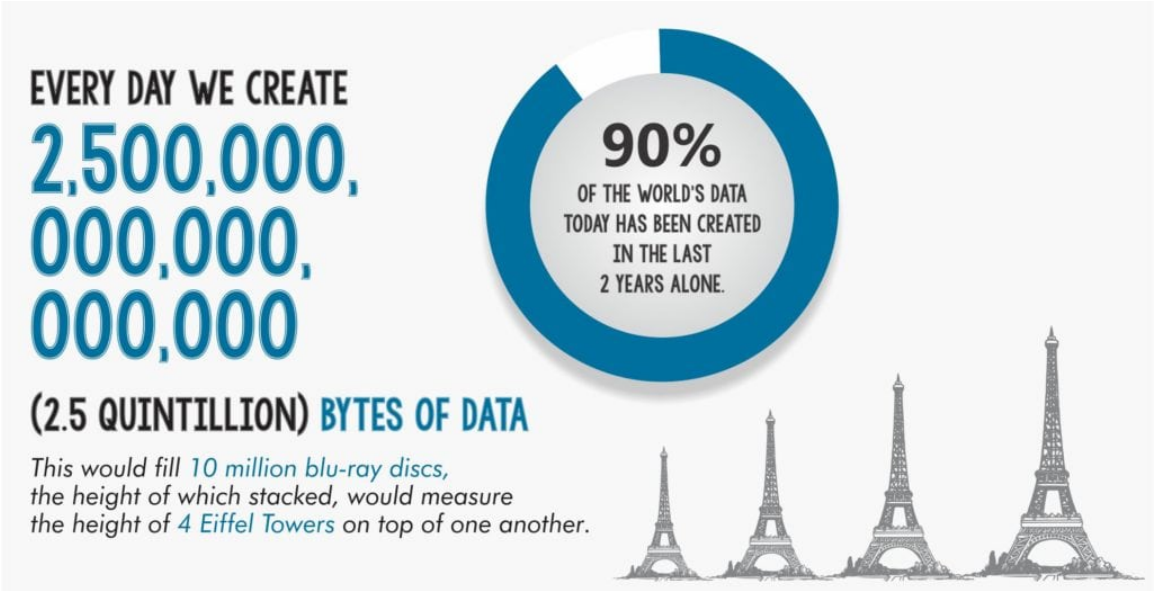

Fig. 1.2 Approximate global data generated everyday[7]

personal computers, laptops and even in data servers. Their importance has amplified since the development of cloud services by companies like Google and Amazon (via Amazon Web Services). Although the increasing use and development of the Solid State Drive (SSD) provides a threat to the existence of HDD's in the future, the decreasing cost/bit for stored data has made the use of HDD's inevitable. Fig. 1.3 shows the

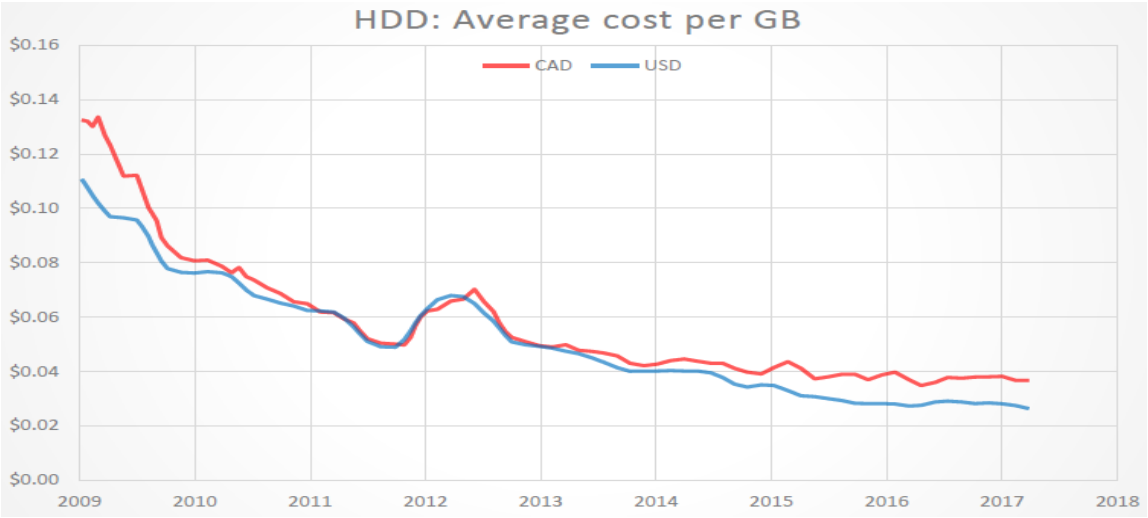

Fig. 1.3 Variation of average HDD cost/GB over the years[8]

decreasing cost of HDD data storage [8]. It is clear that compared to SSD's, the cheap cost of data storage is an advantage for HDD's ensuring their longevity in the coming times.

1.1 Hard Disk Drive Development

The history of HDD development is replete with examples of technologies developed solely to address individual issues identified at different timepoints. The need for permanent storage of data led to the introduction of HDDs in 1956 as data storage devices for an IBM real-time computer. The first IBM drive, the 350 RAMAC was approximately the size of two refrigerators and stored 5 million 6-bit characters (the equivalent of 3.75 million 8-bit bytes) on a stack of 50 disks[3][9]. This was followed by IBM introducing the 1311 disk drive in 1961. This drive was huge and stored about two million characters on a removable disk pack. Additional disk packs could be bought and interchanged with the current disk pack as needed, much like reels of magnetic tapes. Later models of removable pack drives, from IBM and others, became the norm in most computer installations and reached capacities of 300 megabytes by the early 1980s. Non-removable HDDs were called fixed disk drives. In 1973, IBM introduced a new type of HDD code-named "Winchester"[10]. Its primary feature was that the disk heads were not

withdrawn completely from the stack of disk platters when the drive was powered down. Instead, the heads were allowed to "land" on a special area of the disk surface upon spin-down, "taking off" again when the disk was later powered on. This reduced the head actuator mechanism cost but precluded removing just the disks from the drive as was the norm during that period. Later "Winchester" drives abandoned the removable media concept and returned to non-removable platters. A few years later, designers were exploring the possibility that physically smaller platters might offer advantages. Drives with non-removable eight-inch platters appeared, and then drives that used a 5 1⁄4 in (130 mm) form factor (a mounting width equivalent to that used by a floppy disk drive. The latter were primarily intended for the then-fledgling personal computer (PC) market. By the late 1980s, HDD costs had been reduced to the point where they were standard on all but the cheapest PC. Most HDDs in the early 1980s were sold to PC end users as an external, add-on subsystem. The IBM PC/XT in 1983 included an internal 10MB HDD, and soon thereafter internal HDD's proliferated on personal computers[3].

Today, HDD's have captured different market segments based on their use and capacity. Desktop HDD's typically store between 60 GB and 8 TB and have a data transfer rate of 0.5 Gbit/s or higher. These HDD's are typically about 3.5" in diameter and as of May 2019, the highest-capacity desktop HDD's stored 14 TB[11] with Western Digital planning to release 16 TB and 18 TB MAMR drives as well[12]. As of 2016, the typical speed of a hard drive in an average desktop computer is 7200 RPM, whereas low-cost desktop computers may use 5900 RPM or 5400 RPM drives. On the other hand, laptop and mobile HDD's are typically smaller and contain lesser number of platters to store data. Thus, their capacities are relatively much lower. Laptop drives are typically 2.5" in size and their capacity can range from 160 GB to more than 2 TB. Most laptop systems will have between 500 GB and 1 TB of storage. Finally, Enterprise HDD's are used with multi-user computers which may handle enterprise software like transaction processing databases, internet infrastructure (email, webserver, e-commerce) and scientific computing software. These have to operate continuously with reliability and high performance being the most important features. Maximum capacity is not a goal, hence

these drives are typically low capacity drives (3.5 TB – 4 TB) with respect to their high costs.

In 2018, there were about 912 exabytes of combined HDD/SSD data that was shipped. About 800 exabytes was shipped with the use of HDD's. That means about 89% of the data was shipped using spinning platters. The International Data Corporation (IDC) has predicted 22 ZB of new storage capacity will ship in between 2018-25. Of this, hard disk drives will make up approximately 60%. This amounts to about 13 ZB of additional HDD capacity entering the supply chain. The vast majority of that total (approximately 90%) will ship between 2020 and 2025[5]. Thus, it is unsurprising that HDD's will continue to dominate. Although the emerging SSD usage in different applications has offered a strong competition for HDD's, Fig. 1.4 shows the clear capacity advantage that HDD's enjoy over SSD's. It is clear that considering the cost/bit value, SSD's remain prohibitively costly (at least four to five times[13][14]). Additionally, although as of 2016, HDDs are reported to have a failure rate of 2–9% per year, while SSD's have fewer failures: 1–3% per year, SSD's have more uncorrectable data errors than HDD's[15].

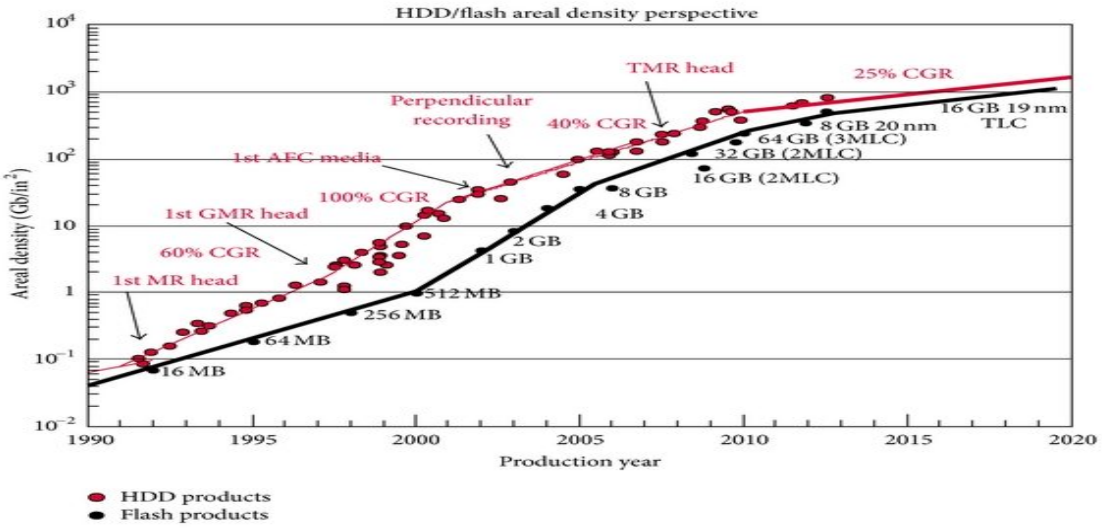

Fig. 1.4 Comparison of Areal Density values for different product technologies[16][17]

The growth in the use of HDD's has been primarily due to technologies that have been developed by the industry to improve the HDD performance, the data retention

capability/stability as well as the development of materials and fabrication processes that have allowed the cheap proliferation of HDD's. Fig. 1.5 shows the improvement in the storage capacity of HDD's by employing various recording technologies. The CAGR up to 2007 was maintained to about 60%. Even though the predicted capacity growth rate has slowed down to 30%, the trend of developing exciting new technologies has improved the morale of the industry. In 2007, Albert Fert and Peter Grunberg were awarded the Nobel Prize for the development of the Giant Magnetoresistance (GMR) that can be used for readback of recorded data[18][19][20][21]. This helped improve the readback sensitivity and allowed the generation of better recorded signals. Before 2005, the most common recording technology used was called Longitudinal Magnetic Recording (LMR). As can be clearly seen in Fig. 1.5, the saturation of Areal Density (AD) values with this technology to about 130 Gb/in^2 gave an impetus to the development of the Perpendicular Magnetic Recording (PMR) technology. Although there have been significant improvements with the use of PMR, there is yet again a clear saturation of AD values around 1.0Tb/in^2. Magnetic storage technologies are being developed to address the magnetic recording trilemma (explained later) and compete with flash memory–based solid state drives (SSD's).

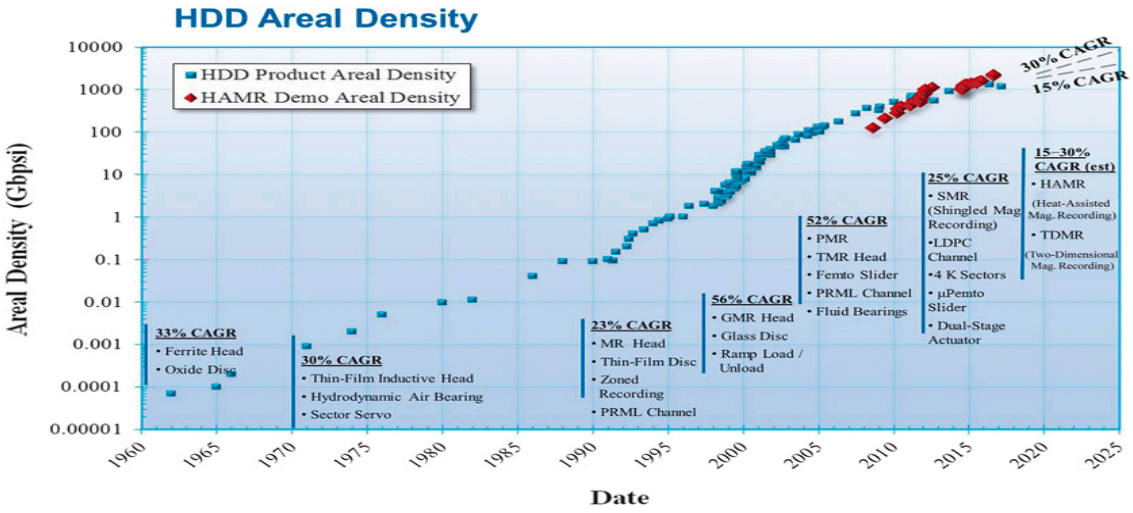

Fig. 1.5 HDD Areal density improvement trend with different recording technologies[22]

In 2013, Seagate introduced shingled magnetic recording (SMR)[23][24][25], intended to be an improvement over PMR before the eventual development of the intended successor of PMR: Heat-Assisted Magnetic Recording (HAMR). SMR utilizes overlapping tracks for increased data density, at the cost of design complexity and lower data access speeds. Western Digital focused on developing helium filled disk drives, to reduce turbulence and friction inside the disk drive during their operation and fit more platters into the same enclosure space. The development of HAMR is an extremely important step in the progress of the HDD industry, as can be seen clearly from Fig. 1.6, that shows the ASTC (Advanced Storage Technology Consortium) predicted capacity roadmap for different technologies.

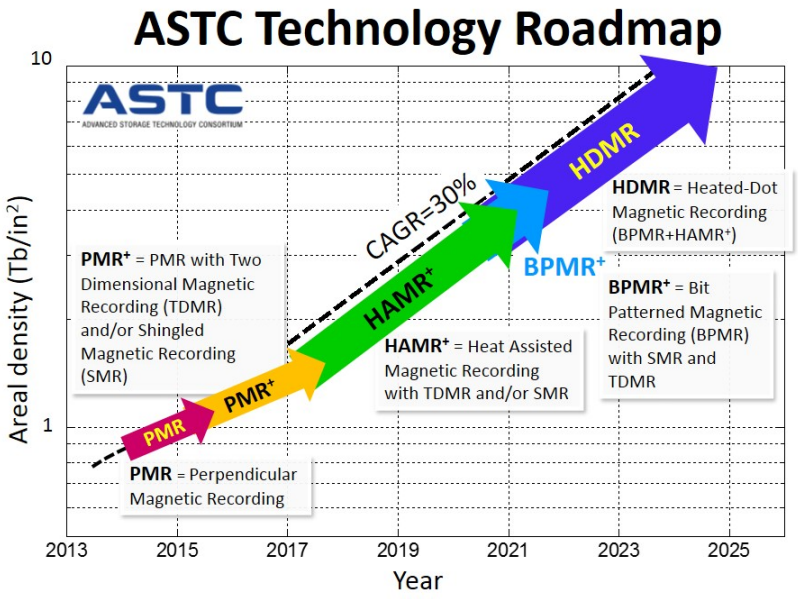

Fig 1.6 ASTC roadmap targeting Areal Densities in the near future[26]

HAMR requires the development of new architecture including a new optical delivery system (including lasers and Near Field Transducers (NFT)), new designs of magnetic media as well as a post processing system. While technical issues have delayed the commercial release of HAMR technology[27][28], the first HAMR drives are expected to ship around the end of 2020-early 2021[29][14]. Western Digital is also expected to ship the first Microwave Assisted Magnetic Recording (MAMR) drives sometime in

2021[30]. Additionally, Western Digital has itself been investing in HAMR development (to the tune of $500 billion, according to reports[5]) alongside its MAMR initiative. Fig 1.7 shows the clear consolidation of the data storage industry market. Although there are several players competing to improve their standing, there are primarily three significant powerhouses that have established their existence via mergers and acquisitions: Seagate, Western Digital and Toshiba. These companies (mainly Seagate and Western Digital) are providers of cloud storage. Toshiba, Seagate, and Western Digital are targeting the cloud data center as the prime area for capacity HDD growth in the coming years. By 2025, approximately half of the world's stored data will live in the public cloud, according to Seagate/IDC's research.

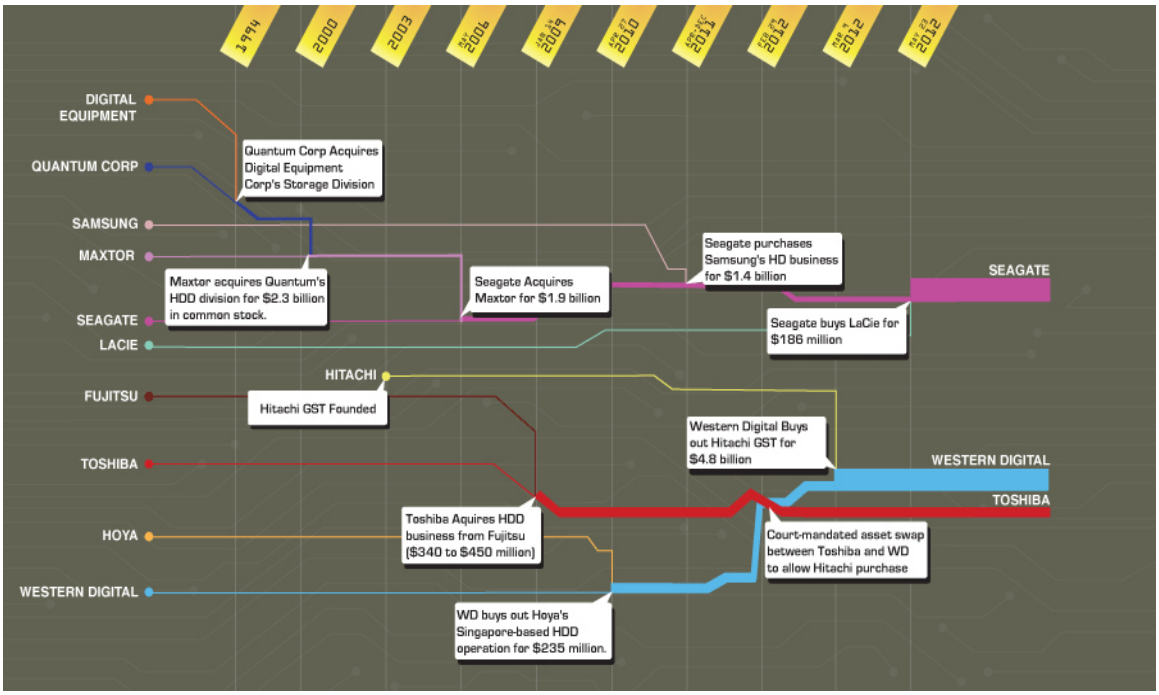

Fig 1.7 Current HDD market situation. Only three companies rule the entire HDD market[31]

1.2 Hard Disk Drive Control System

In the modern HDD design, data is recorded on the magnetic disk surface (media) which is a ferromagnet. The disks are arranged in the form of circular platters which are

nonmagnetic and these platters are coated with magnetic materials and often protected with a carbon (or a diamond like carbon) overcoat. Data is written in the form of binary bits that represent sequential magnetization changes. Due to the presence of errors during the data storage and readback process, data recovery is often aided with the use of Error Correction Codes. Fig 1.8 shows an example of a digital recording channel where data is encoded with different Run Length Limited (RLL) schemes used to encode the data before recording and detecting it. This encoding decides how data is represented in the magnetic transitions. Data is recorded on the magnetic surface as these surfaces rotate and pass through read and write heads that can detect the written data and change the data written on the disk surface.

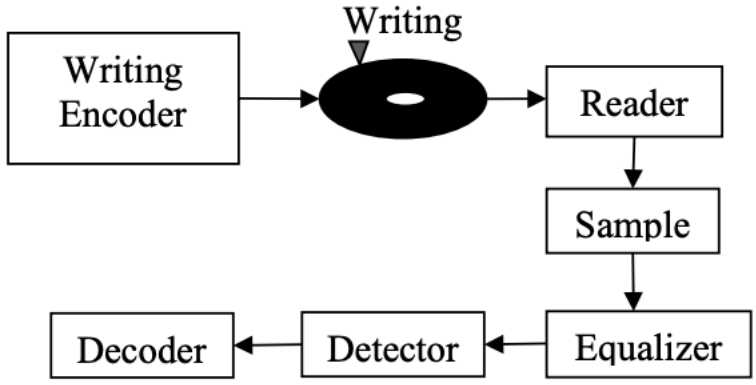

Fig. 1.8 Schematic of a digital recording channel[32].

Fig. 1.9 shows the mechanical structure of the Hard Disk Drive. The cover and base casting are important components of the structure that ensure the longevity of the disk drive operation by keeping the environment free of contaminants and dust particles that may affect the disk operation and reduce the head-media spacing. The base casting also provides support to other components like the spindle and actuator[2]. The actuator assembly consists of a Voice Coil Motor (VCM), data flex cable or printed circuit cable, actuator arms and crash-stops at both ends of travel. The data are read/written from/to the platters using the R/W heads mounted on the top and bottom surfaces of each platter. The read and write heads are supported by the actuator arm. The read/write heads are mostly magnetoresisitive heads (especially in the modern disk drives) that convert a change in

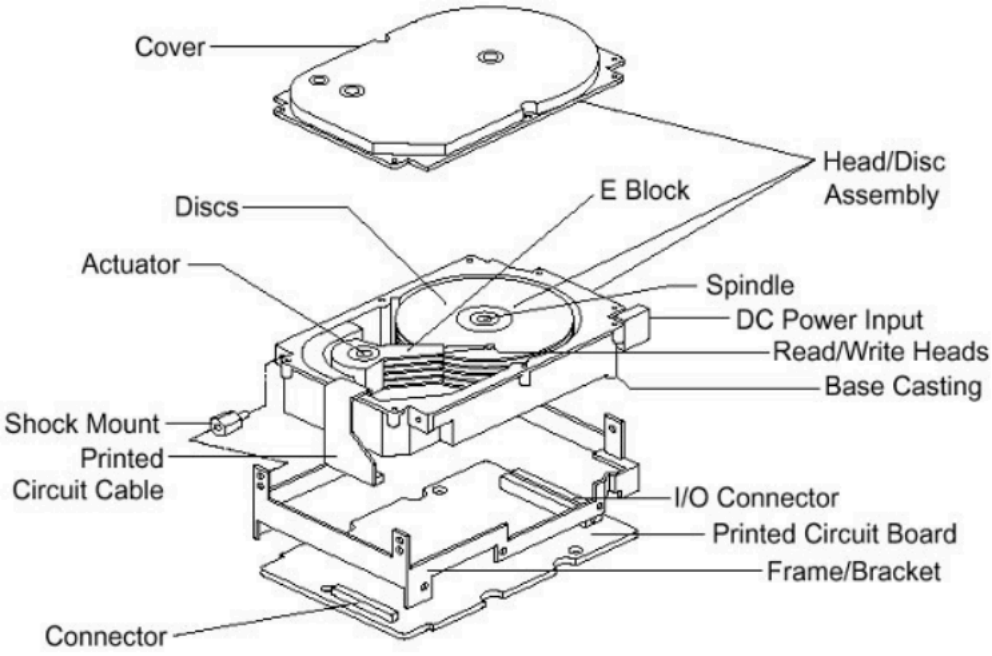

Fig 1.9 Typical mechanical structure of Hard Disk Drive[2]

the magnetoresistance (MR) into an electrical signal. Modern HDDs use separate heads for read and write operations. These heads are positioned a few nanometers above the recording medium on an air-bearing surface, which is referred to as a slider. A gimbal attaches the slider to a stainless steel suspension to allow for pitch and roll. The spindle and motor assembly is responsible for turning the hard disk platters with stable, reliable and consistent turning power for thousands of hours of often continuous use. Finally, the PC electronics card provides an interface connect different electronics to the host personal computer (PC). The most common interfaces used are the Integrated Drive Electronics (IDE), the Advanced Technology Attachment (ATA), and the Small Computer Systems Interface (SCSI), which all use integrated electronic circuits[9].

When the HDD receives a read or write request from the operating system, the VCM rotates the swing arm and keeps the magnetic head over the desired track[33]. In this time, the required accuracy in positioning the magnetic head at the track is usually less than 10% of the track pitch, the distance between two adjacent tracks. If this requirement is violated (leading to a position error), the HDD has to wait, for reading or writing data,

until the disk rotates one more time. This produces an undesirable operation delay in the computer system. Thus, the position of the head is a critical variable and the HDD system is a critical system. The operation of positioning a head is divided into two phases: track seeking and track following. In the seeking phase, the head is accelerated or decelerated by the VCM and moved to the target track as quickly as possible. The control in this phase is called the seek control. In the following phase, the head is maintained over the track by position control until the system finishes reading or writing data. The control in this phase is called the following control. When the HDD system receives a request signal for reading or writing data from the operating system, the following control is performed after the seek control. If the data is fragmented and stored in several different tracks, this control sequence repeats until the data is completely read from the disk. The mechanical part of the system, including the VCM and the swing arm, is a continuous-time system, while the controller is a discrete-time system since it is implemented digitally. In this sense, an HDD system is a sampled data system[33].

There can be several sources of disturbances in the normal HDD operation. Fig. 1.10 summarizes the possible error sources[2]. They can be classified into three categories: input disturbance, output disturbance and measurement noise. The input disturbance is typically due to an electronic bias superimposed with energy arising from the natural frequencies of the various mechanical perturbations such as resonances, vibrations and friction. The output disturbance is due to spindle rotation and its effects such as runout, windage and media noise. The measurement noise is a typical white noise due to the position-measurement techniques and/or sensors. A good HDD system has not only the desired track-seeking and following performance, but also the ability to overcome the different kinds of noise stated above. Fig. 1.11 shows a good way to model the different disturbances in the HDD system.

Many external factors can cause a disk failure, including power loss, magnetic interference, virus/malware, or environmental contamination that causes a head crash. HDD reliability is concerned with internal threats to the HDD, including equipment

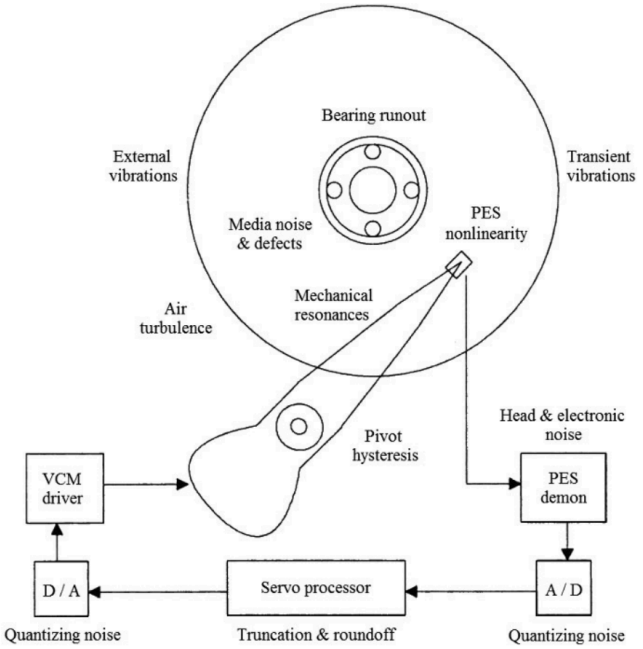

Fig 1.10 Error sources in a HDD system[2]

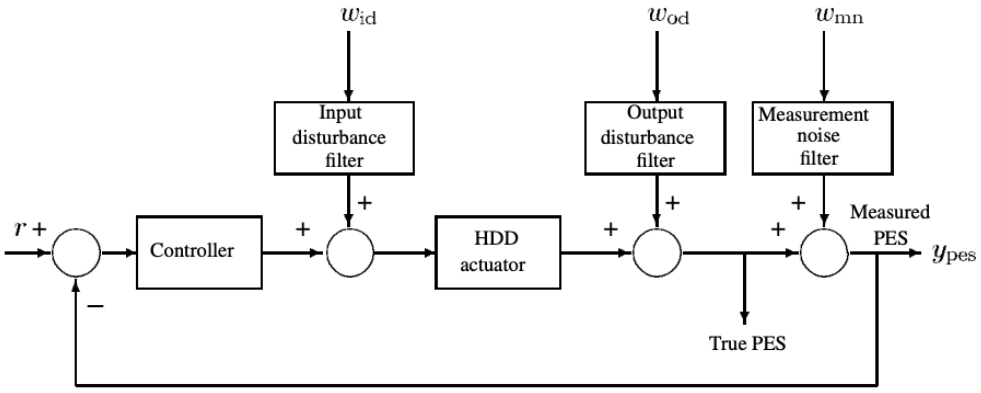

Fig. 1.11 Noise model for different noise sources in a mechanical HDD system[2]

failures, data errors, and head crashes. Sometimes drives fail because of wear and tear or poor manufacturing quality. Drive manufacturers report their drives reliability using mean time between failures (MTBF) or annualized failure rates (AFR)[34]. A head crash is another common cause of drive failure. It occurs when the read/write heads touch or scrape the platter surface. Several factors can damage the heads causing head crashes: power loss, motor failure, concussive shock, dust particles that make it through the air

filter, wear and tear from aging, or subpar manufacturing. Scratch damage and particles from damaged heads or platters create bad sectors, which can severely damage a disk and its data. Data errors can be another example of a cause leading to operation failure. Each sector on a hard disk contains 512 bytes of user data, or 4096 bits. These bits are subject to errors, some of which are identifiable by the OS or firmware; others are undetectable until the HDD fails. Error correction codes may be used to protect against these errors to some extent. When the read head reads back the user data, these codes use the read and the correction bits to report any errors to the controller for possible correction.

1.3 Magnetic Recording Technologies

Longitudinal Magnetic Recording (LMR) was the earliest magnetic recording technology that attempted to record data permanently on a HDD surface[35]. Fig 1.12 shows the recording process. An inductive 'ring' head is used to generate magnetic field with the help of an electromagnet to magnetize the media. As can be seen from the figure, the magnetizations with this technique settle in-plane and the fringing field between the two poles (P1 & P2) is used to record on the media. As the write head is passing over the media, the recording process starts and ends once the head passes completely over a spot. Thus, the recording happens due to the field from the trailing edge of the write head.

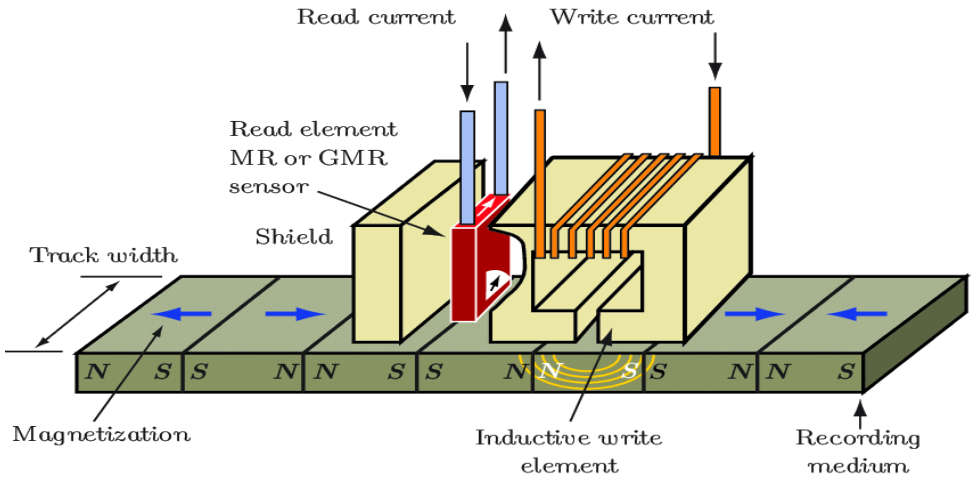

Fig. 1.12 Schematic for the Longitudinal Magnetic Recording (LMR) process[36]

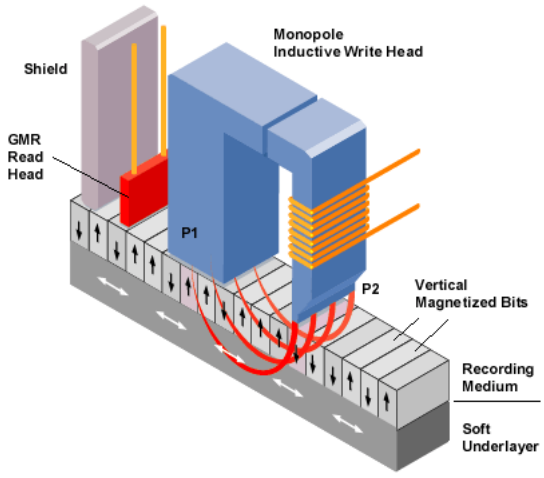

Fig 1.13 Schematic for the Perpendicular Magnetic Recording (PMR) process[37]

Since the fringing field is far less than the field in the gap (about one third of the field in the gap), large fields are required to magnetize the media (overcome the coercivity) and write the data. Since the written magnetizations settle in-plane, as the linear density increases, the distance between the magnetic poles or charges decreases leading to a strong demagnetization effect. Although advances were made in terms of the storage capacity for LMR media due to the development of oriented media[38][39] or Anti-Ferromagnetically Coupled (AFC) media[40][41][42] the demagnetization effect is severe in this technology. Thus the LMR technology faces severe limits[43][44][45][46] in terms of available recording field that limits the maximum storage capacity to about 130 Gb/in^2. The need to increase the storage density beyond this value led to the development of Perpendicular Magnetic Recording (PMR) as a new generation technology in 2005[47][48][49][50]. The major difference between PMR and LMR is the direction in which magnetizations settle for the individual grains. In case of PMR, magnetizations settle perpendicular to the plane of recording. In this case, even at high densities, the demagnetization field is minimal. PMR has also advanced significantly due to the development of fabrication processes for media like CoCrPt-SiO_2 and the development of the Soft Underlayer (SUL)[51][52]. Fig 1.13 illustrates the PMR process. The SUL is a highly permeable layer which acts a mirror and allows the creation of a closure loop with the write head. Since the gap between the SUL and the write head is

minimal, it allows the use of high write fields that can easily record the desired data on the media. Additionally, Wrap Around Shields (WAS) are often employed around the read and write head to ensure that the downtrack and crosstrack field gradients are high, grains adjacent to the one being written are not affected by the write head field, and the read head does not detect stray transitions. The WAS however may reduce the total write field available to switch the media grains. Fig 1.14 describes the various layers of the PMR media which allow high density recording. The lubricant and overcoat[53] are used to protect the recording layer from contaminants and mechanical accidents (like head crashes). The Intermediate Layer[54][55][56][57] may consist of several layers like a seedlayer like MgO that allows the initial magnetizations of the recording layer to be aligned along the easy axis. At the same time, it also allows the recording layer to be exchange decoupled from the SUL. An adhesion layer like NiTa is used to ensure the media can be properly fabricated over a substrate like glass. Although the creation of an additional SUL layer leads to more noise (spike noise due to domain wall formed in SUL, spike noise due to interaction of SUL with the head and low noise)[58], PMR has allowed significant gains in storage capacity. The best PMR capacities (up to 1.0 Tb/in^2[59]) have been obtained for bits containing 6-10 grains per bit with an average diameter <D> ~ 8nm. The need to address the magnetic trilemma however has forced research to focus on HAMR as a possible alternative to PMR especially after PMR densities seem to have saturated.

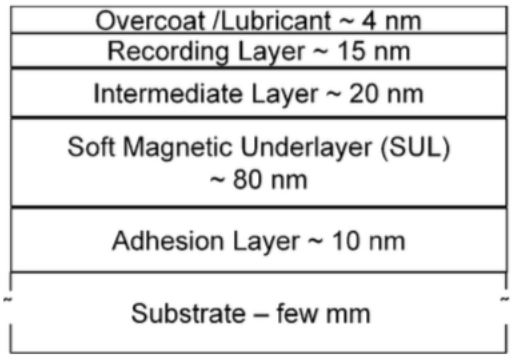

Fig 1.14 Different layers for the PMR media with approximate thicknesses[51]

1.4 Thermal Stability and the Magnetic Trilemma

The focus of developing different recording technologies has always been to address the issues faced by the current recording technology. Most of these issues can be simplified into a set of three problems that are interdependent on each other. These three issues form the magnetic trilemma. To understand this trilemma, a Stoner Wohlfarth model for an isolated grain is considered. It is assumed that the grain has a uniaxial anisotropy with the easy axis (the direction in which the magnetization saturates in the absence of an external field) pointing in the vertical direction. Let the angle between the magnetization (M) and the easy axis = θ and the angle between the applied field and the easy axis = α. In this case, the total energy for an isolated grain (E) can be written as

$$E = K_u \sin^2(\theta) - HM_s\cos(\alpha-\theta) \tag{1.1}$$

Minimizing the total energy with respect to θ can allow us to calculate the maximum and minimum energy in a specific configuration for different values of α. For some special cases ($\alpha = 0$ or $\alpha = 90$), these calculations are easier. In this case, the energy difference between the maximum and minimum possible energies can be given by

$$\Delta E = K_u\left(1 - \frac{H}{H_k}\right)^2 \tag{1.2}$$

where H_k is called the anisotropy field. For a grain of volume V, the energy difference is given by

$$\Delta E = K_u V\left(1 - \frac{H}{H_k}\right)^2 \tag{1.3}$$

In the magnetic recording process, when the disk passes below the write head, an applied magnetic field is used to store a bit pattern on the disk surface. Once the disk passes the write head, this pattern is stored as data in the absence of an external field (H=0). Thus, the energy barrier when data is stored is K_uV. Since the grains of the recording medium have a random size distribution, it is difficult to achieve a distinguishable signal on different grains that are close to each other. A consequence of the expected increase in

useful storage capacity/User Density is that the grain size/grain volume is becoming smaller. Smaller grains are thermally unstable, and their magnetization is susceptible to switching randomly due to random errors or thermal fluctuations. The decrease in the grain volume leads to an increase in the probability of magnetization reversal due to thermal fluctuations. This probability is given by

$$P = A\tau e^{\frac{-\Delta E}{k_B T}} \tag{1.4}$$

where A is the attempt frequency associated with gyromagnetic precession (10^9-$10^{11}s^{-1}$), τ is the thermal relaxation time according to Arrhenius-Neel and $\Delta E = K_u V$ is the energy barrier between two stable magnetization states with different configurations. ($K_u V/k_B T$) is denoted as the thermal stability factor. Obviously as the grains become smaller (V decreases), the thermal stability factor decreases. For magnetic grains to retain data written on them and avoid random switching for 10 years, this factor is calculated to be about 60. Since the objective is to employ grains with small volumes, the need of the hour is to use materials with high anisotropy (K_u) at room temperature (300K).

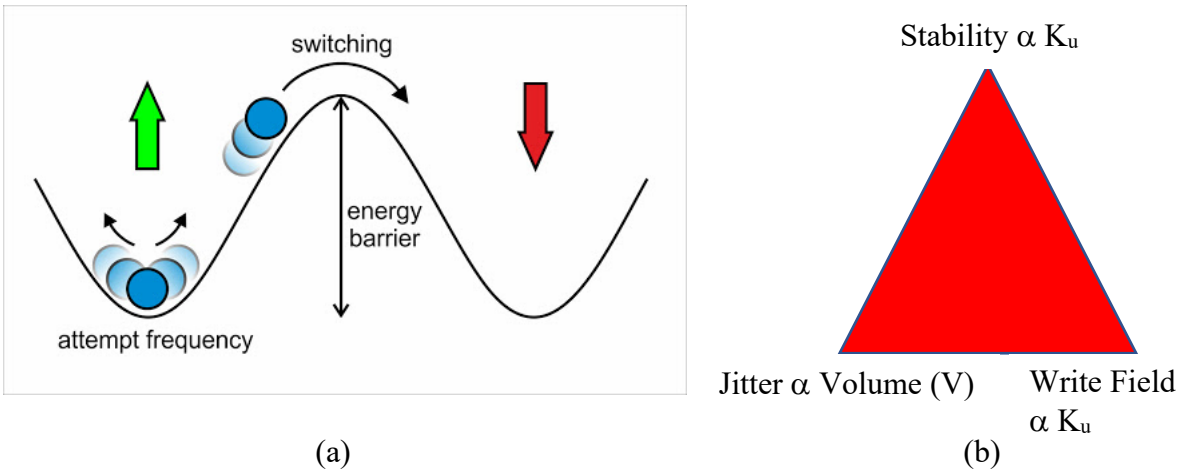

Fig. 1.15 (a) Schematic for the energy barrier for different magnetization states[60] (b) Magnetic Trilemma showing three interdependent issues

Additionally, to obtain an adequate Signal to Noise Ratio (SNR) for the recorded data pattern, the number of grains/bit (N) also needs to be increased significantly, since SNR α $(N)^{1/2}$[61]. Another way to look at this is the minimum noise (jitter) in the recording

process increases as the grain volume increases, thus enhancing the need to decrease grain volumes and consequently look for materials with high anisotropy values. However, the switching field (used to switch the magnetization of grains to record the desired data pattern) increases as the grain anisotropy increases. The current head designs can only supply fields up to a certain value thus creating difficulties in the writing process. Fig 1.15a shows an example of magnetization switching by crossing the energy barrier while Fig. 1.15b shows the magnetic trilemma as described. It is difficult to simultaneously address these three requirements, but with the advent of HAMR technology, this has become partially possible.

1.5 Thesis Outline

The focus of this thesis is to consider the advances made in HAMR technology and to address some of the issues specifically pertaining to the further improvement of performance parameters for the HAMR process. There exist numerous optimization solutions that focus on understanding the nature of noise in the HAMR process, improving the output of the HAMR process and finding solutions to issues that currently plague the data storage industry. The next few lines delineate a general outline followed by this thesis to present these solutions.

Chapter 1 summarizes the interminable need for data storage as well as the progress made in the HDD technology to address this issue. The chapter talks about different recording technologies developed to store the data for long-term use and the advantages and disadvantages of each of these technologies. Finally, the chapter addresses the primary issues which every future recording technology hopes to address with an eye on attaining the expected Areal Density values as predicted by the ASTC roadmap.

Chapter 2 discusses the recording technology that is the focus of this thesis, HAMR. The chapter gives an overview of the technology and the physics that allows it to address the magnetic trilemma. The chapter talks about developments made to fabricate the light delivery system including lasers and NFT's, as well as the new layers added to improve

the functionality of HAMR media. It also talks about the noise sources currently plaguing the HAMR process and which will be addressed in this thesis.

Chapter 3 describes the computational process used to obtain the micromagnetic simulation results presented as a part of the thesis. The mathematical formulation of different fields used as a part of the LLG equation is described along with a description of the renormalization technique. Important results calculated with the use of this technique are presented for the isotropic and anisotropic model of $L1_0$ FePt, a popular HAMR media. Chapter 4 is closely related to the results presented in the latter part of Chapter 3. Renormalization parameters for doped or non-stoichiometric anisotropic $L1_0$ FePt model are calculated in this chapter.

Chapter 5 deals with a newly proposed Thermal ECC media that decouples the issue of recording and long-term data storage. The chapter describes the efforts made in order to reduce DC noise and improve SNR for a thin ECC media that is relatively easier to fabricate compared to thicker media. The chapter also describes a novel Ensemble Waveform Analysis package provided courtesy of Seagate Technology.

Chapter 6 deals with one of the most important issues currently preventing the commercial release of HAMR HDD's. It proposes a low temperature HAMR media to reduce the writing and recording temperature in the HAMR process ensuring that HAMR HDD's are able to function much longer than their expected lifetimes. Optimization approaches ensure that the low temperatures do not affect the recording performance of the proposed media and limits are calculated beyond which cooling the media can have adverse effects on the HAMR performance.

Chapter 7 addresses another important issue which is the calculation of noise (transition jitter) in the HAMR process. Identifying the complete lack of an analytical formulation to calculate jitter in the HAMR process, the chapter discusses the dependence of jitter on various HAMR parameters, and derives an analytical formulation considering both the media and head effects on jitter. The formulation can act as a potential substitute for the otherwise lengthy and time consuming complex micromagnetic simulations.

Chapter 8 addresses the issue of Adjacent Track Erasure (ATE) arising as a consequence of writing multiple closely spaced tracks in HAMR. The presence and numerical extent of ATE is established in different HAMR media and efforts are made to reduce the ATE significantly to allow HAMR to achieve its eventual User Density limits.

The thesis will conclude by summarizing the important conclusions from the thesis and identifying the future of the HAMR technology, which generates several interesting avenues of research to explore and which can help the HDD industry gain even greater traction in the data storage business.

Chapter 2

Heat Assisted Magnetic Recording

The progress made by the HDD industry in addressing the concerns of increasing data generation and the need for devices to store this data has led to a proliferation of HDD's throughout the world. As the amount of data generated every day is increasing, there is a demand to ensure it's safe and long term storage. With the limitations of the previously painstakingly developed recording technologies like LMR and PMR and the saturation limits they have reached, there is a demand for newer technologies that can specifically address the magnetic trilemma. Some improvement has been made in an effort to develop Shingled Magnetic Recording (SMR) as well as Two Dimensional Magnetic Recording (TDMR). However, these seem to be stopgap measures which have the same limitations as LMR and PMR. Additionally, the noise generated in these processes comes from tracks written in both the directions.

The superparamagnetic limit (when the thermal stability is low and grain magnetization changes orientation randomly) imposes limits on the eventual SNR values and the ability to scale recording technologies to achieve higher storage densities. Heat Assisted Magnetic Recording (HAMR) attempts to address the magnetic trilemma by temporarily heating the media to high temperatures above the Curie temperature (T_c) of the media. This is done with the use of a laser passing through a Near Field Transducer (NFT) and incident on the media at a localized spot. This process is illustrated in Fig. 2.1. Heating the media close to and beyond the T_c value leads to a significant decrease in its effective coercivity. The heated region on the media is then rapidly cooled down in the presence of an externally applied head field whose orientation encodes the configuration of the recorded data. Ideally, a focused laser beam with minimal lateral spread can ensure only a specific region is heated and recorded. Once the heated region is cooled down, data is

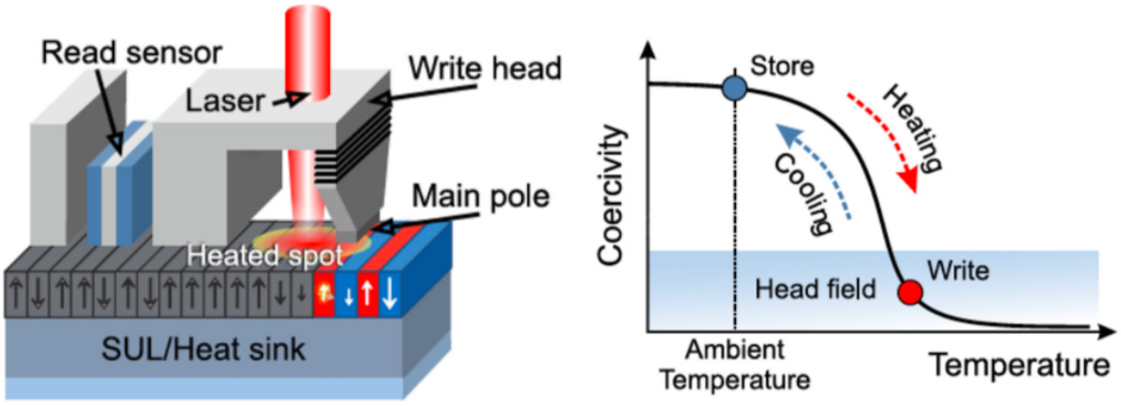

(a) (b)

Fig. 2.1 (a) Illustration of the HAMR process (b) Illustration of the temperatures at which writing and data storage occurs[62]

stored at room temperature. HAMR requires the development of several novel components including a light delivery system, the thermomagnetic writer that includes a laser and NFT, a rapidly cooling media with a good heatsink that can ensure minimum lateral heat conduction, recording media that can sustain high temperatures over a long period of time and a robust head disk interface that includes a lubricant and overcoat to protect the recording layer.

Since the heating of the media leads to a decrease in the coercivity, materials with significantly high anisotropy (and coercivity) values at room temperatures can be employed to fabricate the recording media in the HAMR process. This can also permit the grain diameters to be extremely small and yet ensure stable recording in the presence of a limited head field. Thus, HAMR is able to address the magnetic trilemma successfully. The next few pages are dedicated to understanding the novel components in the HAMR system.

2.1 HAMR Light Delivery System

The main optical elements of the light delivery system[63][64][65] in HAMR are the laser, the focusing optics and the NFT. The magnetic localization problem of PMR has

been replaced with the issue of localizing the thermal field in HAMR[66]. Fig 2.2 (a) describes the HAMR head that includes the laser and NFT while Fig. 2.2 (b) shows the light delivery path in HAMR. With conventional far field optics, spot size minimization is limited to about half the wavelength in diameter. The diffraction limit for a spot size d (equal to its Full Width Half Maximum) is given by

$$d = \frac{0.51\lambda}{NA} = \frac{0.51\lambda}{n\sin\theta} \tag{2.1}$$

where n = refractive index of the medium in which light is focused and θ denotes the half angle of the cone of focused light. The most common laser sources used to heat the media include diode lasers which are an inexpensive source of coherent light. According to equation (2.1), it is advantageous to reduce the wavelength of light used in the process to obtain smaller focused spots. The smallest possible spots obtained can be ~240nm size when λ ~ 405nm and n = 0.85 which are figures for the DVD Blu-Ray recorders. Laser diodes with smaller wavelengths are available but these diffraction limits force the use of more focusing mediums (higher n), light condensers and NFT's.

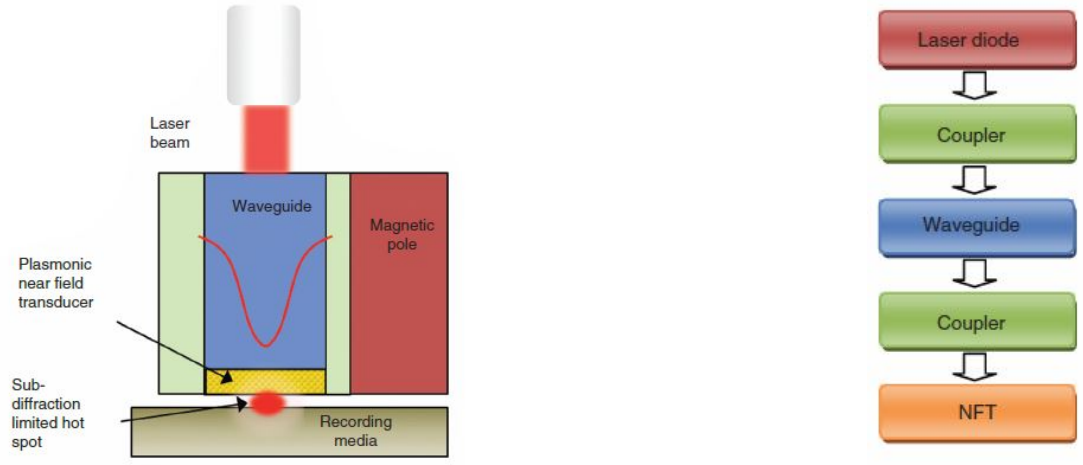

(a) (b)

Fig. 2.2 (a) HAMR write head including laser and NFT (b) HAMR light delivery path[67]

To improve the focusing power and reduce spot sizes, high refractive index materials like liquid immersion oils or solid immersion lenses (SIL) can be used to focus light on the bottom of hemispherical lenses. Both have the same working principle but solid immersion lens (SIL) made out of glass or other types of high index material have been developed to decrease the size of the focusing spot by a factor of 1/n over its value in the air[68][69] . To ensure that the light which is focused in the high index medium couples efficiently with the media without too much spreading of the spot size, the media must be close to the SIL within a distance of half the spot diameter. With a SIL of numerical aperture 1.8, refractive index of 2.08 and λ =405nm, a corresponding spot size ~ 115nm was achieved[70]. A planar variation of the SIL is the solid immersion mirror (SIM) which is able to focus the light to reduce the spot size even more (up to 90nm). Unfortunately, these spot sizes are too big compared to the expected spot size (~25nm) necessary to obtain high storage densities. This forces the use of NFT's in HAMR.

The idea of using the NFT can be traced back to early work of Bethe on the theory of diffraction by small holes in an infinite conductive plane[71]. The main constraint of using NFT's is that they cannot be coupled efficiently with far field optics. In consonance with this constraint is the necessity to provide enough power and sufficient resolution that makes it necessary to employ near field optics with the use of apertures or antennas to overcome the diffraction limit. The basic principle of an NFT is to break the diffraction limit by concentrating the optical energy into a spot much smaller than the incident laser wavelength. This energy localization is accompanied with the requirement of large field enhancement within the optical spot. NFT's are able to produce a cross-track full-width at half-maximum (FWHM) spot of < 50nm as required by the requirement of high areal density. Plasmonic nanostructures are favored by the recording industry to heat the recording layer. The principle employed by these nanostructures that allows the interaction of the metallic NFT's with the metallic media is called the Surface Plasmon Resonance (SPR). Plasmons can be described as interaction particles found where there is an interaction between a metal and a dielectric, as shown in Fig. 2.3. Although there are

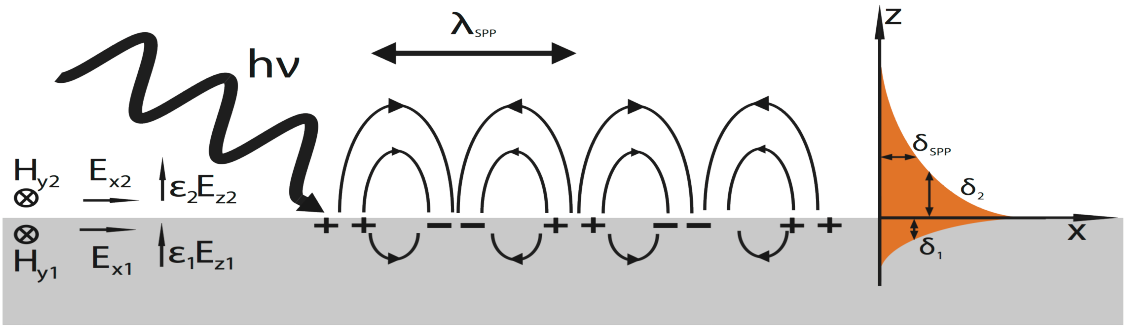

Fig. 2.3 Schematic for generation of the Surface Plasmons[72]

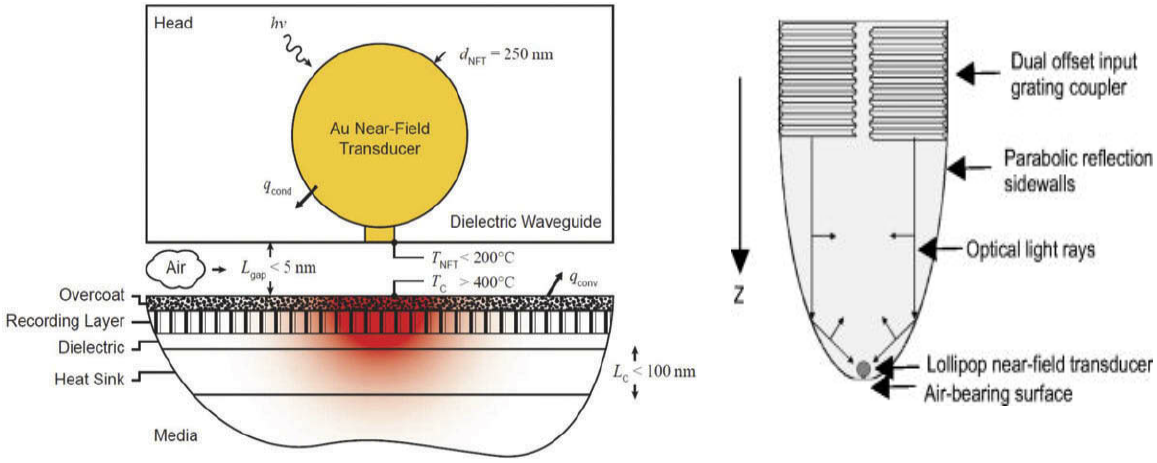

(a) (b)

Fig. 2.4 (a) Details of the lollipop NFT[73] (b) Light focusing before reaching the NFT[74]

several categories of plasmonic NFT's (with different aperture shapes and antenna designs), the most commonly used NFT design is called a 'lollipop NFT' where plasmons are generated on a circular disk and a rectangular peg is used for concentrating the light on the media (Fig. 2.4 (a) and (b)). The NFT peg heats the media that moves in the downtrack direction. The HAMR process first involves the use of near infrared light (~800nm) that passes from the laser's emitter facet through the slider to the NFT which constitutes a path length ~ 100nm. A thick input coupler (n = 1.6 to 1.9) that is first used

to collect the laser spot then guides the light in a tightly confined mode inside a planar waveguide with high index (the waveguide consists of two layers: a cladding which is Al_2O_3 and a core which is Ta_2O_5). The light via multiple reflections on a parabolic SIM then reaches the NFT. The details of this light path are shown in Fig. 2.2 (b). NFT materials must be robust against the Air Bearing Surface (ABS) environment, must be able to sustain high temperatures and be structurally stable. Some good NFT peg materials are metals with noble characters like Ag and Au where Au is the most frequently used material.

2.2 HAMR Media

A primary feature that makes the HAMR technology unique compared to other technologies is the use of heat to increase temperature and thus allow recording in spite of the use of high anisotropy materials for the recording media. The utilization of thermal assistance means that the integrated HAMR medium (the recording layer and other layers that make up the media) should not only be thermally stable, but consist of well-ordered grains with high anisotropy and a thermal design for heat confinement and good vertical heat conduction. Fig. 2.5 shows the HAMR media with different layers. What makes the structure unique is the presence of a heatsink layer as well as a lubricant/overcoat (OC). The key challenges for the HAMR media can be collated as follows (1) Controlled T_c distribution (ii) Small grain sizes with columnar grains (where height/diameter > 1) (iii) Small grain diameters (~4nm) leading to high storage densities (iv) good thermal design especially for the heatsink (v) low DC noise with rapid cooling of grains

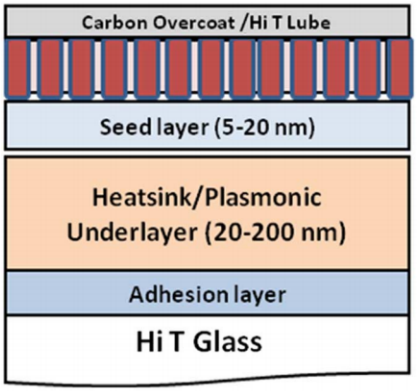

Fig. 2.5 Basic HAMR media design[75]

Undoubtedly, the most important layer is the recording layer that consists of grains on which specific data patterns are written. To ensure data is recorded and stored properly, the grains should have a high anisotropy (at room temperature), they should be thermally stable (columnar grains with high height/diameter ratio) and well ordered (high squareness in the hysteresis loops) to distinguish each individual grain from the other. There are several potential magnetic materials for the recording layer. Considering the requirement of high anisotropy, materials like $L1_0$ FePt, FePd, CoPt, MnAl are all potential materials. However, most of these materials require annealing at high temperatures to ensure high anisotropy values that can affect the chemical ordering and grain sizes. $SmCo_5$ and $Nd_2Fe_{14}B$ are another class of materials considered because of their high anisotropy. However, they have extremely complex structures that are difficult to fabricate via sputtering. Additionally, these Rare Earth (RE) materials suffer from serious corrosion issues. Similarly, Co/Pd and Co/Pt multilayers are another class of materials that possess high anisotropy, however these values are normally for a stack of these layers and individua Co/Pt or Co/Pd layers have low anisotropy.

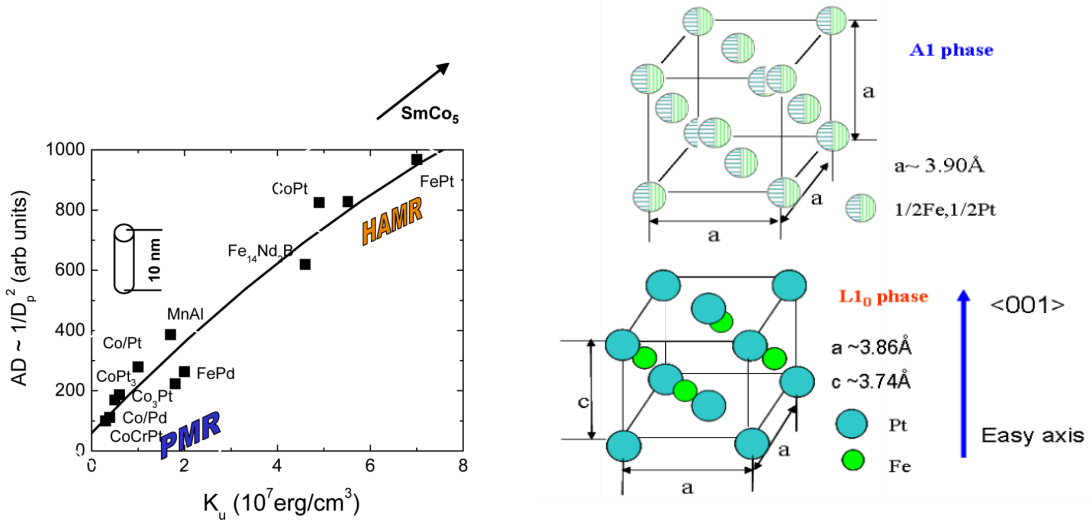

(a) (b)

Fig. 2.6 (a) Achievable Areal Density (AD) values for different materials[76] (b) Phases of FePt[77]

Type	Material	K_1 (10^7 erg/cm^3)	M_s (emu/cm^3)	H_k (kOe)	T_c (K)	D_p (nm)
Co-alloy	$CoCr_{20}Pt_{15}$	0.3	330	18.2		14.4
	$Co_3Pt(L1_2)$	2	1100	36.4		6.9
	$(CoCr)_3Pt$	1	800	25.0		10.2
	$CoPt_3$	0.5	300	33.3	600	9.7
Multilayer	Co_2/Pt_9	1	360	55.6	500	6.6
	Co_2/Pd_9	0.6	360	33.3	500	9.1
$L1_0$	FePd	1.8	1100	32.7	760	7.8
	FePt	7	1140	122.8	750	2.6
	CoPt	4.9	800	122.5	840	3.0
R.E.	$SmCo_5$	20	910	439.6	1000	1.4

Table 1. Magnetic and granular properties for different materials[76][78][79]

Table 1 lists some of the important properties for materials under consideration for the recording layer. D_p denotes the minimum grain diameter that ensures thermal stability (with height = 10nm). Fig. 2.6 (a) shows the variation of achievable areal density (AD) values based on K_u values for different materials. Based on Fig. 2.6 (a) and Table 1, it is clear that $L1_0$ FePt is an ideal material for the HAMR media. There are however several challenges in general when it comes to fabrication of $L1_0$ FePt for HAMR media. Fig. 2.6 (b) shows the two phases in which FePt exists. The A1 phase has extremely low anisotropy and high process temperatures (up to about 600°C) are required to achieve the $L1_0$ phase[80]. The $L1_0$ FePt phase is a FCC tetragonal structure with the (c/a) ratio = 0.96. Such high ordering temperatures makes it difficult to control and reduce the grain size. Granular $L1_0$ FePtX-Y refers to $L1_0$ FePt alloyed with different materials where X refers to materials used to reduce the ordering temperature (like Ag, Cu) and Y refers to materials used to segregate individual grains for good ordering and columnar growth (like C, SiO_2 and TiO_2). Use of Ag & Cu as dopants can reduce the ordering temperature but they can significantly reduce the T_c of individual grains leading to a decrease in the anisotropy values and causing stability issues. The T_c distribution can also lead to

additional noise problems. Use of carbon as a segregate material assures good particle separation and high degree of $L1_0$ ordering but individual grains are spherical with rough surfaces. Use of SiO_2/TiO_2 ensures that the grains are cylindrical with high smoothness but result in extremely poor separation and poor ordering. While the most common fabrication process for the recording layer is DC sputtering, different fabrication processes have been proposed to ensure that both the requirements of small grain size and columnar grains is ensured. An example is the Embedded Mask Patterning (EMP) process[81][82] which decouples the magnetic properties and the granular properties of the recording layer. This simplifies the constraints in the fabrication process by making the FePt layer in the process responsible for the magnetic properties and the Ru-SiO_2 layer deposited on top of the FePt layer responsible for the granular properties. An interlayer/seedlayer can often be used to ensure proper $L1_0$ chemical ordering and ensure that the easy axis of distribution has minimum value, or in other words the orientation is almost perfect. The most commonly use seedlayer is MgO which ensures this distribution ($\Delta\theta < 3°$). However, this adds further complexity to the functionality of the HAMR stack since MgO is an insulator and does not allow for good conduction of heat from the recording layer leading to poor thermal gradients and high lateral heat conduction.

The lubricant/overcoat layer is used to protect the recording layer from any accidents (like head crashes) or contact with the NFT and the read head. NFT heating, expansion and protrusion may occur in the media due to (i) Scattering of heat from the NFT (ii) backheating from the media (iii) thermal fly height control power and writer current[83]. The recording layer also has to sustain high temperatures in the HAMR process (~900K) that may lead to a significant degradation. Commonly used overcoats must be extremely hard materials to ensure the protection of the media. Although diamond was proposed as an ideal material for its hardness, Diamond like carbon (DLC) is used as an overcoat material due to the high cost associated with diamond. For lubricant materials, good fluidity/wetness, high adhesion to surfaces and good thermal stability are the main criteria. There are three main concerns with lubricants (i) decomposition which happens frequently with lubricants with high molecular weight (ii) evaporation which is more

common with lubricants with low molecular weight (iii) thermocapillary shear stress that causes lubricant displacement to certain areas on the media. Decomposition kinetics are sensitive to the lubricant end groups and lubricant thickness as well. Conventional perfluoropolyether (PFPE) lubricants like Z-Dol and Z-Tetraol are currently used to coat the recording layer[53]. Most of these lubricants commonly have the $-CH_2OH$ end group. These lubricants may also be used to protect the NFT from the same high temperatures faced by the media.

Achieving high thermal gradients, efficient energy supply to the media and minimum lateral conduction in the recording process can be assured with the presence of a good heatsink material in conjunction with Plasmonic Underlayers (PUL's). The PUL can ensure minimum lateral spread from the NFT and heatsink layers can control the thermal conductivity. Some commonly used materials for the heatsink layer include metals with noble character (like Au and Ag), Al, Cu and Cr. NiTa is a commonly used adhesion material to ensure proper contact of the heatsink with the substrate (like glass).

2.3 Noise sources in HAMR

In the HAMR process, there are three main components which encounter noise problems[84]. The largest amount of noise is often present in the recording process in the HAMR media. This is followed by noise in the magnetoresisitive (MR) read heads followed by the electronic noise which has the lowest value. Often, only the media noise is considered for calculations of the total noise. There are two temperatures that are significantly important in the HAMR process. The first temperature is the writing temperature which is the temperature at which the probability that the magnetization switches is approximately (1/2). This value is often close to T_c especially for the $L1_0$ FePt media. The other temperature is the Curie temperature (T_c). In the HAMR process, most writing happens at temperatures close to T_c thus requiring a well-defined T_c value to be of paramount importance. Near the T_c value, both M_s & K_u (the saturation magnetization and anisotropy respectively) are close to zero and hence the Zeeman energy (M_sHV) and thermal stability are both low. Thus, a variation in the T_c value can cause serious noise

issues. As has been described previously, the HAMR media is fabricated by DC sputtering and related processes. Often the use of segregate materials and process variations leads to a variation in the grain size.

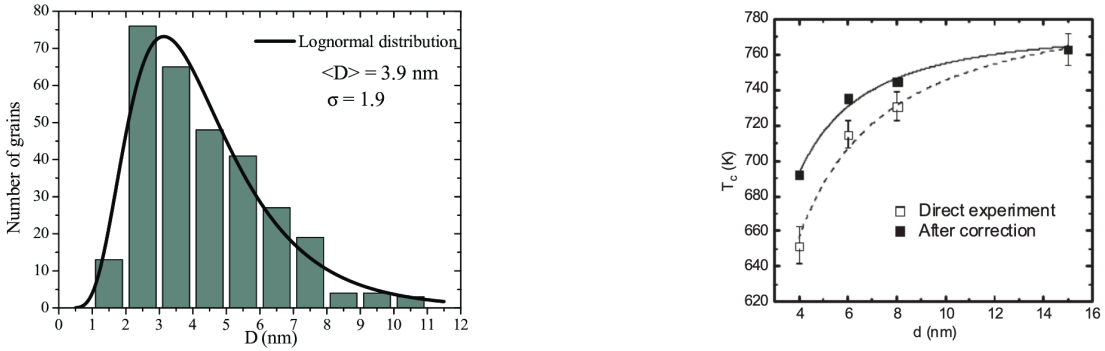

(a) (b)

Fig. 2.7 (a) Grain diameter (D) with a lognormal distribution[85] (b) T_c variation with grain diameter[86]

Fig 2.7 (a) shows an example of the Grain Size Distribution (GSD) which follows a lognormal distribution. Without agglomeration, the grain sizes follow a Gaussian distribution. Ideally, the HAMR fabrication processes aim for a GSD < 10%. A natural consequence of a finite GSD is the variation in the T_c value for individual grains. This variation becomes more significant as the average grain size decreases. Fig. 2.7 (b) illustrates the variation of T_c value for individual grains of different sizes. Another consequence of the grain size variation is a variation in the intrinsic anisotropy values for individual grains. This intrinsic variation causes a distribution in the anisotropy field (H_k) that in turn contributes to a switching field distribution (SFD). Another noise source in HAMR which is common in all the recording technologies is random switching caused due to thermal fluctuations[87]. As described before, thermal fluctuations are caused due to low energy barriers which depend on the grain volume. In HAMR, the grain sizes used are frequently ~5nm thus making thermal fluctuations an important and unintentional source of noise. Recent research[88] has also pointed out to the fact that a variation in the

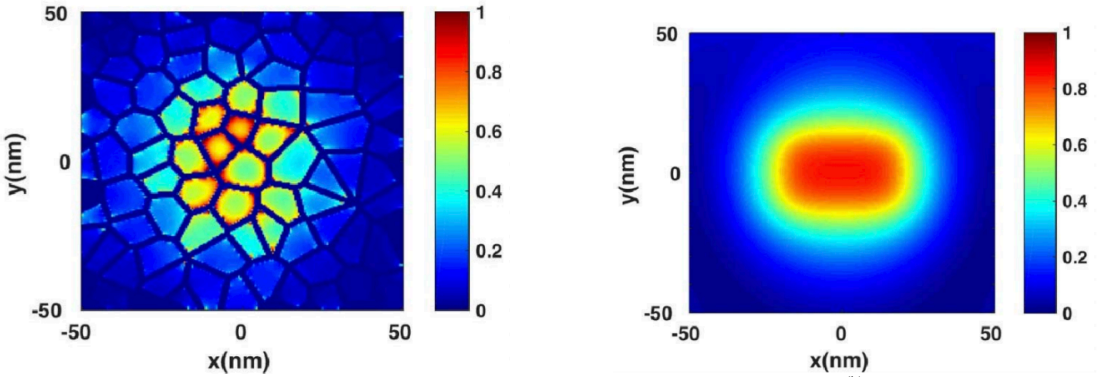

(a) (b)

Fig. 2.8 (a) Differential absorption of power and rise in temperature for the granular media (b) Effective Media Theory (EMT) approximation for the HAMR media[88]

grain size can lead to a differential absorption of energy from the NFT to a differential change in temperature for individual grains causing additional jitter (noise), as shown in Fig. 2.8 (a) where the grains at the center have the maximum power absorption. An approximation to this absorption is given by the Effective Media Theory (EMT) (Fig. 2.8 (b)). In addition to the media noise which is dominant, the MR head also contributes to the noise in the HAMR process. There are three main kinds of noise for the MR head (i) Johnson noise (ii) Shot noise (iii) Mag noise. Johnson noise is directly proportional to the resistance of the MR head and the temperature. That makes it an important contributor to noise in the HAMR process when writing takes place close to T_c. Mag noise is inversely proportional to the volume of the MR head. The nature of this noise is similar to thermal fluctuations forcing magnetizations to switch. The shot noise is also inversely proportional to the MR head volume. It can be characterized by a Poisson process and in electronics, it originates from the discrete nature of electric charge[89]. Thus, it can be understood as being inversely proportional to the total number of electrons between the MR heads. It is obvious to notice that decreasing the shield to shield spacing or decreasing the MR head volume to improve the resolution in the readback process would lead to an increase in the head noise. This is one of the limiting factors in designing

smaller MR heads. The HAMR system being an electrical circuit also consists of electronic noise. This noise arises primarily from the preamplifiers, connecting wires and the circuitry as well as due to any current leakages. Overall, its magnitude is quite low.

2.4 Summary

The chapter gives an overview of the HAMR process and some of the advances made through the implementation of this process. The chapter described in detail, the HAMR magnetooptical recording process with a laser and NFT as well as the materials and processes associated with the same. The chapter also delineated the various layers of the HAMR media that can help understand the interplay of various factors that determine the performance of the process. It is obvious that HAMR has an important role to play in enhancing the importance of HDD's in the data storage industry.

Chapter 3

Simulation Process

The computational process presented in this thesis describes the process implemented behind the micromagnetic simulations that are used to calculate most of the results in this thesis. The first idea behind the use of micromagnetic simulations was published by Prof. William Fuller Brown Jr.[90] when he published a paper relating to the calculation of antiparallel domain wall structures. Largely, micromagnetics deals with the study of the behavior of magnetic materials (in this case, ferromagnets) at micrometer and sub-micrometer scales. This is especially useful when dealing with quantities (like energies of nanostructures) where experimental calculations might be difficult. In the simulations implemented in this thesis, the Landau Lifshitz Gilbert (LLG) equation is used to mimic the magnetization dynamics of grains of the recording medium. The LLG equation has had several forms before it attained the form used in the micromagnetic simulations. In 1932, Bloch reported the first description of the time-dependent motion of uncoupled and undamped magnetic moments [91]. In 1935, Landau and Lifshitz proposed an equation describing the damped motion of the magnetization in a ferromagnet, known as the Landau-Lifshitz (LL) equation[92]. This equation was then modified by Gilbert by taking into account, the strong damping present in some thin films. The LLG equation has now been modified to account for several additional energies (like accounting for Spin Transfer Torque switching for multilayer structures).

To understand the evolution of the LLG equation, it is first understood that the LLG equation calculates the variation in magnetization (M) as a function of time (t). This variation is a function of the spatial magnetization, effective field and the gyromagnetic ratio (γ) which is a ratio of the magnetic moment to the angular momentum for a single particle. Depending on the terms included in this equation, it can describe a precessional or dissipative mode of motion for the magnetization in the presence of an effective field. With the development of computers with high speed processors, parallel computing

devices like GPU's and the ability to make simplified assumptions (like assuming length scales larger than atomistic scales but smaller than domain wall dimensions) when dealing with magnetic systems, it is possible to simulate real world examples of recording systems with the use of micromagnetic simulations and the LLG equation.

3.1 LLG equation for undamped motion

As described before, the LLG equation aims to understand the variation in the magnetization of a sample in the presence of different constant and varying parameters. An important constant parameter in this equation is the gyromagnetic ratio (γ) whose definition has already been mentioned before. In the absence of any dissipative forces, the magnetization (M) has a precession motion around the applied field (H). To understand this precession motion, the relation between the angular momentum (P) and torque (L) for a rotating rigid body is considered. The two quantities can be related as follows:

$$\frac{dP}{dt} = L \tag{3.1}$$

Based on the definition of the gyromagnetic ratio, equation (3.1) can be written as follows where m is the magnetic moment:

$$\frac{dm}{dt} = \gamma L \tag{3.2}$$

By definition, for an applied field (H), using the definition of the magnetic torque (L)

$$\frac{dm}{dt} = -\gamma(m \times H) \tag{3.3}$$

For a body of volume V, this can be rewritten in the form of magnetization (M) as

$$\frac{dM}{dt} = -\gamma(M \times H) \tag{3.4}$$

3.2 LLG equation with dissipative forces

With equation (3.4), magnetization can rotate around the applied field axis unless acted upon by a resisting force. The criteria for the dissipative forces in the LLG equation is two-fold (i) ensure the total magnitude of magnetization (equal to the saturation magnetization M_s remains constant. This is the major difference between the LLG and LLB or Landau-Lifshitz-Bloch equation where M is not conserved) (ii) ensure the final direction of magnetization results in the system having minimum energy (in other words, M must be parallel to H). The term chosen for phenomenological reasons to describe the dissipative forces is $\frac{(-\gamma\alpha)}{M_s}(M \times (M \times H))$. Here α is called the Gilbert damping constant. This equation helps realize the magnetization motion in strongly damped systems like thin films. For $L1_0$ FePt, the value at room temperature (due to spin orbit interaction) was calculated to be 0.02[93]. Thus, the LLG equation with dissipative forces can now be written as

$$\frac{dM}{dt} = -\gamma(M \times H) - \frac{\gamma\alpha}{M_s}(M \times (M \times H)) \tag{3.5}$$

Replacing γ by $\frac{\gamma}{1+\alpha^2}$ the final form of the LLG equation becomes

$$\frac{dM}{dt} = -\frac{\gamma}{1+\alpha^2}(M \times H) - \frac{\gamma\alpha}{(1+\alpha^2)M_s}(M \times (M \times H)) \tag{3.6}$$

$$\frac{dM}{dt} = -\frac{\gamma}{1+\alpha^2}(M \times H) + \frac{\gamma\alpha}{(1+\alpha^2)M_s}\left(M \times \left(\frac{\partial M}{\partial t}\right)\right) \tag{3.7}$$

Fig. 3.1 (a) and (b) show the illustration of the magnetization motion for the case of both undamped and damped motion.

In this thesis, only the effect of the precession related torque and the damping effects are taken into account to study the magnetization dynamics of grains. The next section describes in detail, the numerical implementation of the LLG equation.

(a) (b)

Fig. 3.1 (a) Schematic for undamped precession of magnetization (b) damped precession for magnetization[94]

3.3 Numerical Implementation of the LLG equation

The LLG equation (for example equation 3.6) is an ordinary differential equation. A common technique used to solve these equations is numerical integration methods. The Runge-Kutta family of methods is a family of techniques used in solving equations in numerical analysis by discretizing the intervals over which the equation is integrated. The RK4 or the fourth order Runge-Kutta method[95] is the most popular method in this family and is used to solve the LLG equation in the thesis.

The initial problem is considered as follows

$$\frac{dy(t)}{dt} = f(t, y); y(t_0) = y_0 \tag{3.8}$$

where the initial value of the function y(t) is y_0 at time $t=t_0$. y(t) can be a scalar or vector function (For example, in this case, it is the magnetization M(t)). Now considering a discretization step with size $h = \Delta t$, the solution to the differential equation is given as

$$y_{n+1} = y_n + \frac{1}{6}h(k_1 + 2k_2 + 2k_3 + k_4) \tag{3.9}$$

$$t_{n+1} = t_n + h \tag{3.10}$$

where the values for the other terms (for n=0,1,2,3….) are

$$k_1 = f(t_n, y_n) \tag{3.11}$$

$$k_2 = f(t_n + \frac{h}{2}, y_n + h\frac{k_1}{2}) \tag{3.12}$$

$$k_3 = f(t_n + \frac{h}{2}, y_n + h\frac{k_2}{2}) \tag{3.13}$$

$$k_4 = f(t_n + h, y_n + hk_3) \tag{3.14}$$

In equation (3.10), y_n denotes the value of function at iteration n, and y_{n+1} denotes the value at iteration n+1. The step size used in the simulations for this thesis is ~10^{-14}.

For the LLG equation, magnetization corresponds to the variable y, and the time derivative of magnetization from equation (3.6) can be obtained by assuming the spherical coordinate system for M

$$M_x = M_s \sin(\theta) \cos(\varphi) \tag{3.15}$$

$$M_y = M_s \sin(\theta) \sin(\varphi) \tag{3.16}$$

$$M_z = M_s \cos(\theta) \tag{3.17}$$

The time derivative is given as

$$\dot{\vec{M}} = M_s[(\dot{\theta}\cos(\theta)\cos(\varphi) - \dot{\varphi}\sin(\theta)\sin(\varphi))\vec{x} + (\dot{\theta}\cos(\theta)\sin(\varphi) + \dot{\varphi}\sin(\theta)\cos(\varphi))\vec{y} - (\dot{\theta}\sin(\theta))\vec{z}] \tag{3.18}$$

Similarly, the total field (H) can be written using the Cartesian coordinate system

$$H = (H_x)\vec{x} + (H_y)\vec{y} + (H_z)\vec{z} \tag{3.19}$$

By substituting values from equation (3.18) and (3.19) into equation (3.6), calculating the vector products $\vec{M}\times\vec{H}$ and $\vec{M}\times(\vec{M}\times\vec{H})$, and comparing the $\vec{x}, \vec{y}, \vec{z}$ components on both sides, the time derivative for the magnetization angles can be obtained. This can help derive the equation for change in magnetization with respect to time.

$$\dot{\theta} = \frac{\gamma}{1+\alpha^2}[(\alpha\cos(\theta)\cos(\varphi) - \sin(\varphi))H_x + (\alpha\cos(\theta)\sin(\varphi) + \cos(\varphi))H_y - (\alpha\sin(\theta))H_z] \tag{3.20}$$

$$\dot{\varphi} = \frac{-\gamma}{1+\alpha^2}[(\cot(\theta)\cos(\varphi) + \alpha\mathrm{cosec}(\theta)\sin(\varphi))H_x - (\mathrm{cosec}(\theta)\cos(\varphi) - \cot(\theta)\sin(\varphi))H_y - H_z] \quad (3.21)$$

3.4 Calculation of effective field

The effective field in the LLG equation consists of five components. For the magnetic recording system, the externally applied field (H_{appl}) is used to write a specific pattern on the media depending on its orientation. However, the effectiveness of the externally applied field (usually of the order of 8-10kOe) depends on the magnitude of the other fields. The total field (effective field) is given by the expression

$$\vec{H}_{eff} = \frac{\partial E}{\partial \vec{M}} + H_{th} + H_{appl} \quad (3.22)$$

Based on the different energies in the system, the effective field can be written as

$$\vec{H}_{eff} = \vec{H}_{appl} + \vec{H}_{th} + \vec{H}_{k} + \vec{H}_{ex} + \vec{H}_{demag} \quad (3.23)$$

where H_{th} is the thermal field (due to thermal fluctuations or random errors), H_k is the anisotropy field, H_{ex} is the intergranular exchange field and H_{demag} is the demagnetization field due to magnetostatic energy.

3.4.1 Applied and Stochastic thermal field

As described above, the applied field in the recording process used to obtain results in this thesis has a constant magnitude ~10kOe. In general, it may vary with respect to both the magnitude and direction. Also, as explained before, the existence of a finite thermal barrier means that as the material is heated, thermal agitation can lead to a change in the magnetization state or even phase transitions (ferromagnetic to paramagnetic). In order to capture the magnetization dynamics at temperatures T>0, it is necessary to model this thermal agitation. This was done successfully in [87] where

$$\sigma = \sqrt{\frac{2k_B T\alpha(1+\alpha^2)}{M_s V\gamma(\Delta t)}} \quad (3.24)$$

where α is the Gilbert damping constant, γ is the gyromagnetic ratio and Δt is the time discretization in the RK4 method. The thermal field is now written as

$$H_{thermal} = \sigma \times \vec{h} \tag{3.25}$$

where the field $\vec{h}$ is considered to be a white noise (error) with the following properties[96][97][98]

$$< h_i(t) > = 0 \tag{3.26}$$

$$< h_i(t1)h_{i'}(t2) >= \delta(i - i')\delta(t1 - t2) \tag{3.27}$$

Equation (3.27) clearly shows that the correlation between the thermal fields is a combination of two Kronecker delta functions and is zero when the two locations or calculation times are different. In other words, the thermal field is assumed independent of other values at other locations and times. In order to ensure the field response is independent of time, the time step must be chosen carefully (and must be small enough).

3.4.2 Anisotropy field

There can exist different kinds of anisotropies for a magnetic material. However, they can mainly be classified into crystalline and stress anisotropy. For the magnetic recording simulations in our thesis, stress anisotropy is comparatively small and crystalline anisotropy is significant (due to the crystalline nature of $L1_0$ FePt). The origin of this anisotropy in magnetic materials is the spin orbit interaction. In general, the crystalline anisotropy energy is given as

$$E_{anisotropy} = K_0 + K_1(\alpha_1^2\alpha_2^2 + \alpha_2^2\alpha_3^2 + \alpha_1^2\alpha_3^2) + \text{higher order terms} \tag{3.28}$$

where α_1, α_2 and α_3 are the direction cosines for magnetization. For a popular HAMR media like $L1_0$ FePt, uniaxial anisotropy is given as

$$E_{anisotropy} = K_u \sin^2\theta = K_u(1 - \cos^2\theta) = K_u(1 - (\vec{k} \cdot \vec{m})^2) \tag{3.29}$$

Here θ is the angle between the magnetization and easy axis. $\vec{k}$ and $\vec{m}$ are unit vectors for the easy axis and magnetization. Then the uniaxial anisotropy field can be given as

$$H_k = \frac{2K_u}{M_s}(\vec{k} \cdot \vec{m})\vec{k} \tag{3.30}$$

3.4.3 Exchange field

The exchange field arises from the exchange interaction between two spins, that is a quantum mechanical behavior. This exchange interaction attempts to change the configuration of the spins to an arrangement where the energy of the system is minimum. The exchange interaction thus leads to a change in the alignment of adjacent spin moments. The total exchange energy of spin i, considering all the other spins j is given by

$$E_{exchange} = \sum_{i \neq j} -J_{ij}(\vec{S}_i \cdot \vec{S_j}) \tag{3.31}$$

Here $\vec{S}_i$ and $\vec{S_j}$ are two spins at sites i and j such that $|S_i| = |S_j|$ and J_{ij} is the atomistic exchange constant which depends on the material. Assuming $\vec{S_j} = (\vec{S}_i + \Delta\vec{S}_{ij})$,

$$E_{exchange} = \sum_{i \neq j} -J_{ij} \cdot (\vec{S}_i \cdot (\vec{S}_i + \Delta\vec{S}_{ij})) \tag{3.32}$$

$$E_{exchange} = \sum_{i \neq j} -J_{ij} \cdot ((\vec{S}_i)^2) + \sum_{i \neq j} -J_{ij} \cdot (\vec{S}_i \cdot (\Delta\vec{S}_{ij})) \tag{3.33}$$

Since by definition

$$(\vec{S}_j)^2 = (\vec{S}_i)^2 + 2(\vec{S}_i \cdot \Delta\vec{S}_{ij}) + (\Delta\vec{S}_{ij})^2 \tag{3.34}$$

and the magnitudes of the spins are the same, we write

$$(\vec{S}_i \cdot \Delta\vec{S}_{ij}) = \frac{-(\Delta\vec{S}_{ij})^2}{2} \tag{3.35}$$

$$E_{exchange} = J_{ij} \sum_{i \neq j} \frac{(\Delta\vec{S}_{ij})^2}{2} - J_{ij} \sum_{i \neq j} (\vec{S}_i)^2 \tag{3.36}$$

Considering a cubic lattice with lattice parameter a, the exchange energy can be written using equation (3.37) as

$$E_{exchange} = \frac{A}{{M_s}^2}(|\nabla_x \vec{M}|^2 + |\nabla_y \vec{M}|^2 + |\nabla_z \vec{M}|^2) \tag{3.37}$$

Based on the equation (3.22), the exchange field can now be found as

$$H_{exchange} = \frac{2A}{{M_s}^2}(\nabla_x^2 \vec{M} + \nabla_y^2 \vec{M} + \nabla_z^2 \vec{M}) \tag{3.38}$$

Equation 3.38 can be approximated for a 3D case considering the nearest neighbors

$$H_{exchange} = \frac{2A}{{M_s}^2}\left[\frac{M(i+1,j,k)-M(i-1,j,k)}{(\Delta x)^2}\vec{x} + \frac{M(i,j+1,k)-M(i,j-1,k)}{(\Delta y)^2}\vec{x} + \frac{M(i,j,k+1)-M(i,j,k-1)}{(\Delta x)^2}\vec{z}\right] \quad (3.39)$$

3.4.4 Demagnetization field

In the presence of an external field, when magnetizations are aligned in a certain direction, free poles exist that oppose the alignment of the magnetization. The interaction of the magnetic field and magnetization is given by the magnetostatic energy. Unlike the exchange energy which has a significant value only for the nearest neighbors, the magnetostatic energy is calculated considering the interaction of one site (atom) with all the other sites (atoms). This increases the complexity of the calculations and also leads to this energy calculation being the most time consuming calculation. The total magnetostatic field or demag field at a certain location (r) is given as

$$\mathrm{H_{magnetostatic}} = \frac{-1}{4\pi}\int\left[\frac{3(\vec{r}-\vec{r'})\,(\mathrm{M}(\vec{r'})(\vec{r}-\vec{r'})}{|\vec{r}-\vec{r'}|^3} - \frac{\mathrm{M}(\vec{r'})}{|\vec{r}-\vec{r'}|^3}\right]\,\mathrm{d}\vec{r'} \quad (3.40)$$

Since the interactions are considered all over the space, this is a 3D integral. Another way of writing the integral is

$$\vec{\mathrm{H}}(\mathrm{x},\mathrm{y},\mathrm{z})_{\mathrm{magnetostatic}} = \iiint \vec{\mathrm{M}}(\mathrm{x},\mathrm{y},\mathrm{z})\,\overleftrightarrow{\mathrm{N}}(\mathrm{x}-\mathrm{x}',\mathrm{y}-\mathrm{y}',\mathrm{k}-\mathrm{k}')\,\mathrm{dx}'\mathrm{dy}'\mathrm{dz}' \quad (3.41)$$

where $\overleftrightarrow{N}$ is the Green's function (a constant function) of the system, which in the case of 3D LLG is a tensor. It can be represented as

$$\begin{bmatrix} N_{xx} & N_{xy} & N_{xz} \\ N_{yx} & N_{yy} & N_{yz} \\ N_{zx} & N_{zy} & N_{zz} \end{bmatrix}$$

The details for working out this integral are given in [99]. For a system with m1, m2 and m3 elements in the 3 directions, one calculation would take time of the order of O(m1m2m3) and the total calculation would be of the order of $O((m1m2m3)^2)$. This is clearly a difficult calculation and would be require extreme resource allocation if it were to be executed on the CPU. To facilitate faster simulations, the magnetostatic field is calculated on a parallel computing unit called the GPU. The Fast Fourier Transform

(FFT) algorithm is used to calculate this field since it reduces the computational time from $O(n^2)$ to $O(n\log_2 n)$. This is a significant improvement especially when n is large.

Calculation on the GPU is especially advantageous as this ensures that the CPU is free to perform other computations. The CUDA version of the FFT function (CUFFT) is used to implement the FFT algorithm on the GPU. While CPU's are latency oriented and focus on reducing the delay in access times, GPU's focus on faster parallel implementations of the same instruction and thus are throughput oriented. The extra number of cores, especially on the most recent GPU's are responsible for faster calculations. Fig. 3.2 shows the architecture of both the CPU and the GPU. Fig. 3.3 shows the process that is used to implement the simulations using both the CPU and GPU[32][100].

Significant improvements can be obtained especially in terms of reducing the computational time by understanding the system architecture. In the operation to calculate the effective field, the CPU and GPU access the global memory incessantly. Accessing this memory every time takes about 500 clock cycles, whereas other memories with limited capacities have lower access times. Usage of the shared memory available to each device, replacing double operands with float to reduce the required storage capacity and using fast math operations are just some of the ways in which the LLG equation can be simulated faster to save computational time and space.

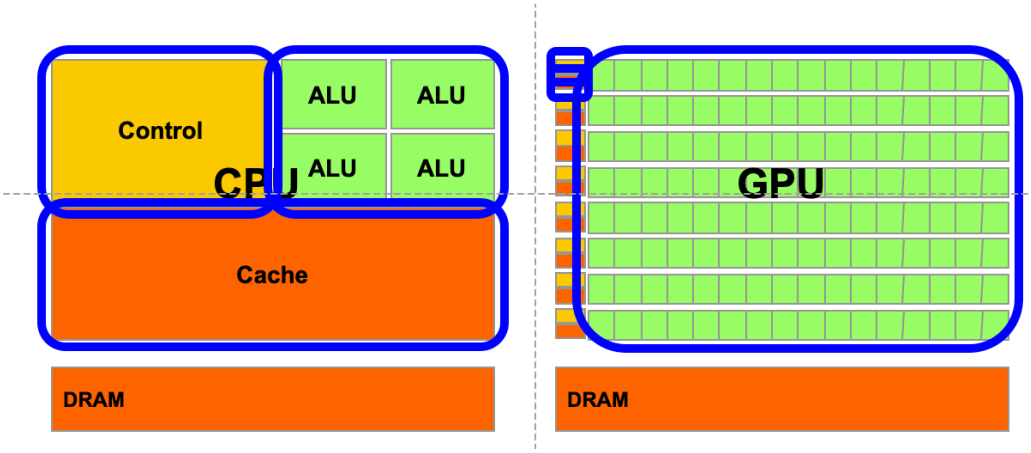

Fig. 3.2 Architecture for the CPU and GPU[101]

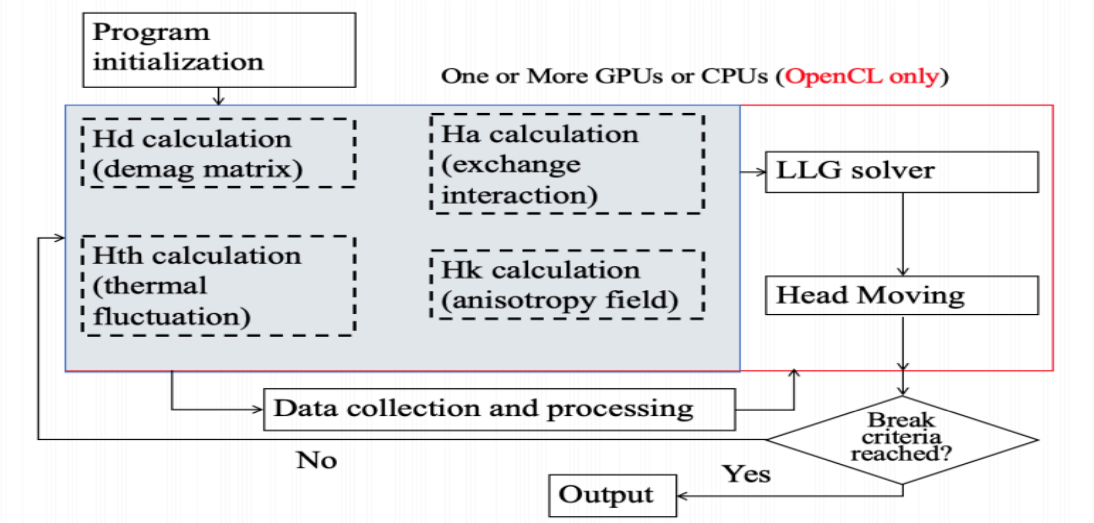

Fig. 3.3 Process flow for implementing micromagnetic simulations on the CPU and GPU. The red box indicates processes that are implemented on the GPU. Constant exchange of data occurs between the CPU and GPU and processes in the blue box with the dotted lines also have a component executed on the CPU[32].

3.5 Renormalization method for HAMR

During the explanation of the magnetic trilemma, the Stoner Wohlfarth model or the single spin model was introduced. The single spin model works well to describe the magnetization changes under certain conditions. However, in the presence of significant intergranular exchange coupling, adjacent spins start to cluster together reducing the effectiveness of the single spin model. Additionally, increasing the temperature can also cause thermal agitation leading to spins in a grain behaving independently of each other, thus leading to a necessity of addressing multiple spins. An atomistic model[102] which consist of one spin/atom is able to accurately depict most magnetic phenomena like high frequency spin waves, domain wall motion within a grain and the magnetization dynamics of individual grains. However, implementing simulations with atomistic scale modeling (of the order of a few angstroms) would involve the use of significant computational resources which are usually not available. This leads to researchers making simplified assumptions that do not accurately represent the behavior of magnetic

grains and grain boundaries. An example of this is the Landau-Lifshitz-Bloch (LLB) model[103] which adds a few terms to the single spin model. To accurately model multispin dynamics, the renormalization technique is useful. This is especially true for magnetic recording where the media consists of hundreds of grains.

The renormalization method[104] is a simplified modeling technique similar to the Finite Element Method where a renormalized block is the smallest unit of measurement and each block is assumed to encompass multiple atomistic spins. Thus, each block represents the aggregate properties of multiple spins. This works for the case of magnetic recording (especially HAMR) since in HAMR, the media is heated to temperatures close to T_c where the correlation length of spin fluctuations tends to infinity. Thus, at $T=T_c$ where the correlation length is infinity, an entire grain can be represented by one single block.

Fig. 3.4 illustrates the creation of the renormalized block system. Fig. 3.4 (a) represents the atomistic system where each small block represents one atom. Multiple spins in the atomistic system are combined to form a renormalized cell with an averaged spin as seen in Fig. 3.4 (b). These renormalized cells are then overlaid on a 3D magnetic recording media that consists of Voronoi grains of different shapes and sizes (Fig. 3.4 (c)).

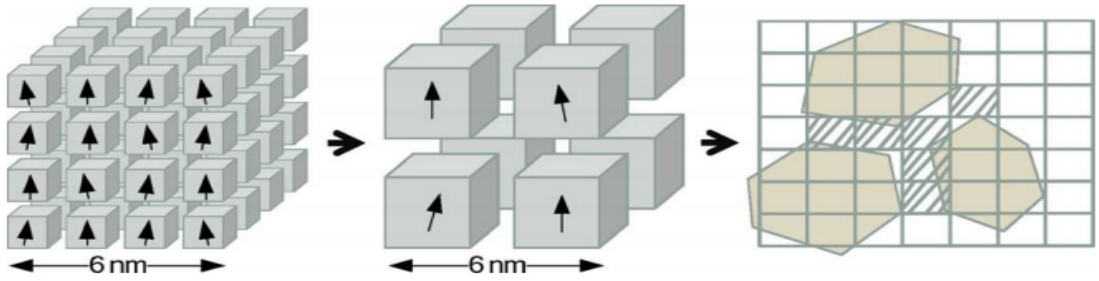

(a) (b) (c)

Fig. 3.4 Schematic to illustrate the renormalized block system creation (a) The atomistic $L1_0$ FePt system (b) Multiple atomistic spins combined to create the renormalized cell through the coarse graining process (c) The renormalized cells are overlaid on a 3D media with Voronoi grains[104]. The shaded portion between the magnetic Voronoi grains represents the non-magnetic grain boundaries.

3.6 Renormalization method for isotropic $L1_0$ FePt

For the HAMR process, a popular magnetic material is the $L1_0$ phase of FePt. The renormalization length (length of the renormalized cell in Fig. 3.4 (b)) depends on temperature. For the $L1_0$ FePt model, this length at the writing temperature is calculated to be about 1.5nm. This value can vary based on the magnetic properties and the corresponding writing temperature of the material under consideration. This length scale also represents a good tradeoff between the accuracy of the micromagnetic simulations and the computational time for the simulations.

For the isotropic $L1_0$ FePt model under consideration, the dimensions of the atomistic model are approximated to be 0.3nm, thus implying each renormalized cell contains about 125 atoms. An average grain size of 6nm is considered for the renormalized block system as shown in Fig. 3.4 (c). Thus, each renormalized block contains about 20*20*20 or 8000 atoms. The objective of the renormalization method is to mimic the magnetic properties calculated for the atomistic system for different temperatures.

The renormalization parameters represent the magnetic properties for the renormalized block system. The Gilbert damping constant formula is derived by the Visscher method[105]. Other renormalization parameters can be found by solving four simultaneous equations that compare the average magnetization, average anisotropy field and variance of anisotropy field for the atomistic system (where there is an absence of thermal fluctuations) and the renormalized system. These equations are shown below. These quantities are chosen since they affect the magnetization the most. Here, the 'average' refers to an average in space and time.

$$< M >_{atomistic} =< M(M_s, K_u, A_{ex}) >_{block} \quad (3.42)$$

$$< H_k >_{atomistic} =< H_k(M_s, K_u, A_{ex}) >_{block} \quad (3.43)$$

$$< \delta H_k >_{atomistic} =< \delta H_k(M_s, K_u, A_{ex}) >_{block} \quad (3.44)$$

Fig. 3.5 (a) – (d) show the renormalized parameters calculated for $L1_0$ FePt at different temperatures. For the atomistic system, the assumed parameter values for T=0 are M_s =

1100emu/cm^3 ; $K_u = 7\times10^7$erg/cm^3 ; $A_{ex} = 1.1\times10^{-6}$erg/cm. Isotropic exchange means the exchange assumed in different directions has the same value. Observing Fig. 3.5 (b) – (d), the dotted line denotes the saturation magnetization for the atomistic model (single spin).

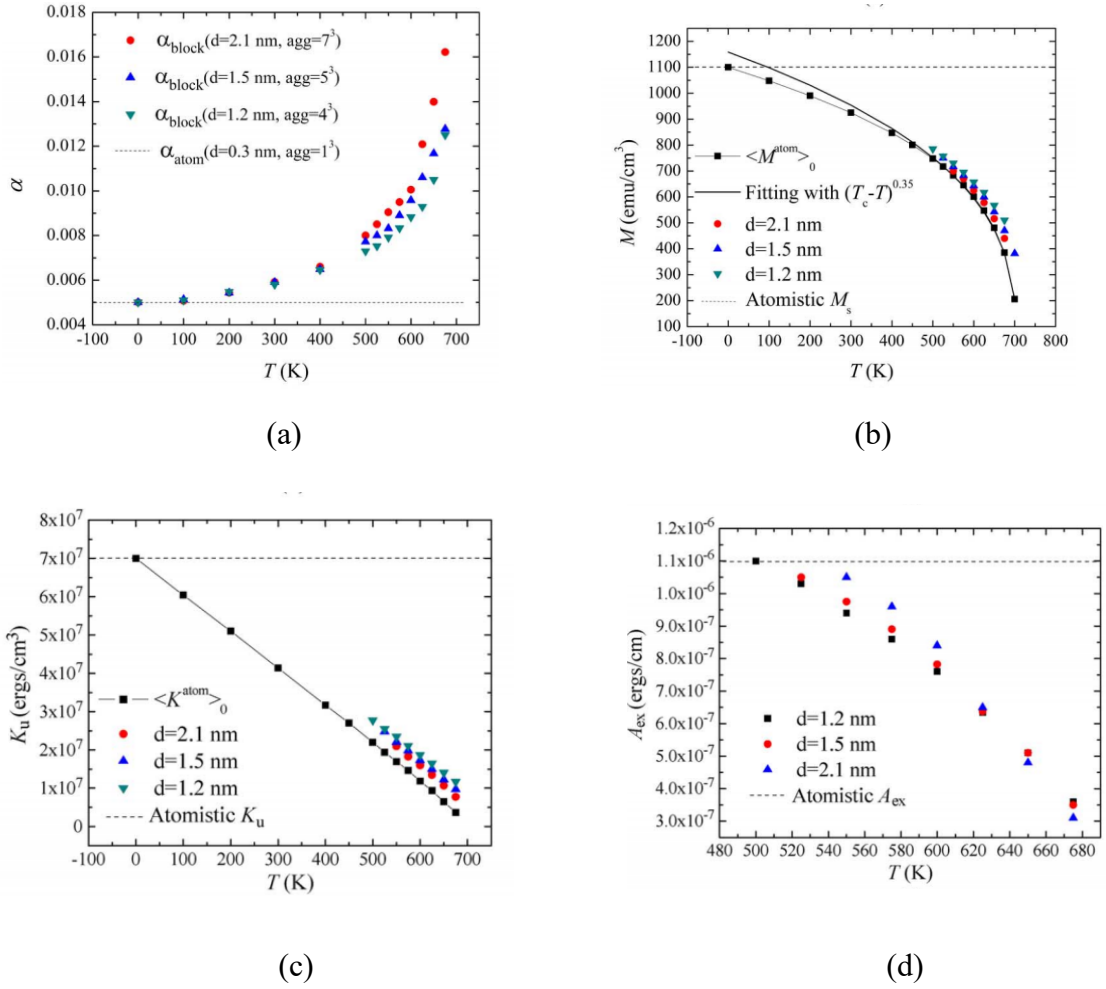

Fig. 3.5 Renormalized parameters for isotropic model for $L1_0$ FePt (a) Damping (The value at T=300K depends on the spin orbit interaction and was calculated to be 0.005. It was later recalculated to be 0.02[93]) (b) Saturation magnetization M_s (c) Uniaxial anisotropy K_u (d) Exchange. The variable 'd' in the legend denotes different renormalized cell sizes[104].

This is independent of temperature and hence there exists a straight line with the y intercept being the value of the parameter at T=0K. The solid black line (with the square

symbols) show the atomistic values for these parameters at different temperatures calculated through the atomistic simulation. The variable 'd' denotes the size of the renormalized cell. As 'd' increases, the renormalization parameter values start approaching the atomistic values. In the limiting case, when the $6nm^3$ (6nm×6nm×6nm) system is represented by a single cell, the atomistic parameter values would be exactly similar to the renormalization parameter values.

3.7 Renormalization method for anisotropic $L1_0$ FePt

As seen in Fig. 2.6 (b), the dimensions for the $L1_0$ phase of FePt are not exactly symmetric. The structure is tetragonal with the dimensions out of plane being slightly smaller. Additionally, exchange values vary based on the direction in which they are measured[106][107]. Thus, it is more realistic to consider an anisotropic model of FePt where five different directional exchanges are considered in two categories (i) in plane exchange A_{xy} and (ii) out of plane exchange A_z. For the anisotropic model, the dimensions of the unit cell for the atomistic system are 0.273nm and 0.374nm as opposed to 0.3nm. Thus, the renormalized cell with 1.5nm cell size contains about 5*5*4 or 100 atoms. Renormalization parameters are calculated for the anisotropic model[108] by equating four quantities for the atomistic and renormalized system, the average magnetization, average anisotropy field, variance of magnetization and variance of anisotropy field.

$$< M >_{atomistic} =< M(M_s, K_u, A_{xy}, A_z) >_{block} \quad (3.45)$$

$$< \delta M >_{atomistic} =< \delta M(M_s, K_u, A_{xy}, A_z) >_{block} \quad (3.46)$$

$$< H_k >_{atomistic} =< H_k(M_s, K_u, A_{xy}, A_z) >_{block} \quad (3.47)$$

$$< \delta H_k >_{atomistic} =< \delta H_k(M_s, K_u, A_{xy}, A_z) >_{block} \quad (3.48)$$

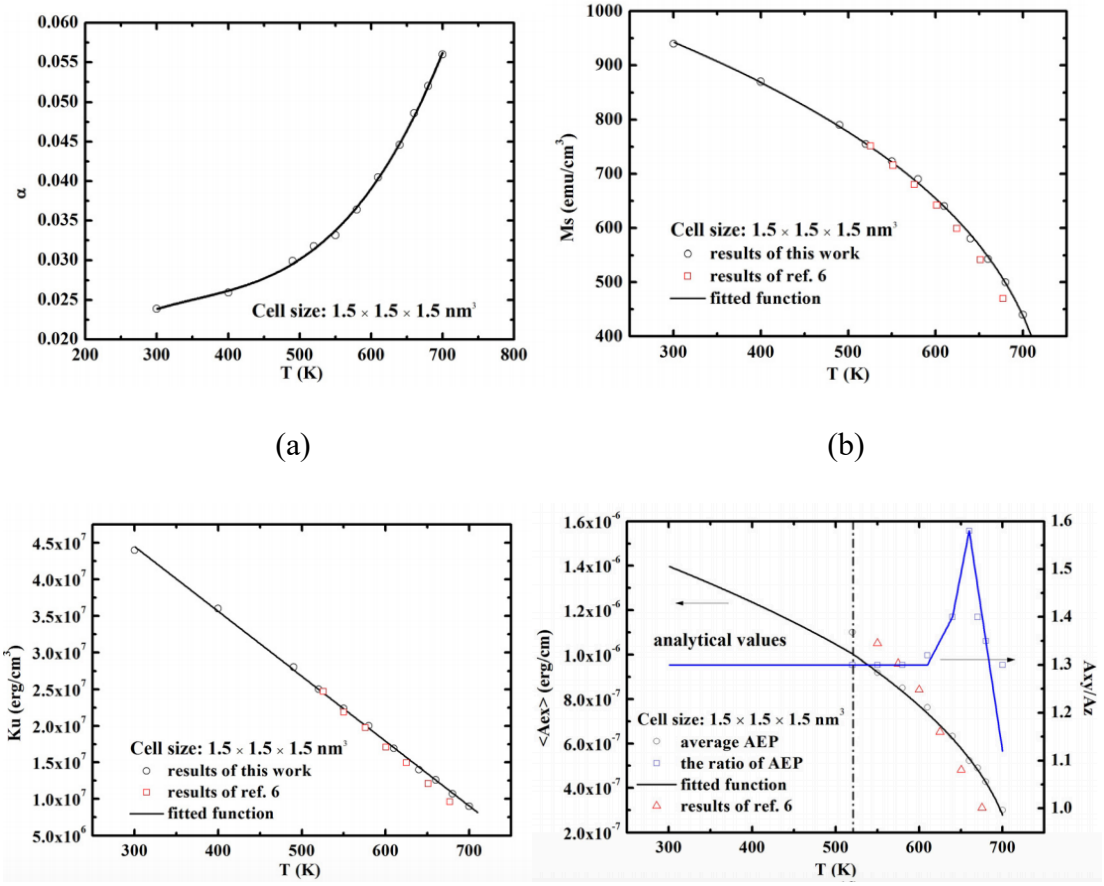

Fig. 3.6 Renormalization parameters for the anisotropic model of $L1_0$ FePt[108] (a) Damping (b) Saturation Magnetization M_s (c) Uniaxial Anisotropy K_u (d) Average exchange <Aex> (given by $\frac{1}{3}A_z + \frac{2}{3}A_{xy}$) and exchange ratio $\frac{A_{xy}}{A_z}$. Ref. 6 in the legend refers to [104].

Two cost functions are considered to solve equations (3.45) – (3.48). The cost functions are minimized simultaneously at different temperatures. The calculated renormalization parameters are shown in Fig. 3.6 (a) – (d). The atomistic parameter values at T=0 are the same as before. Comparing Fig. 3.5 and 3.6, it is clear that the nature of variation for the renormalization parameters remains the same irrespective of the exchange values in different directions, but the actual values of the parameters are different for different temperatures.

3.8 Summary

The chapter describes the details of the micromagnetic simulation technique implemented to solve the LLG equation for a magnetic recording system. The different forms of the LLG equation and its applications are explored. The chapter also describes the components of the effective field used in the stochastic LLG equation with formulations for each field. The highest computational time for the LLG equation is dedicated to calculating the magnetostatic interactions or the demagnetization field. To speed up the calculation process and reduce the simulation time, parallel computing unit called GPU's are used to perform a part of the operation of solving the LLG equation with minimal participation of the CPU. Techniques to improve the computational time further are explored. These techniques fundamentally exploit the architecture of the current systems and are based on reducing access to global memories and using fast math operations. The renormalization technique which is used as a fulcrum to support the simulation process is described by understanding its need and significance. Finally, the process of obtaining the renormalization parameters for the isotropic and anisotropic $L1_0$ FePt model is enumerated.

Chapter 4

Renormalization Parameters for doped FePt

The fabrication process for HAMR media includes an important step for heating the HAMR media to high temperatures above 600°C in the annealing process. This is extremely important in order to fabricate the ordered crystalline $L1_0$ FePt phase. As explained before, the HAMR media is generally written as FePtX-Y[109] where X and Y are different alloying elements that are used to encourage ordered columnar growth of grains, improve the $L1_0$ ordering of the granular HAMR media and reduce the ordering temperature. Based on different elements used in the fabrication process, the resulting HAMR media often ends up being non-stoichiometric and it is difficult to ascertain exactly, the composition of various elements in the granular media.

The use of different alloying elements not only affects the chemical ordering but also affects the magnetic properties of the HAMR media[110][111][112]. There is a clear correlation between the Curie temperature T_c and the grain size, which can vary based on the fabrication process for the HAMR media. A variation in the T_c value can lead to an additional variation in the values of other magnetic parameters like the saturation magnetization (M_s), anisotropy (K_u), damping (α) and exchange (A_{ex}). Since a granular variation and a consequent variation in the magnetic properties in fabricating the HAMR media is inevitable, there is a necessity to study and identify the extent of variation in the values for the magnetic parameters mentioned above.

The other aspect related to doped FePt is the different spin directions achievable at different temperatures for the FePt media. As the temperature varies, so does the anisotropy. The agitation of individual spins also leads to a distribution in the directions of individual spins. As the T_c value changes due to the doping process for FePt, this can lead to a significant disparity in the value of the exchange forces between adjacent spins. The study of the variation in the renormalization parameters for doped $L1_0$ FePt can thus also be useful to identify the behavior of this varying exchange to anisotropy ratio.

4.1 Estimation of renormalization parameters

Near the Curie temperature (T_c), magnetic parameters including magnetization, anisotropy, and damping depend strongly on both temperature and length scale[113]. This manifestation of renormalization theory is most readily seen in the case of magnetization where the magnitude of the atomic spin is largely unaffected by temperature, but the bulk magnetization vanishes at T_c. It has been previously argued that the Landau-Lifshitz-Gilbert damping parameter alpha exhibits a similar effect owing to its dependence on both atomic effects and magnon-magnon scattering, the latter having a strong length dependence. In the calculation of the renormalization parameters, damping due to the two magnon and higher order scattering is considered. Only pure exchange is considered without taking any dipolar effects into account. These parameter calculations are implemented for 1.5nm×1.5nm×1.5nm renormalized cells aggregated into a 6nm×6nm×6nm renormalized block system[104]. An anisotropic $L1_0$ FePt model is considered where exchanges in five different directions are accounted for[107][108]. The in-plane exchange (A_{xy}) is higher than the out of plane exchange (A_z) except very close to T_c when both these values disappear. Before the renormalization parameters can be calculated, the atomistic parameters are estimated by simulating an atomistic system with each atomistic cell measuring 0.273nm×0.273nm×0.374nm (unit cell dimensions for $L1_0$ FePt). The dimensions of the renormalized cell and the block system are kept constant.

The atomistic and renormalized damping are calculated using the Green Kubo method whose formulation has been given before[105][104]. However, a typographical error has been corrected here

$$\frac{\alpha^2_{\text{renormalized}}}{1+\alpha^2_{\text{renormalized}}} = \frac{-M_s}{\gamma}\frac{<\frac{d\vec{M}}{dt}\cdot\vec{M}\times\vec{M}\times\vec{H}>}{<(\vec{M}\times\vec{M}\times\vec{H})^2>} \tag{4.1}$$

Here $\vec{M}$ denotes the magnetization averaged over space (the 1.5nm^3 renormalized cell), $\vec{H}$ denotes the effective field averaged over the same space, M_s is the saturation magnetization at T=0 and γ is the gyromagnetic ratio. < > denotes an average over time and damping is calculated at different temperatures. Fig. 4.1 (a) shows the renormalized

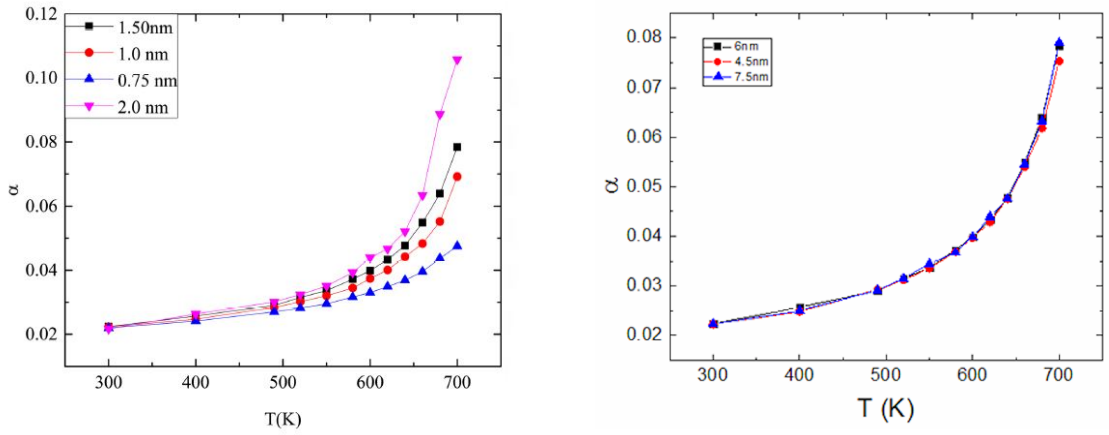

(a) (b)

Fig. 4.1(a) Renormalized damping for different cell sizes (b) Renormalized damping for different block sizes[113]

damping calculated for different cell sizes ranging from 0.75nm - 2nm. This damping is plotted as a function of temperature (T). In all the cases, the system size is still the same ($6nm^3$). It is clear that as the cell size increases, more spin waves are available to contribute to the damping process thus increasing the damping. This contribution is negligible at the lower temperatures but becomes progressively more significant at higher temperatures due to higher contributions by different damping mechanisms. This also helps explain the trend of renormalized damping as it approaches the atomistic value at low temperatures and increases as the temperature scales increase. Similarly, as the temperature increases, more magnons contribute to the damping process. Fig. 4.1 (b) shows the damping calculated for different renormalized block/system sizes. In this case, the damping remains almost equal irrespective of the system size. This is because irrespective of the system size, damping is calculated for each individual renormalized cell after averaging over the entire space. The averaging ensures the damping would remain the same for every system size. In this regard, it is also important to state that the damping values calculated using an anisotropic exchange model (different atomistic exchange values in different directions along nearest and next nearest neighbor interaction axes in the renormalized block) and an isotropic exchange model[104] (same

atomistic exchange value in different directions in the renormalized block) are significantly similar even at high temperatures.

To calculate the renormalization parameters for doped FePt, the atomistic values of these parameters is compared to the renormalization values at different temperatures as explained before in equations (3.47) – (3.50). Two cost functions are considered that calculate the difference between the parameters[108]. These cost functions are minimized to obtain the renormalization parameters. For doped FePt, there is an unintended consequence of variation in the T_c value. Although this variation is normally about 3-5%, a T_c variation of ±10% is considered to calculate these results. For non-doped FePt, the T_c value is considered to be 700K. Fig. 4.2 (a) – (e) show the renormalization parameters calculated for three different T_c values and at different temperatures. To consider the effect of T_c variation, we scale the atomistic exchange stiffness parameter values with respect to the change in T_c values, since the atomistic exchange stiffness is directly proportional to the Curie temperature of the material. The atomistic parameters calculated using the scaled value are then used to estimate the renormalization parameters for the new T_c with the same process as described above.

4.2 Analysis of variation of renormalization parameters

Referring to Fig. 4.2 (a), the damping increases for different T_c as the temperature increases. This is because, as temperature increases, the number of magnons contributing to the damping process also increase. At low temperatures, the primary damping contribution is the spin orbit interaction[114][115] and hence the damping values seem to be similar for different T_c values. As the temperature increases, additional two magnon and higher order scattering mechanisms contribute to the damping process. For the three T_c values under consideration, referring to Fig. 4.2 (b) the variation of M_s is insignificant for low temperatures but become significantly noticeable as the temperature increases. At temperature scales close to T_c, the renormalized M_s values can be fitted by the fitting equation $M_s \sim K(T_c-T)^{\beta}$ [104] where $\beta \sim (1/3)$.

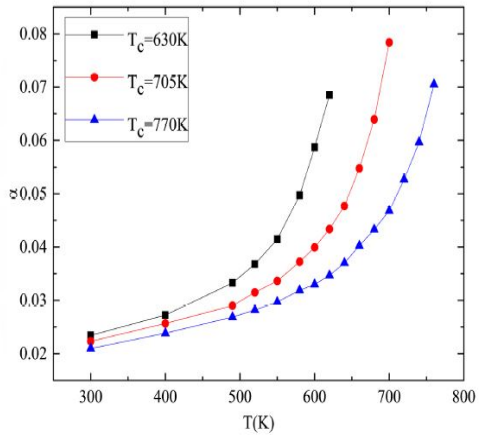

(a)

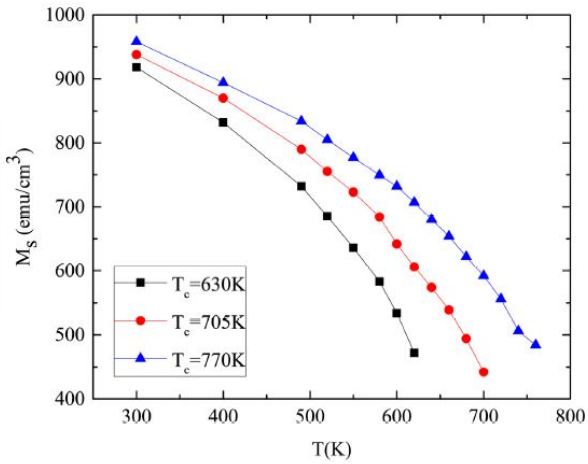

(b)

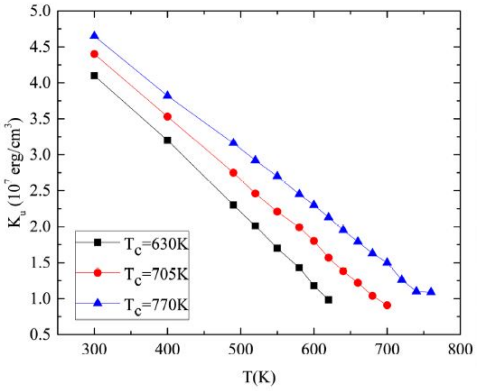

(c)

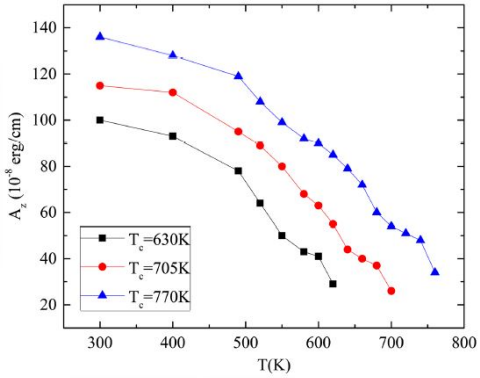

(d)

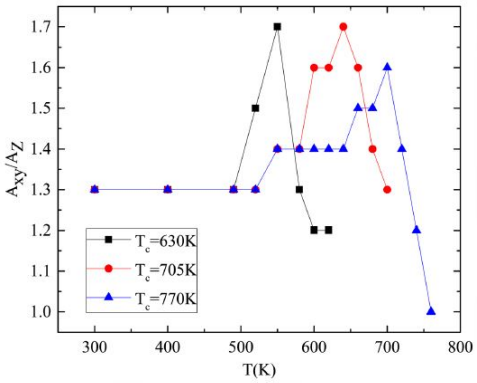

(e)

Fig. 4.2 Renormalization parameters for a 1.5nm^3 cell aggregated in a 6nm^3 system (a) Damping (α) (b) Saturation magnetization (M_s) (c) Anisotropy (K_u) (d) Out of plane exchange (A_z) (e) Exchange ratio (A_{xy}/A_z)[113]

Fig 4.2 (c) shows the variation of K_u as the temperature varies beginning from 300K. At temperature scales close to T_c, the renormalized K_u values can be fitted by the linear fitting function $K_u \sim K (T_c\text{-}T) + P$ where K and P are constants (for T_c=630K: K=9.77×10^4erg/cm^3-K, P=9.16×10^6erg/cm^3; for T_c=705K: K=8.82×10^4 erg/cm^3-K, P=8.16×10^6 erg/cm^3; for T_c=770K: K=7.92×10^4 erg/cm^3-K, P=9.29×10^6 erg/cm^3). In the limiting case the block spin represents the entire aggregated system and hence the renormalized block system possesses the intrinsic properties of a macroscopic system.

Fig. 4.2 (d) shows the variation of exchange values as the temperature varies beginning from 300K. At the lower temperature scales, the correlation length for the critical phenomena drops rapidly as the temperature drops. Thus, the renormalized approach is not valid at temperatures much lower than T_c, e.g., below 80% of T_c. Fig 4.2 (e) shows the exchange ratio A_{xy}/A_z as the temperature varies for the three T_c values. The ratio is constant for temperatures much lower than T_c as predicted from mean field theory. This can be explained in the following manner: the thermal fluctuations are always trying to disturb the exchange interactions, and because the out-of-plane exchange interaction along the z direction (A_z) is smaller than that in the in plane direction (A_{xy}), A_z is reduced faster than A_{xy} as the temperature increases, and as a result, the ratio of A_{xy} over A_z becomes larger and larger when increasing the temperature[113][108]. However, at T_c, not only the exchange interactions but also the ratio will "disappear" because of thermal fluctuations, so there is an abrupt drop near T_c as can be seen from Fig. 4.2 (d).

For the lower temperatures where the renormalization theory is not very accurate, the exchange ratios can be calculated from mean field theory. To understand this calculation consider Fig. 4.3 that shows the FePt $L1_0$ FCC structure. In the figure, $J_1 - J_5$ shows the directional exchanges for the anisotropic $L1_0$ FePt model. The formulation for exchange energy can be written as

$$E_{exchange} = \sum_i \frac{J_i}{2V}\left[\left|\frac{\partial \vec{S}_i}{\partial x}\right|^2 \left|\vec{r}_{x,i}\right|^2 + \left|\frac{\partial \vec{S}_i}{\partial y}\right|^2 \left|\vec{r}_{y,i}\right|^2 + \left|\frac{\partial \vec{S}_i}{\partial z}\right|^2 \left|\vec{r}_{z,i}\right|^2\right] \qquad (4.2)$$

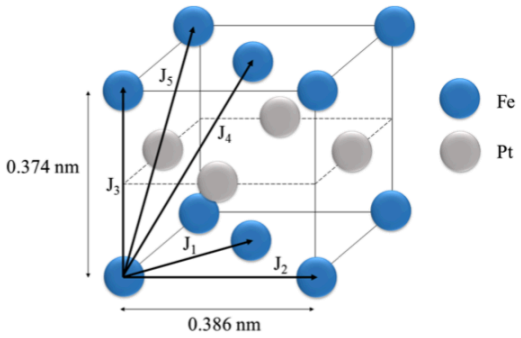

Fig. 4.3 Anisotropic model of $L1_0$ FePt BCT structure[113]

where $\vec{S}_i$ is the spin at a particular location i, $\vec{r}_i$ is the distance vector between neighboring Fe atoms and V is the $L1_0$ FePt lattice volume. Energies can be calculated in the five different exchange directions and components can be separated based on $\left|\frac{\partial \vec{S}_i}{\partial x}\right|$, $\left|\frac{\partial \vec{S}_i}{\partial y}\right|$ and $\left|\frac{\partial \vec{S}_i}{\partial z}\right|$. The exchange ratio is then proportional to the in-plane energy to the out of plane energy. This ratio is calculated to be 1.3 as shown in Fig. 4.2 (e).

4.3 Summary

This study was partially supported by Seagate. The chapter focused on understanding the variation of magnetic properties for doped and/or non-stoichiometric granular FePt which is a reality resulting from the variations in the fabrication process. Technologically, the chapter helps estimate the magnetic properties for different T_c values more accurately thus improving the accuracy of micromagnetic simulations. This helps improve the estimation of the recording performance, media noise and other such parameters. Scientifically, a study of these properties provides several intermediate points between the Heisenberg model (anisotropy/exchange = 0: spins can point anywhere) and Ising model (anisotropy/exchange = infinity: spins are constrained to two directions).

Chapter 5

Optimization of thinner Thermal ECC media

Most of the results presented in this thesis are obtained by implementing micromagnetic simulations. These simulations essentially solve the LLG equation at different instants of time for different designs of the HAMR head and media. Besides the writing process, the other important process is the playback process. In the playback process, the reciprocity principle is used to detect and readback the patterns written on the HAMR media[35]. The reciprocity principle states that the field generated by the written patterns on the media is the same as the field generated from the read head, which is much easier to evaluate. Thus, the reciprocity principle states that the readback signal is a convolution of the head field with the media magnetization and this is written as the amplitude of the playback signal.

In the HAMR process, noise can be generated in both the recording and the readback process. The noise generated in the readback process is mainly due to the noise in the read head and the noise due to the read head misalignment. The effect of the curved nature of transitions and the SNR reduction generated because of it has been studied before[116]. Solutions to this issue have also been provided like increasing the cross track field gradient[117][118], using a forked writer[119] and other changes to the head design[120][121]. An alternate treatment of this issue is also the micromagnetic modeling of the read head (just like the micromagnetic modeling of the HAMR media). In this case, the head is comprised of small elements with each element having a $1.5nm^3$ dimension[122]. However, the noise from the read head is not found to be a significant factor in the recording process.

The biggest issue in the recording process is the stochastic nature of writing and the issues that arise due to the variation in grain size and granular T_c variation. Before the extent of this issue can be understood, it is necessary to understand how the noise is generated, the nature of the noise and the solutions that have been proposed to reduce it.

5.1 Recording process and performance parameters

To implement micromagnetic simulations in the HAMR process, there is a process followed to mimic the actual process conditions and parameters so as to get the most realistic results. These steps are enumerated in detail in this section.

5.1.1 Voronoi media generation

The thesis has already described in detail, the fabrication process involved in generating the granular magnetic media. It is clear that the process depends on several experimental conditions like deposition rate, pressure, temperature and so on. This leads to a variation in the granular size as well as a random distribution of grains. To mimic this condition perfectly, the micromagnetic simulations used to calculate the results in this thesis use a Voronoi media. The generation of the Voronoi media is based on the idea of a Voronoi diagram, where a certain region is divided into multiple areas where each area consists of a set of points closes to a certain point whose distribution is predetermined by a random seed. The Voronoi diagram can also be referred to as a Dirichlet tessellation[123]. An example of such a Voronoi diagram is given in Fig. 5.1. The cells in the Voronoi diagram are called Voronoi polygons or Dirichlet regions.

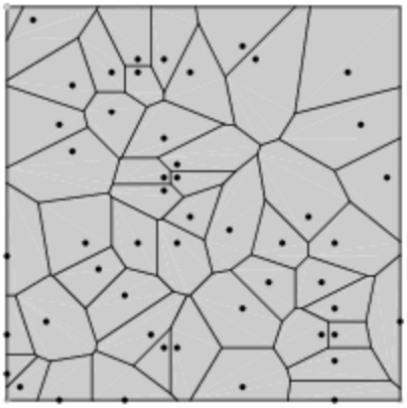

Fig. 5.1 Example of a Voronoi diagram[124]. The solid black dots are generated using a random seed that generates this distribution of points. The cells are generated by modeling a set of points closest to the solid black dots in the diagram. The distance used for this purpose is the Euclidean distance

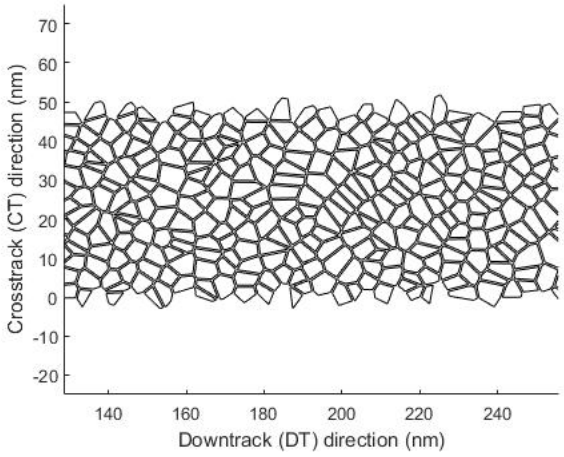

Fig. 5.2 Voronoi diagram with downtrack dimension = 256*1.5nm = 384nm and crosstrack dimension (CT) = 32 * 1.5nm = 48nm

For the generation of the Voronoi diagram, the media generation code takes into account a random seed that is used to generate a set of random numbers. It also includes an input based on the size of the media to be generated, the size distribution expected and the expected average grain size. Based on the different inputs, a distribution of points (the set of black dots in Fig. 5.1) is generated in a 2D space and a set of points is identified which lie closest to each individual point (each black dot in Fig 5.1) generated in the random distribution. The set of points closest to a certain point is determined by minimizing the Euclidean distance of all the points from this individual point generated in the random distribution. Fig. 5.2 shows an example of a Voronoi media generated from the code. This 2D media is then replicated in the direction which corresponds to the height of the media. The generated media has gaps in between that denote the non-magnetic grain boundaries which may be formed due to various reasons in the fabrication process. As mentioned before, the renormalization technique is used to implement micromagnetic simulations in this thesis. As shown in Fig. 3.4 (c) the renormalization cells are then overlaid on the Voronoi media. Fig. 5.3 shows an illustration of this process.

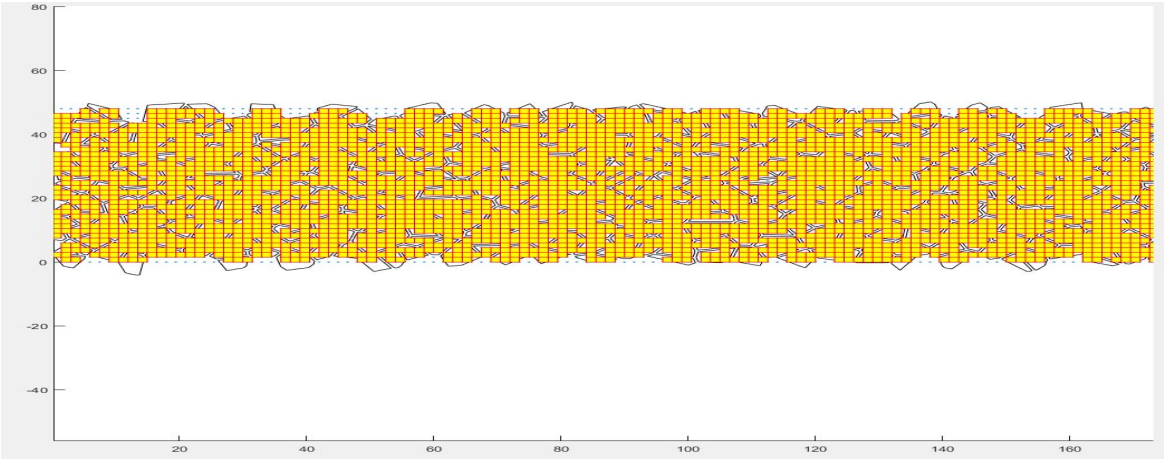

Fig. 5.3 Renormalized cells overlaid on the Voronoi media. The squares with red edges denote the renormalized cells

5.1.2 Recording process

The process of implementing the LLG equation to write specific patterns has already been described in Chapter 3 of this thesis. The process flow for these simulations has been described in detail in Fig. 3.3. There are two main patterns that would be encoded on the recording media. The single tone pattern consists of a bit series 1010…. where the 1 and 0 denote different magnetization directions recorded on the media. A more realistic pattern that is often recorded on the disk drives is the Pseudo Random Bit Sequence (PRBS) which consists of a string of 1's and 0's. PRBS sequences are used in communication systems, encryptions, time of flight spectroscopy measurement and other real world applications[125]. The PRBS sequence is a binary sequence generated by a deterministic algorithm. A generator polynomial is used to generate this sequence of a specific length Fig. 5.4 (a) and (b) show examples of single tone and PRBS sequences written on a Voronoi media.

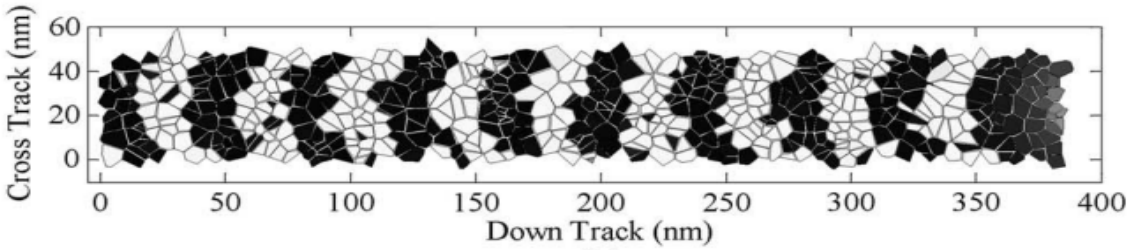

(a)

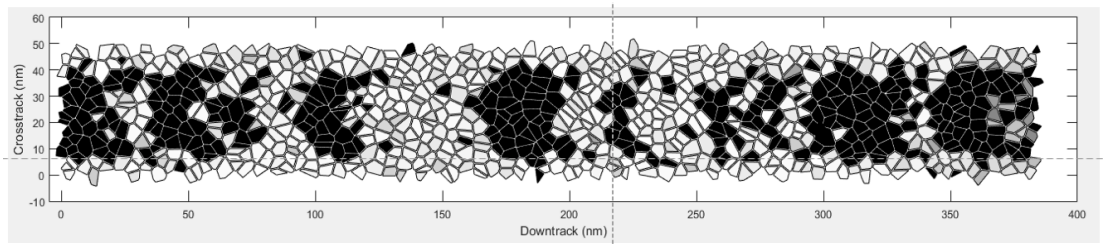

(b)

Fig. 5.4 (a) Single Tone sequence recorded on a Voronoi media[104] (b) PRBS sequence on a Voronoi media. Black and white regions correspond to magnetizations in different directions

5.1.3 Playback process

The playback process in the micromagnetic simulation is initiated by the magnetoresisitive read head. The playback signal is a convolution of the magnetic field from the media and the media magnetization. However, since it is difficult to accurately calculate the field from the media, the reciprocity principle is employed which states that the field from the media is equal to the field from the reader. Equation (5.1) shows the playback voltage generation for the media. The normalized head field is $\vec{h}$ and the media magnetization is $\vec{M}$. Fig 5.5 shows a schematic for the read head enclosed in between two shields used to avoid the detection from adjacent bits and ensure a sharp playback signal.

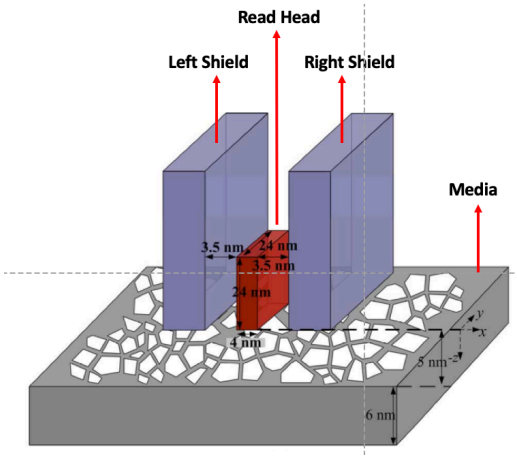

Fig. 5.5 Read Head and shields in the playback process[104]

$$V_{playback} = c\int_{-\infty}^{\infty} dx \int_{-\frac{\delta}{2}}^{\frac{\delta}{2}} \vec{h} \cdot \frac{d\vec{M}}{dx} dy \tag{5.1}$$

where δ is the thickness of the thickness of the media and c is a constant[32].

5.1.4 Types of noise

The noise in the micromagnetic simulation process is generated from two sources (i) the written patterns on the media (ii) the playback signals generated in the playback process. The noise from the written patterns may be one of two kinds[126][127] as seen in Fig. 5.6. When continuous patterns are written on the media (strings of 1's and 0's), there are some grains that don't switch based on the desired pattern. This could be because of the low/high energy barrier during switching, poor thermal gradient of the heat spot, insufficient field or high anisotropy of the grains and thermal fluctuations. It is difficult to reduce this noise since it depends on the grain size and the available head field. This is called DC or remanance noise. Electronic noise due to the use of components like preamplifiers and the post processing system like equalizers and detectors may also add an additional component to the DC noise. On the other hand, when the magnetization changes direction from 1 to 0 or vice versa, a transition occurs. The locations at which these transitions occur may change depending on the available field, the heat spot thermal gradient, misalignment of the read head and so on. The variation in the grain size may also cause a variation in the location of these transitions.

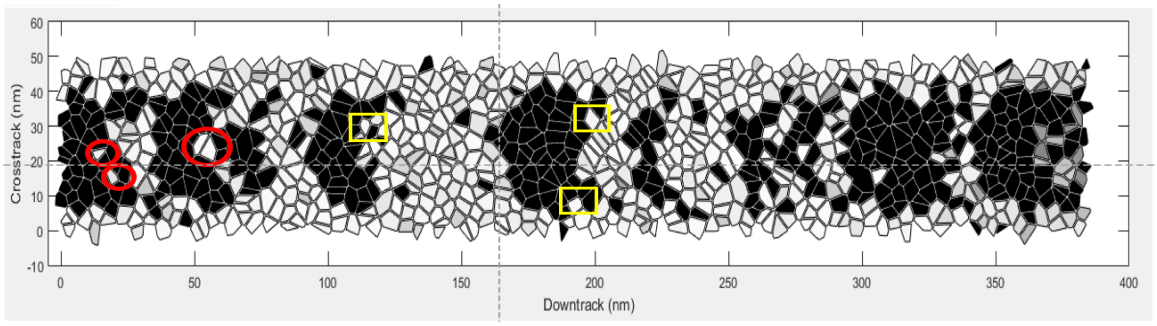

Fig. 5.6 Two kinds of media noise identified from the recording pattern. The red circles denote the DC or remanance noise. The yellow squares denote the AC or transition noise which is the noise in the boundary region as magnetizations switch.

This leads to the transition noise or AC noise. Mathematically, the standard deviation of the location at which these transitions occur is called the transition jitter. As the Linear Density (LD) increases, both these noises may increase. With different recording processes and optimizations, an attempt is made to reduce both kinds of noise.

5.1.5 Ensemble Waveform Analysis

It is easy to capture the total noise in the recording process. However, it is frequently necessary to also decompose the total noise into its components to identify the contribution of each of these components to the total noise. Mathematically, the main source of the transition noise is around the locations where the transitions occur. These locations can be captured in the playback signal. The remanance noise is significant in the region where long bits or patterns are written. This is the primary noise source when long PRBS patterns are written on the media where the number of transitions are few but the regions of no transitions and continuous signals are many. Thus, it is easier to identify the magnitudes of each of the noise components if their locations are known. The Ensemble Waveform Analysis package[128] provided by Seagate Technology allows the decomposition of the total noise (spatial noise) into its components, the remanance and transition noise. This decomposition is obtained by using appropriate windowing functions that capture the regions where the transition and remanance noise components

are significant. The total noise is a combination of the transition noise and the remanance noise.

5.1.6 Recording Performance Parameters

The recording performance parameters are essential to judge the efficiency of the recording performance. There are several techniques that can be used to measure the performance. The simplest performance parameter used to measure the HAMR process efficiency is the Signal to Noise Ratio (SNR). The SNR can be defined based on the signal and noise power used for its calculation. The SNR can is defined in equation 5.2 as

$$\text{SNR (dB)} = 10\log_{10}\left(\frac{\text{Signal Power}}{\text{Total Noise Power}}\right) \tag{5.2}$$

The Signal Power (SP) is the power of the noise free signal. This noise free signal is generated by averaging over all the playback signals generated in the recording process. Since the reader noise is very low compared to the media noise, in this thesis, it is assumed the reader generates negligible noise and thus the written patterns are readback only once. As explained before, the noise power has two components (i) the DC noise or remanance noise (ii) the AC noise or transition noise. The Ensemble Waveform Analysis package allows the identification of individual noise components and the decomposition of the total (spatial) SNR into its components, the remanance SNR and transition SNR. The other recording performance parameter commonly used is the transition jitter. It is the standard deviation of the locations at which transitions are written on the recording media. The formula for the transition jitter is shown in equation 5.3[104]

$$\sigma_{jit} = \sqrt{\frac{1}{N}\sum_{i=1}^{N}(x_i - \bar{x})^2} \tag{5.3}$$

Here N denotes the number of transitions, 'i' denotes the i'th transition, x_i denotes the location of the i'th transition and $\bar{x}$ denotes the corresponding transition location of the averaged noise free signal.

Other performance parameters like the Bit Error Rate (BER), the Shannon channel capacity (C) which denotes the useful information passing through a channel, the

Effective Bit Ratio (EBR) which is the ratio of the channel capacity to the Bit Length and the User Density (UD) can also be used to classify the recording performance. However, the signal detection system consisting of the Maximum Mean Squared Error (MMSE) equalizer, the Partial Response (PR) target, and the 1D Soft Output Viterbi Algorithm Detector is not used as a part of the recording setup to obtain results in this thesis.

5.2 Exchange Coupled Composite Media

The idea behind the development of the composite media is to extend the possible performance limits of different recording technologies and increase the achievable storage densities. The earliest efforts made to explore the improvement in the recording process is the development of the tilted media to extend the storage capacities for LMR in 2002[129][130]. Micromagnetic simulations were implemented to establish the viability of a tilted recording media where the initial magnetization is tilted with respect to the applied field for faster switching. Depending on the direction of movement of the media relative to the head, a good recording direction is defined as the direction of movement for the media when the observed magnetization transitions were sharp. The transition noise was low, and the relative motion was such that the head field direction on the leading side is in the direction of the tilted easy axis of the media. The other direction of motion was the bad direction where transitions were broadened, and high transition noise was observed. The dependence of the media performance on the demagnetization field was reduced and this design allowed the use of high anisotropy materials.

The aim of introducing the tilted media was to improve the ratio of the thermal stabilizing energy barrier to the switching field given by $\xi = (\frac{2\Delta E}{M_s H_s V})$ where ΔE is the energy barrier, M_s is the saturation magnetization of the material, H_s is the switching field and V is the volume. For the best PMR design, this ratio was found to be 1. With the tilted media at 45°, this ratio was increased to 2 indicating a clear advantage. However, fabrication issues prevented its wide usage in real world applications[130].

The next effort made in this regard was to develop composite media designs mainly for improving the PMR technology output. A composite media design was developed by Victora and Shen [131] with a soft and hard layer. The proposed structure worked on a similar principle as the tilted media proposed before but could be fabricated a lot more easily thus making it a more attractive proposition. Fig. 5.7 (a) shows the proposed design by Victora and Shen and Fig 5.7 (b) shows the switching mechanism for the optimized case where the minimum switching field (as a fraction of $2K_u/M_s$) is h=0.3. It was clear that the exchange coupling between the two layers should be optimized to ensure switching at the lowest field. A proposed solution to this issue was introducing a thin polarizable interlayer introduced between the soft and hard layer. However, unlike the antiferromagnetic coupling (AFC) used for most designs including the longitudinal

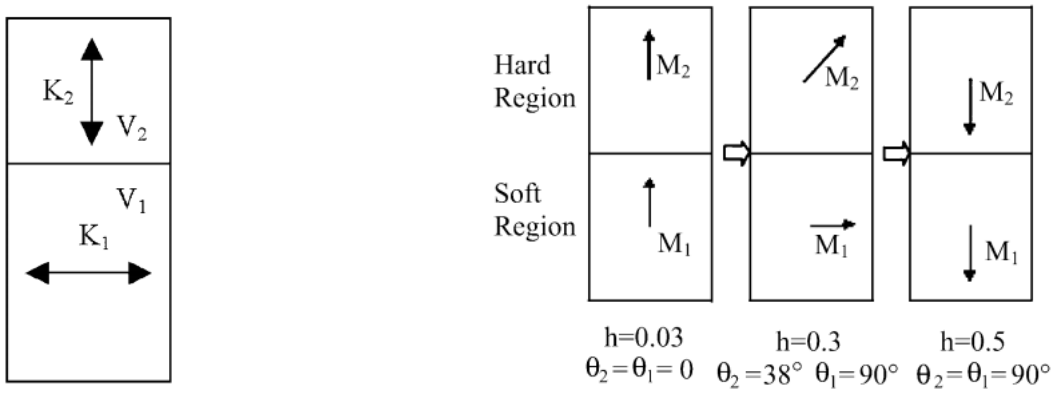

(a) (b)

Fig. 5.7 (a) Schematic of the composite media proposed by Victora and Shen[131]. The top layer is the hard layer and lower layer is the soft layer. (b) Switching mechanism for the composite media for the optimized case ($M_1 = M_2$ and $V_1 = V_2$)

recording media[132][133], this layer had to induce ferromagnetic coupling. Application of applied field initially causes the magnetization of the soft region to rotate and, thus, alter the exchange field angle applied to the hard layer. The exchange field helps the rotation of the magnetization of the hard region. For this design, the switching field distribution (SFD) shows high tolerance to the easy axis distribution. The switching field of composite media is about half that of perpendicular media. The switching mechanism

ensured high-anisotropy material could be used in composite media and a high-recording density can be obtained. Furthermore, the inability of strongly tilted fields to switch this media should greatly reduce adjacent track erasure. Further analysis of this structure was conducted by Kapoor, Shen and Victora[134] which used a micromagnetic approach to study the effect of intergranular exchange coupling on the switching mechanism of this structure. It was found that good exchange coupling was necessary between the hard and soft layers of this structure to facilitate the switching of the hard layer. In addition to this, for exchange coupled grains, it was found that nonuniform rotation was observed as a nucleation domain in the bottom region of the soft part. This nucleation moved its way up to and through the layer interface, if the interlayer exchange coupling was appropriate[134]. An effort was also made to fabricate the composite media design proposed by Victora and Shen. Wang, Shen and Bai in 2005[135] and 2006[136] fabricated a composite magnetic recording medium with exchange decoupled magnetic grains. A nonmagnetic interlayer with different thickness was put between the hard and soft layer to tune the exchange coupling and aid the switching process. With proper coupling, a significant drop of the coercivity field was observed for this design while still maintaining good thermal stability. This fabricated design also verified a better recording performance than the performance exhibited by single layer LMR and PMR designs. Since the soft layer actually aided the switching of the hard layer, this media design could also be named dynamic tilted media.

An independent effort to develop composite media designs was also undertaken by Thiele[137] whose group developed exchange spring media. The principle design was similar to the media developed by Victora and Shen. It still consists of two layers where the exchange coupling between the layers aids the switching of the high anisotropy layer. In this design, the FeRh layer is the soft layer whereas the high anisotropy FePt layer is the layer. The FeRh layer is antiferromagnetic at room temperature but on heating up to the writing temperature T_w (which was greater than the Neel temperature T_N) FeRh undergoes a phase change and becomes ferromagnetic with high moment and low anisotropy (thus acting like a soft layer). This reduces the switching field considerably

compared to single layer structures. The average switching field for this bilayer structure is given by

$$H_0 = \frac{K_{u,FePt}t_{FePt}+K_{u,FeRh}t_{FeRh}}{M_{s,FePt}t_{FePt}+M_{s,FeRh}t_{FeRh}} \approx \frac{K_{u,FePt}t_{FePt}}{M_{s,FePt}t_{FePt}+M_{s,FeRh}t_{FeRh}} \quad (5.4)$$

Since the moment (M_s) for FeRh is significantly high at the writing temperature, this aids the switching of the FePt layer at temperatures well below $T_{c,FePt}$. The written data is then stored at a temperature $T_s < T_{N,FeRh}$ where FeRh is in the antiferromagnetic state and the exchange coupling between the FeRh and FePt layers as well as the high anisotropy for FePt allows for thermal stability. In the study of the structural and magnetic properties of this structure, it was observed that the exchange coupling between the layers allows switching via an exchange spring mechanism that fully reverses the magnetization of the FePt layer, rather than merely reversibly rotates it[138]. A micromagnetic study of the exchange spring media was conducted by Seuss[139]. Optimizations were used to obtain the best gain in the energy barrier by about 70% for a bilayer structure with zero anisotropy for the soft layer. The switching time for the spring media for external fields applied 10º off the easy axis was about 0.4 ns which is comparable to single-phase media[139].

The problem associated with this structure is the variations during the experimental fabrication process. Fabricating a thin FeRh layer that can still undergo the expected phase transition at T_w with the required grain size control is extremely difficult. Additionally, from [138], it is clear that to attain high SNR values compatible with a storage density of 1Tb/in^2, the required grain size in the bilayer structure is about 5nm. Controlling the FePt grain size in a fabrication process that includes sputtering with the MgO/C seedlayer while maintaining the exchange between the FeRh and FePt layer for efficient exchange spring behavior is extremely difficult.

5.3 Thermal Exchange Coupled Composite Media

In the HAMR media fabrication process, granular size variation leads to a significant T_c variation. In the HAMR writing process, the efficiency of recording desired patterns is sensitive to the magnetic parameters for the granular HAMR media. The variation in the grain size leads to a T_c variation that causes major issues for the integrity of the written patterns and accurate detection of the encoded bit pattern. Previous chapters have described in detail how the granular T_c variation is one of the biggest noise sources in the HAMR process. The Thermal Exchange Coupled Composite (ECC) media proposed by Victora and Liu[140] aims to address this issue and provide a new counter to address the magnetic trilemma. The Thermal ECC media aims to decouple the issue of writing and storage by proposing a design where the bilayer structure consists of two layers. Fig. 5.8 (a) shows the design for the Thermal ECC media. The primary difference between this media and the other composite media proposed before is the write layer (the softer layer) still has a significantly high anisotropy (~10^7 erg/cm^3) at 300K. This is in opposition to the previously proposed composite media structures where the soft layer has extremely low anisotropy.

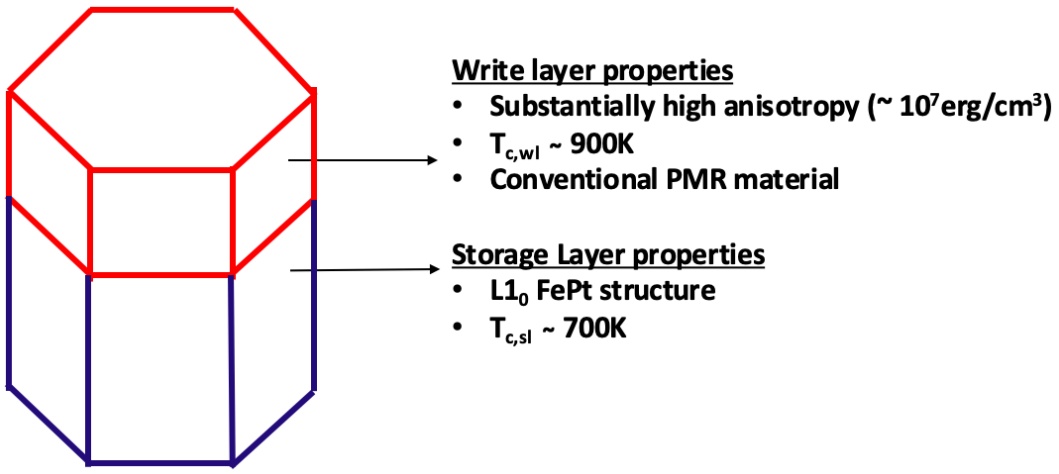

Fig. 5.8 (a) Design of the high temperature Thermal ECC media

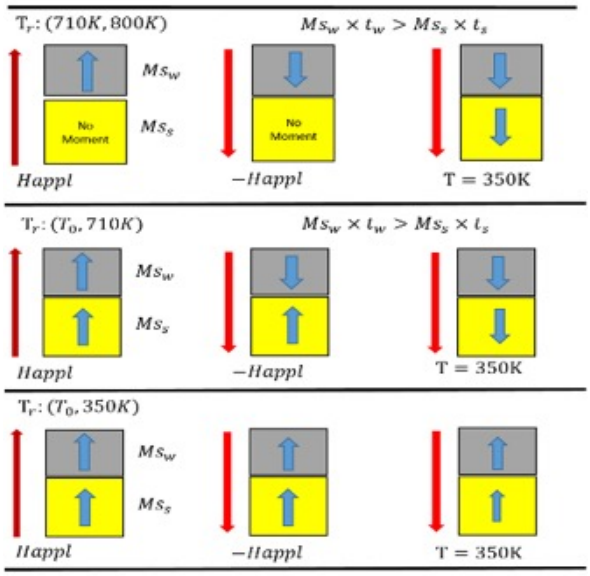

Fig. 5.8 (b) Working principle of the high temperature Thermal ECC media[140]

For the Thermal ECC media, the writing process in HAMR is restricted to the write layer. The write layer can be a conventional PMR material (like CoPt, FePd or doped FePt) and it has a T_c value ($T_{c,wl}$) greater than the T_c of the storage layer ($L1_0$ FePt where $T_{c,sl}$ = 700K). To implement the micromagnetic simulations with this design, the T_c for the write layer is 900K. Since $T_{c,wl} > T_{c,sl}$, the magnetic parameters of the write layer can be adjusted so that the writing temperature (T_{write}) > T_c of FePt. This makes the writing process independent of the T_c variations in FePt thus negating one of the biggest noise sources plaguing the HAMR process. The writing process uses superparamagnetic writing or writing with controlled thermal fluctuations. Fig. 5.8 (b) shows the working principle of this ECC media. T_0 denotes the maximum temperature at which the write layer switching probability is zero. In the first row, when the temperature $T_r > T_{c,sl}$, the storage layer is paramagnetic and write layer magnetization follows the direction of the external field. When the media is cooled down to room temperature (350K), the magnetization direction in the storage layer follows the direction of the write layer. In other words, the storage layer allows long term storage of the data written in the write layer due to its high anisotropy and the interlayer exchange coupling that exists between the layers. In the middle row, when the temperature T_r > 350K and $T_r < T_{c,sl}$, since the

writing process is restricted to the write layer and the moment of the write layer($Ms_w \times t_w$) is greater than the storage layer moment($Ms_s \times t_s$), only the magnetization of the write layer switches in the presence of the external field. Once the media is cooled, the magnetization of the storage layer follows the direction of the write layer. In the last row when the writing temperature is lower than 350K, the writing process fails since the anisotropy of the write layer is too high. Thus, the magnetization does not switch.

Fig. 5.9 (a) shows the switching performance of the Thermal ECC media. The Switching Probability Distribution (SPD) is a differential of the Switching Probability (SP) and is Gaussian in nature[141]. The smaller value of the Full Width Half Maximum (FWHM) of SPD indicates a sharper switching performance. For the Thermal ECC media, the red curve shows that the FWHM of the SPD for the Thermal ECC media is 42K and the writing temperature (temperature at which the SPD has a minimum value) is 738K.

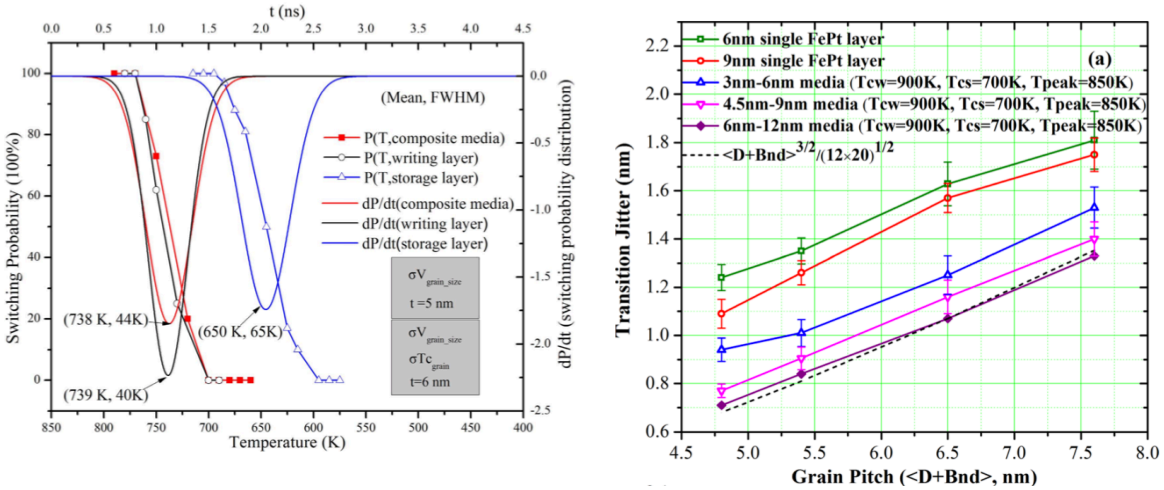

(a) (b)

Fig. 5.9 (a) Switching Performance of the Thermal ECC media denoted by the red curve. The black and blue curves show the switching performance of the write and storage layer respectively. The Gaussian SPD is calculated by differentiating the Switching Probability curve which is an error function (b) Recording Performance of the Thermal ECC media compared to the conventional Single Layer FePt media[141].

Compared to the single layer FePt media with a FWHM value for the SPD = 65K, the Thermal ECC media has a lower SPD FWHM (44K) and thus a better switching performance. Fig. 5.9 (b) shows the recording performance of the Thermal ECC media with different thicknesses. Compared to the conventional single layer FePt media, the Thermal ECC media has an improved recording performance, given the low jitter values. As the ECC media thickness increases, thermal stability increases thus decreasing the DC noise for the structure. This leads to an improvement in the recording performance. Based on the improvement achieved by using thicker ECC media, especially with respect to the high User Density (UD)[141] the 4.5nm (write layer thickness) - 9nm (storage layer thickness) Thermal ECC media is considered to be a good design.

The fabrication of thicker ECC media involves the deposition of thicker recording layers. This requires longer sputtering times decreasing the throughput of the fabrication system[51]. Additionally, sputtering for thicker media also requires high power which can lead to a deterioration of the recording media surface with increased roughness causing difficulties for the flying head above the media. To avoid this, thicker layers can be deposited in multiple chambers though this increases the production cost substantially. Finally, fabrication of thicker media also entails the growth of small diameter grains which is difficult considering the high annealing temperatures for the FePt media. Considering these fabrication issues, it is necessary to explore the use of thinner ECC media than the current 4.5nm-9nm media. However, thinner 3nm-6nm ECC media are more susceptible to DC noise and thermal fluctuations although they are much easier to fabricate. This chapter deals with the optimization processes implemented for the thinner 3nm (write layer thickness) – 6nm (storage layer thickness) Thermal ECC media to reduce the DC noise[142]. The other aim is to improve the SNR of the recording performance with this thinner media and to make it comparable to the performance of the thicker 4.5nm-9nm Thermal ECC media.

5.4 Simulation Setup

The focus of this chapter is to introduce optimization approaches that have remained unexplored till this point. There have been several approaches used to improve the SNR, like increasing the Bit Length[143], changing the head velocity[104], changing the applied field angle and magnitude[104], system design optimization[144], decreasing the shield to shield spacing, decreasing the fly height and so on. The approaches introduced here mainly counter the DC noise in the Thermal ECC media. To explore the SNR improvement techniques in greater detail, micromagnetic simulations based on the Landau-Lifshitz-Gilbert (LLG) equation is implemented. The renormalized cell size is 1.5nm×1.5nm×1.5nm. The composite structure has two layers, a 3nm superparamagnetic writing layer and 6nm FePt storage layer. The magnetic profiles of the write layer are similar to [141] except that a small typo has been corrected. The arguments for $M_{s,wl/sl}$, $K_{u,wl/sl}$ and $A_{ex,wl/sl}$ are defined to be (T-300)/($T_{c(wl/sl)}$ -300) where 300 is the room temperature. For example, a temperature of 300º corresponds to 0. Using this notation, we can write the storage layer properties: $M_{s,sl}(0) = 922.3$ emu/cm^3; $K_{u,sl}(0) = 4.11 \times 10^7$ erg/cm^3 and $A_{ex,sl}(0) = 1.1\times10^{-6}$ erg/cm. The write layer profile can then be written as

$$M_{s,wl}\left(\frac{(T-300)}{T_{c,wl}-300}\right) = M_{s,sl}\left(\frac{(T-300)}{T_{c,sl}-300}\right) \times \frac{M_{s,wl}(0)}{M_{s,sl}(0)} \tag{5.5}$$

$$K_{u,wl}\left(\frac{(T-300)}{T_{c,wl}-300}\right) = K_{u,sl}\left(\frac{(T-300)}{T_{c,sl}-300}\right) \times \frac{K_{u,wl}(0)}{K_{u,sl}(0)} \tag{5.6}$$

$$A_{ex,wl}\left(\frac{(T-300)}{T_{c,wl}-300}\right) = A_{ex,sl}\left(\frac{(T-300)}{T_{c,sl}-300}\right) \times \frac{A_{ex,wl}(0)}{A_{ex,sl}(0)} \tag{5.7}$$

In the micromagnetic simulations, $T_{c,wl}$ = 900K, $T_{c,sl}$ = 700K, $M_{s,wl}(0)$ = 550emu/cm^3, $K_{u,wl}(0) = 1.0 \times10^7$erg/cm^3. The exchange coupling between these two layers is taken to be $\sqrt{A_{ex,wl} \times A_{ex,sl}}$. The calculated SNR values are based on the playback signals obtained by writing on eight different magnetic media with an average grain pitch (GP) of 5.5 nm. A 31 bit Pseudo Random Bit Sequence (PRBS) generated by a generator

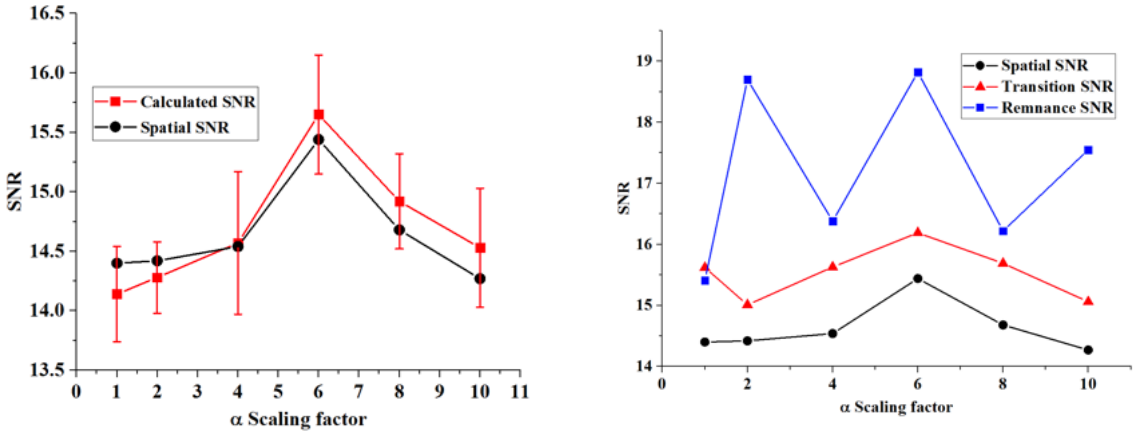

(a) (b)

Fig. 5.10 (a) Total SNR calculated from our approach (Calculated SNR) and the Ensemble Waveform Analysis Package (Spatial SNR) for damping scaled to different extent only in the write layer (α Scaling factor) (b) Components of the spatial SNR (transition and remanance SNR) plotted for different values of scaled damping in the write layer[142]

polynomial x^5+x^3+1 represents the read head field profile. Each bit of the polynomial is denoted by either 1 (negative applied field) or 0 (positive applied field) with the field being applied at an angle of 22.5° to the easy axis direction (+z). Appropriate padding bits are used at either end of the sequence to avoid edge effects of the media. A Gaussian heat spot with peak temperature 850K is used to heat the HAMR media to record the desired PRBS with the padding bits. To understand the reasons behind the variations in the calculated SNR, the total SNR (spatial SNR) is further broken down into transition SNR and remanence SNR. The spatially noise-free signal is simply an average of all spatially noisy signals. The total spatial noise is calculated by subtracting each noisy signal from the averaged noise free signal. Total SNR is calculated from the definition using the power of the noise free signal and the total power of the different spatially noisy signals. The transition and remanence contributions to the total SNR are obtained by applying appropriate windowing functions to the total spatial noise. To obtain the transition component of the spatial SNR, the windowing function for transition noise is non-zero close to the transitions and zero everywhere else. The remanance noise is the difference

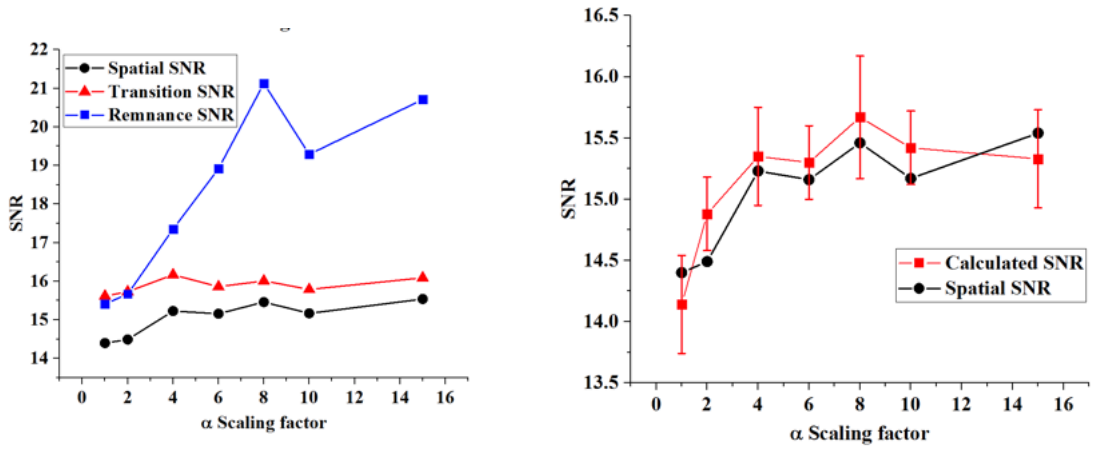

(a) (b)

Fig. 5.11 (a) Total SNR calculated from our approach (Calculated SNR) and the Ensemble Waveform Analysis Package (Spatial SNR) for damping scaled to different extent only in both the write and storage layer (α Scaling factor) (b) Components of the spatial SNR (transition and remanance SNR) plotted for different values of scaled damping in both the write and storage layer[142]

between the total noise and the transition noise. The Ensemble Waveform Analysis[128] package introduced before enables this functionality. However, it is unable to generate error bars for the results. Thus, it is an interesting exercise to compare the Calculated SNR values from the approach used in our simulations to the spatial SNR values generated from the package.

5.5 SNR dependence on damping

Damping represents the rate at which the magnetization approaches equilibrium. To understand the effect of varying the damping in the write layer of the composite media, the damping is scaled uniformly across the write layer. This scaling is denoted as the damping scaling factor in Fig 5.10 (a) and (b). The effect of damping increase can be understood as follows: within the limited time that the heat spot is incident on a certain bit on the media, increasing the damping ensures that the grain is switched as the Zeeman

energy due to the applied head field overcomes the anisotropy energy at high temperatures. Higher damping values ensure that more grains switch at these temperatures. This increases the calculated SNR as shown, by almost 1.5 dB thus indicating a decrease in the noise power by almost 30%. However, increasing the damping after a certain value may delay the write process at the write temperatures where damping is already enhanced. This leads to stray transitions in the write layer after the information is stored in the storage layer. This results in decreasing the SNR to a certain extent. The total SNR calculated from the ensemble waveform analysis is denoted as spatial SNR in the same figure. A comparison between the two shows accuracy at every data point within the given error bars of the calculated SNR. It can be seen that the total SNR values agree to a good degree even for the limited number of simulations. The SNR variation clearly denotes that the transition SNR follows the trend of the total SNR thus indicating that the SNR variation process is largely affected by the transition/jitter noise. The strong variations in the remanence SNR is likely caused by an inadequate number of bits to fully represent this much smaller noise. The low remanance noise also signifies a substantial reduction in the DC noise due to this optimization approach.

The effect of damping variation on SNR is extended to include the entire composite structure (both the write and the storage layer) in Fig. 5.11 (a) and (b). The trends are very similar except at the largest values, which are no longer detrimental. The results suggest that optimization of damping only need be done in the write layer, which is helpful given that the write layer also has more design flexibility, and thus opportunity for optimization.

5.6 SNR dependence on Intergranular Exchange Coupling

Introducing exchange coupling between grains of the HAMR media increases the total exchange field in the simulation. The intergranular exchange coupling allows adjacent grains to assist each other in the switching process. Thus, it can aid in the switching process and allow thermally unstable grains to retain the desired configuration. This may help reduce the overall DC noise. However, high exchange coupling beyond a certain

value may be undesirable since it may lead to the formation of clusters that affect the written patterns and increase the jitter[35].

The intergranular exchange coupling (IGC) in these simulations is introduced as a finite fraction of the renormalized exchange at different temperatures In the presence of the heat spot, these grains that form clusters have a higher thermal stability factor (K_uV/k_BT) and hence are less susceptible to thermal fluctuations and superparamagnetic effects due to low K_u values. This leads to successful switching under the applied head field and ensures fewer stray transitions. It should reduce remanence noise. However, as the intergranular exchange increases beyond a certain value, the particles form larger clusters that create noise, particularly jitter. To observe the effect of varying intergranular exchange coupling (IGC) in the write layer, the IGC is uniformly scaled for all the grains in the write layer only. As expected, from Fig. 5.12 (a), the calculated SNR shows an increasing trend to start with, with a significant increase in the SNR of almost 2.2 dB and a consequent decrease as the IGC goes beyond 10%. The agreement between the calculated SNR values and the spatial SNR values remains as seen in Fig. 5.12 (b). Both the transition SNR values and the remanence SNR values follow similar trends as the spatial SNR value. However, their absolute magnitudes help ascertain that the effect of the jitter/transition noise is the deciding factor yet again in causing the aforementioned SNR variation. To extend this understanding, the intergranular exchange is varied throughout the composite structure uniformly in Fig. 5.13 (a) and (b). The calculated SNR initially increases as the intergranular exchange is increased to 5% of the exchange coupling values in each of the layers. The increase is almost 1.5 dB denoting a decrease of almost 30% in the noise power of the playback signal. The SNR then decreases as the spatial SNR (transition and remanance SNR) plotted for different values of finite Intergranular Exchange Coupling (IGC) introduced between the grains in the ECC media IGC value increases. Interestingly, the peak is found at a lower value of IGC, presumably because all layers are now exchange coupled. This limits the overall SNR increase because the higher values of exchange are no longer accessible: it suggests that exchange

coupling should be limited to the write layer and the FePt grains should continue to be magnetically isolated.

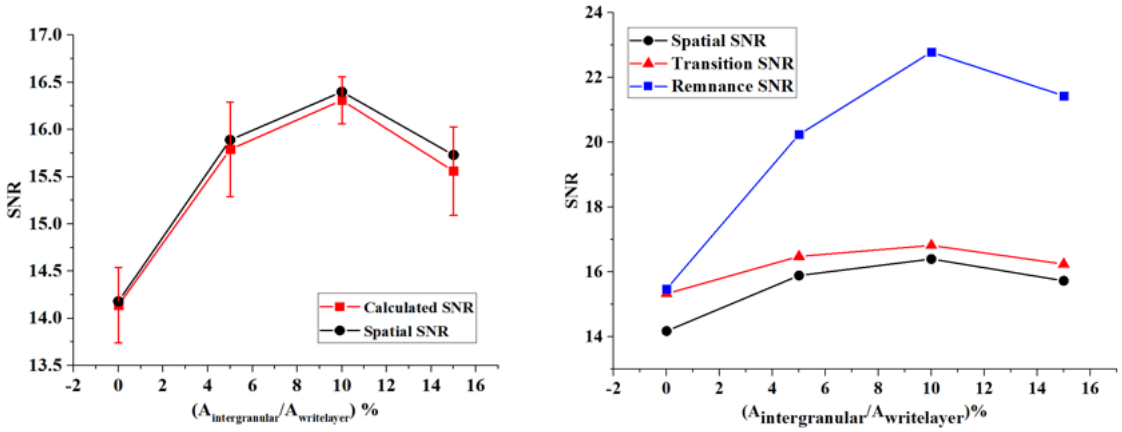

(a) (b)

Fig. 5.12 (a) Total SNR calculated from our approach (Calculated SNR) and the Ensemble Waveform Analysis Package (Spatial SNR) for finite Intergranular Exchange Coupling (IGC) introduced between the grains in the write layer (b) Components of the spatial SNR (transition and remanance SNR) plotted for different values of finite Intergranular Exchange Coupling (IGC) introduced between the grains in the write layer[142]

5.7 Thermal ECC media storage layer optimization

In both the approaches used to improve the SNR in Section 5.5 and 5.6, it is easy to observe the SNR improvement when the implemented optimization approaches are restricted to the write layer and the storage layer is excluded from the optimization process. This is an important conclusion, especially given that the write layer is a conventional PMR material with several choices and flexibility for optimization by variation of media parameters. However, the storage layer is $L1_0$ FePt with a T_c = 700K. It is difficult to scale the damping or introduce intergranular exchange coupling without affecting the magnetic properties of individual grains or introducing metallic interlayers (for intergranular exchange coupling) which may enhance the thermal bloom. To explore

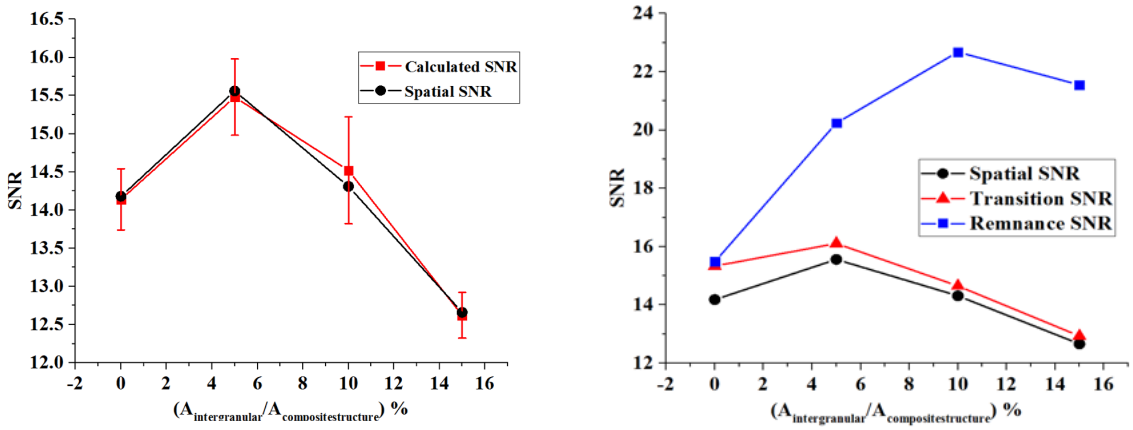

(a) (b)

Fig. 5.13 (a) Total SNR calculated from our approach (Calculated SNR) and the Ensemble Waveform Analysis Package (Spatial SNR) for finite IGC introduced between the grains in the ECC media (b) Components of the spatial SNR (transition and remanance SNR) plotted for different values of finite IGC introduced between the grains of the ECC media[142]

the potential for further increase in the SNR, two cases are simulated (i) In the first case, damping in the write layer is scaled to six times its original value since this is the optimized value which led to the highest spatial SNR (from Fig. 5.10(a)). This is followed by scaling the damping gradually in the storage layer and the effect on the SNR is observed. (ii) In the second case, a 10% IGC is introduced between the grains in the write layer, since this led to the highest spatial SNR (Fig. 5.12(a)). Finite IGC is then introduced between the grains of the storage layer and the variation in the SNR is observed. The results for case (i) and (ii) are plotted in Fig, 5.14 (a) and (b). It is clear that there is no further scope for optimization for the media since neither of these approaches actually help improve the SNR further. This is an extremely important conclusion since it indicates the practical nature of the proposed optimization approaches.

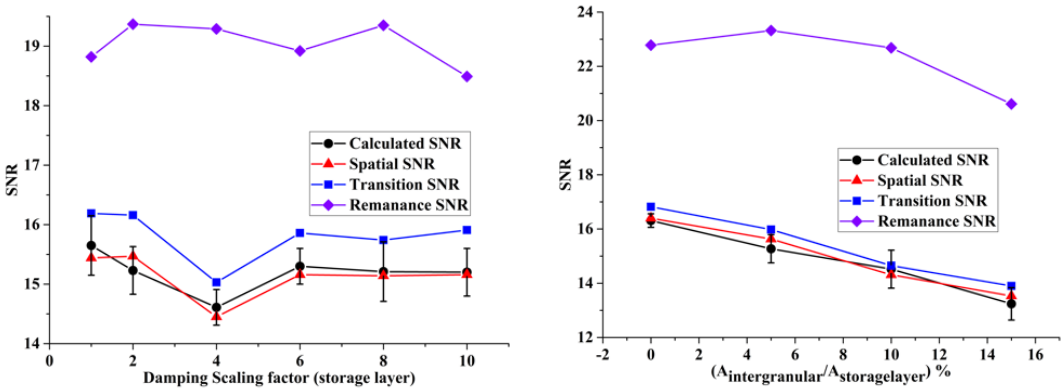

Fig. 5.14 Optimizations implemented exclusively in the storage layer for the Thermal ECC media (a) Damping scaled in the storage layer after damping in the write layer is scaled to six times its original value (b) Exchange coupling introduced between grains of the storage layer after a 10% exchange coupling is introduced between grains of the write layer

5.8 SNR dependence on temperature

In HAMR, a laser source is incorporated in and moves together with the write head, and heat energy is delivered to the recording layer through a near-field transducer. A small rate of temperature change is important for successful grain switching. Usually, in HAMR, we also desire to have a large temperature gradient for sharp transitions. These competing factors cause the most optimum heat spot temperature to be greater than the writing temperature of the medium within a few hundred Kelvin. In the micromagnetic simulation, the peak heat spot temperature is varied up to a maximum value of 900 K as based on previous simulations for single layer FePt. Three different cases are addressed here: (i) Media with no T_c & K_u/H_k variation (ii) Media with 3% T_c variation and no K_u variation (iii) Media with 3% T_c variation and 15% K_u variation. The variation of the calculated SNR for no T_c and K_u variation values shows a slight increase in the SNR as the peak spot temperature reaches 800K and then a slight fall (Fig. 5.15 (a)). Extending the simulation to include the media with T_c & K_u variation produces an interesting observation: the maxima in SNR is observed to shift to the right as the peak temperature

is varied. The effect is shown in Fig. 5.15 (b) where, in both cases, the maximum SNR is observed to shift towards a peak temperature of 850K as compared to 800K in the absence of any T_c/K_u variation. Increasing the peak temperature and maintaining the same write temperature (which happens when intrinsic media variations are included)

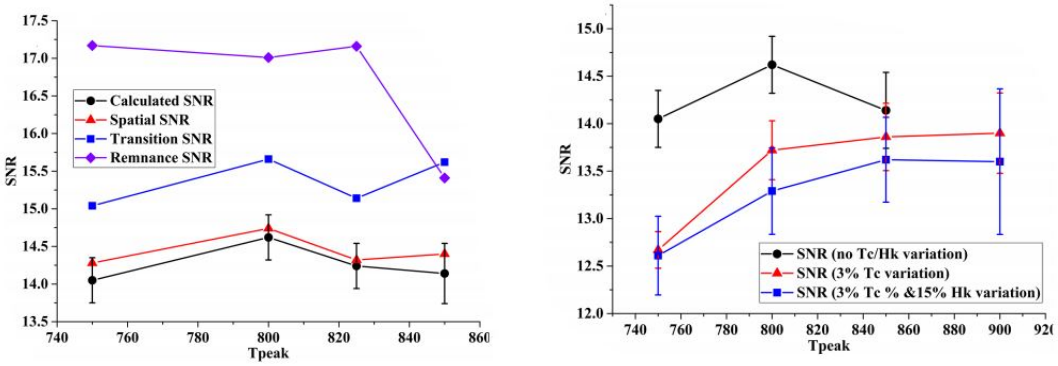

(a) (b)

Fig. 5.15 (a) Variation of calculated SNR and individual components vs heat spot peak temperature (no T_c/H_k media variation) (b) Effect of T_c and H_k variation on SNR[142]

ensures that writing takes place at a higher thermal gradient (farther away from the peak temperature) in the temperature profile as compared to the case with no variations. This helps explain the shift of the SNR maxima towards the right at a higher peak temperature.

5.9 Summary

This study was possible due to funding from ASTC/IDEMA. Optimization approaches have been introduced in this chapter to reduce the DC noise in the relatively thinner 3nm-6nm Thermal ECC media. A clear increase in the SNR is observed as the damping is scaled and finite exchange coupling is introduced between the grains of the write layer. Both these approaches are best restricted to the write layer since this ensures that the high SNR values remain accessible. With an improvement in the SNR, there is a potential for the thinner ECC media to be used as a potential substitute to the thicker 4.5nm-9nm Thermal ECC media that is harder to fabricate.

Chapter 6

Low temperature Thermal ECC media

Chapter 2 in this thesis explained in detail various components of the HAMR system. The basic idea of the HAMR process is to heat the HAMR media to temperatures close to the T_c value. In the use of the Thermal ECC media, this becomes an even greater issue of importance since the temperatures to which the media may be heated up are even more than the T_c value of FePt. Depending on the purpose of the HAMR process and the sequences that are written, the writing process may take several ns to finish. An important figure of merit for the Hard Disk Drive industry is the longevity of the HDD's developed. Commercial HDD's would be expected to write and store data for at least ten years or more. This indicates that the high temperatures in the HAMR process would have to be sustained by the components of the HAMR system for several years with minimum possibility of failure.

In the HAMR system, the NFT assembly is responsible for heating the media. With the long term usage of this heating system, there are three sources leading to significant heating of the NFT and its consequent protrusion[83] (i) Scattering of heat from the NFT (ii) backheating from the media (iii) thermal fly height control power and writer current. The most common material used in the lollipop NFT for the rectangular peg is gold (Au)[145]. Although Au has a noble character, is a good conductor of heat and has a significantly high melting point, use of such high temperatures over a long period of time leads to thermal instability (heating and consequent melting) of the rectangular peg and additional head induced contamination[146]. This may lead to a worsening thermal gradient on the media, a lateral spread of the heat spot and additional Adjacent Track Erasure (ATE) and other undesirable effects. The high temperature conditions also damage the media over a period of time leading to protrusions in the media. Although these protrusions have been measured to be small (~0.4nm)[147], the challenge of decreasing the fly height for the head from the media may face obstructions[148]. This

can also lead to an increased possibility for collisions between the head and the media. Finally, the use of high temperatures in the HAMR process can also lead to a decomposition or evaporation of the lubricant used to protect the media. These high temperature and heating issues constitute one of the biggest impediments to the commercial release of HAMR technology[149].

This issue is especially pronounced in the Thermal ECC media proposed in the previous chapter. For this media, the writing temperature increases from the 650K to 738K. Thus, although this media enjoys several advantages over the single layer FePt media in terms of the improved switching and recording performance, it is clear that the heating issues in the HAMR process are more critical for this media. To counter these heating issues, a low temperature Thermal ECC media has been proposed. The idea is to propose a media design that works on the same principle as the previously proposed high temperature Thermal ECC media but has a significantly lower writing temperature. In order to reduce the system temperatures in the HAMR process, the low temperature Thermal ECC media is designed such that it can record successfully in the presence of a Gaussian heat spot with a lowered peak temperature. At the same time, it is also verified that this media enjoys the same superior switching and recording performance as the high temperature Thermal ECC media.

6.1 Proposed ECC media design

In the fabrication process for HAMR media, one of the ways of reducing the ordering temperature is alloying or doping using different elements. This process can affect the magnetic properties of the material by reducing its T_c. Fig. 6.1 (a) shows an example of using Ni for doping FePt[76] and the decrease in the coercivity due to the doping process. With increasing extent of Ni doping, it is easy to notice the decrease in T_c. This idea is used to propose the Thermal ECC media design. The low temperature Thermal ECC media is a bilayer structure with the T_c of the write layer reduced from 900 K and storage layer (FePt) reduced from 700 K. For the storage layer, doped $L1_0$ FePt material with reduced T_c of 500 K is assumed. For the write layer, we model a similar $L1_0$ material like

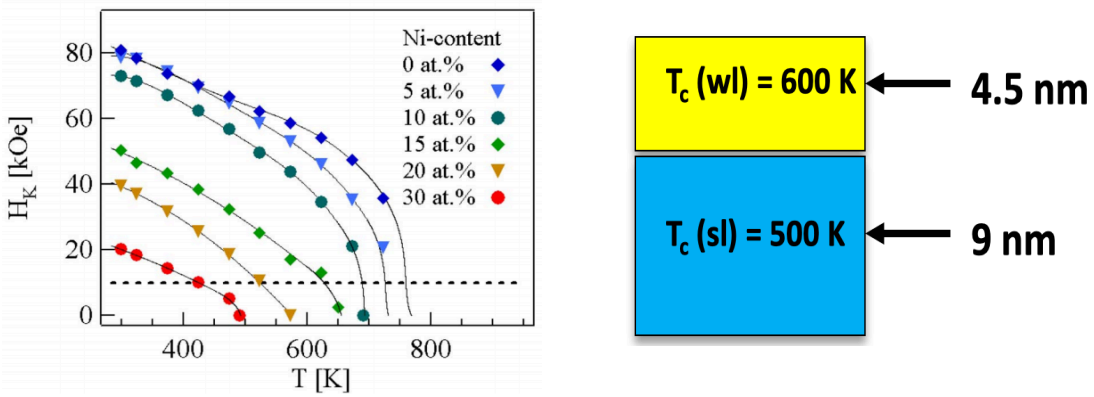

(a) (b)

Fig. 6.1 (a) Effect of Ni doping on the coercivity H_k (or anisotropy) of FePt[76][111] (b) Schematic of the proposed low temperature Thermal ECC media[149]

CoPt or FePd doped to reduce its T_c down to about 600 K. The design is shown in Fig. 6.1 (b).

To lower the overall system temperature, the simulations are recorded on the thermal ECC media with a Voronoi grain structure with a peak heat spot temperature of 650K as opposed to 850K, the peak heat spot temperature used to write on previously proposed media. In all the simulations, we use an average grain diameter of 4.5nm (Grain Pitch GP = 5.5nm) with a Grain Size Distribution (GSD) = 20%. The switching behavior and recording performance (characterized by the transition jitter and SNR) are evaluated via micromagnetic simulations on a 384nm × 48nm × 13.5nm sample with the thickness of write and storage layer being 4.5nm and 9nm respectively. Transition jitter is calculated for a single tone sequence with BL = 20nm and a head velocity of 20m/s with ~320 transitions written using a uniform head field of 8kOe applied at an angle of 22.5° to the z axis. 16 different media samples are used to get adequate statistics. Unless otherwise mentioned, a correlated σ_{Ku} = 15% and σ_{Tc} = 3% with correlation coefficient = 1 is used in both layers of the media. To model the low temperature Thermal ECC media with the T_c values mentioned above, the storage layer is modeled first. The magnetic parameters for the storage layer are found using the renormalization approach described in Chapter 4.

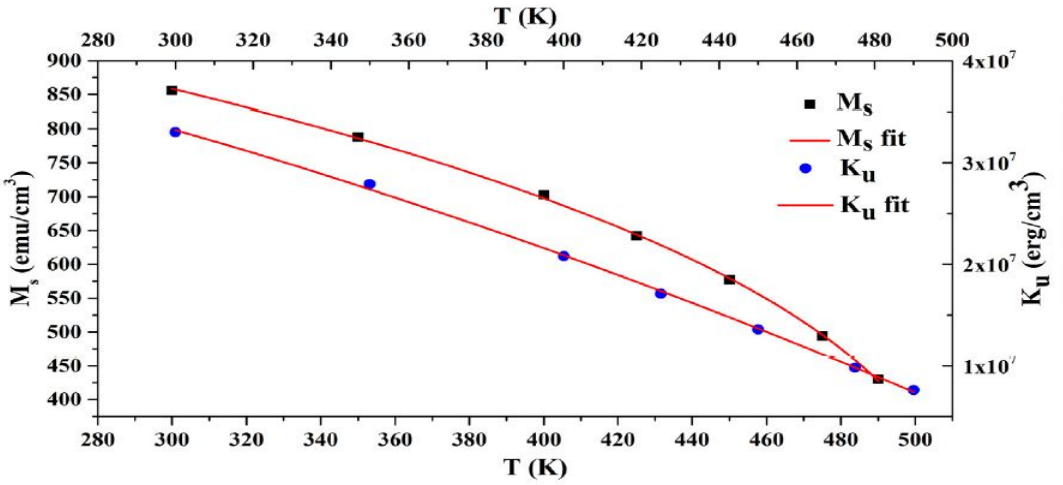

(a)

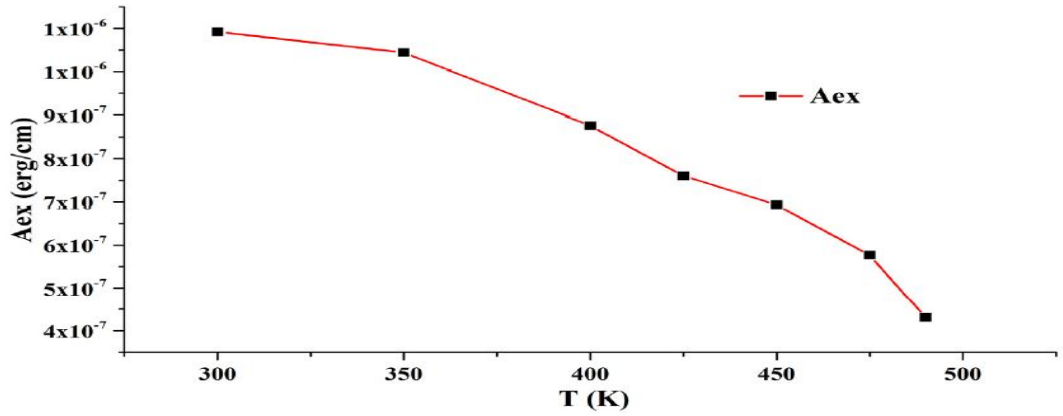

(b)

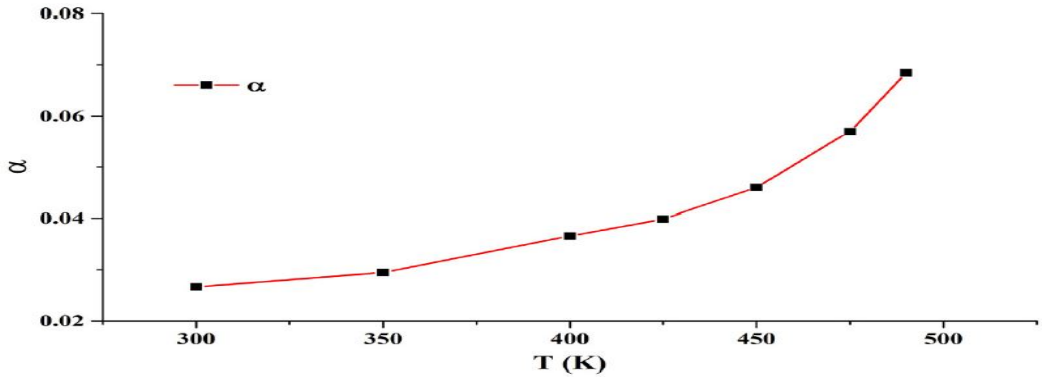

(c)

Fig. 6.2 (a) – (c) Renormalization parameters for doped $L1_0$ FePt with T_c = 500K[149]

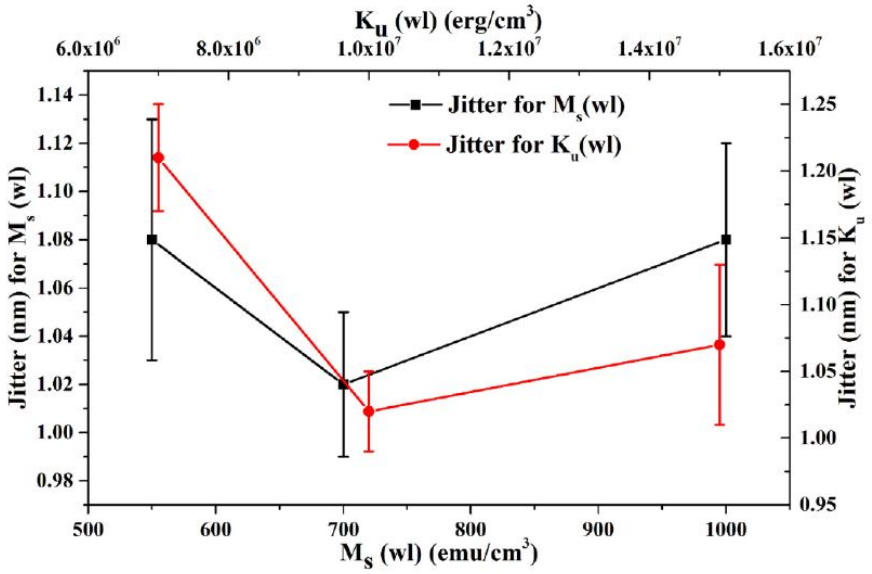

(a)

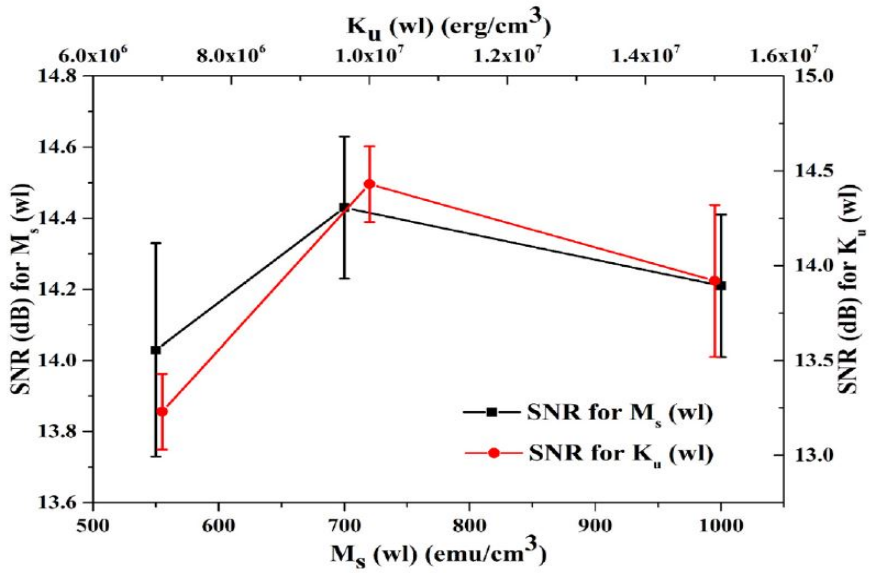

(b)

Fig. 6.3 (a) Jitter and (b) SNR for different values of $M_{s,wl}$ and $K_{u,wl}$ at 300K[149]

The parameters are calculated for a 1.5nm × 1.5nm × 1.5nm renormalized cell size by invoking two cost functions[108][113]that evaluate the differences between the atomistic parameters and their renormalized counterparts at different temperatures. An anisotropic $L1_0$ FePt model is considered for calculating the atomistic and renormalized values. The

anisotropic FePt model corresponds to a FePt lattice structure with five different atomistic exchange values representing five different types of neighbors as has been described before in this thesis. Fig. 6.2 (a)–(c) show the resulting magnetic parameters at the reduced length scale. From these calculations, we derive the following properties for FePt ($T_c = 500K$) at 300 K: $M_s = 856 emu/cm^3$, $K_u = 3.3 \times 10^7 erg/cm^3$ and $A_{ex} = 1.1 \times 10^{-6} erg/cm$. Calculations yield a thermal stability factor ($K_u V/k_B T$) of ~72 at 300K for an average grain size = 4.5nm. Micromagnetic simulations with a Gaussian heat spot of FWHM = 40nm are implemented to optimize the M_s and K_u of the write layer at 300K. Renormalized parameters for the write layer are obtained by scaling as described in [149] and equation (5.5) – (5.7). Fig. 6.3 (a) and (b) show the jitter and SNR are simultaneously optimized without a need for different write layer magnetization or anisotropy. Increasing the $M_{s,wl}$ and decreasing the $K_{u,wl}$ beyond the values shown in Fig. 6.3 (a) and (b) reduces the write temperature further[141]. This negates the effect of the Thermal ECC media having a recording performance independent of T_c variations in storage layer (FePt). Decreasing the $M_{s,wl}$ and increasing the $K_{u,wl}$ similarly, leads to an increase in the write temperature which defeats the primary objective of low temperature writing that is the objective to be attained. With this trend, the optimized parameters for the write layer at 300K are identified as $M_{s,wl} = 700$ emu/cm^3 and $K_{u,wl} = 1 \times 10^7 erg/cm^3$. Table 2 lists the different thermal ECC media and their magnetic properties at 300 K.

Media	T_c (wl)	T_c (sl)	M_s (sl) at 300K	K_u (sl) at 300K
High Temperature Thermal ECC	900K	700K	922.3emu/cm^3	4.11×10^7erg/cm^3
Low Temperature Thermal ECC	600K	500K	856emu/cm^3	3.1×10^7erg/cm^3

Table 2. Magnetic properties of different Thermal ECC media[149]

6.2 Low temperature Thermal ECC media switching performance

To evaluate the switching probability distribution, a linear cooling process is implemented for the low temperature thermal ECC media. The media is cooled down from a peak temperature of 650K down to 300K at a constant cooling rate (CLR) of 200K/ns (dT/dx ~ 10K/nm & v ~ 20m/s). The direction of the head field is flipped at a certain switching time (or switching temperature). An error function is used to describe the switching probability curve mathematically[140]. The switching probability distribution is calculated by differentiating the probability curve and is Gaussian in nature. The switching performance is characterized by the FWHM of the SPD while the writing temperature is calculated at the point where the SPD curve attains a minimum. Smaller the FWHM of the SPD, better is the switching performance. Fig. 6.4 (a) shows the switching probability and SPD curve for the proposed low temperature thermal ECC structure. The write temperature T_{write} ~ 487K with a FWHM of the SPD = 51.4K. To further reduce this FWHM and ensure sharper switching, intergranular exchange coupling (IGC) (exchange coupling between grains) is introduced among grains in the

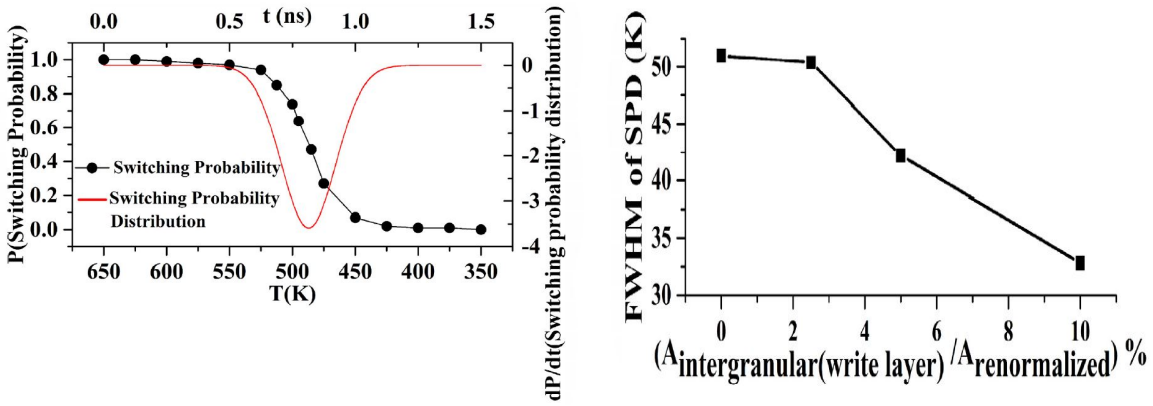

(a) (b)

Fig. 6.4 Switching performance for the low T_c Thermal ECC media (b) SPD FWHM variation with different exchange coupling values for grains in the write layer[149]

write layer to optimize the thermal ECC structure[142]. An interlayer exchange coupling equal to $\sqrt{A_{ex,wl} \times A_{ex,sl}}$ is used in all the simulations. The effect of variation in this value is considered in other works as well[150]. Fig. 6.4 (b) shows the variation in the FWHM of the SPD as the intergranular exchange coupling (write layer only) is increased.

Structure	$\delta T_{w,thermal}$	δT_w	$\delta T_{w,\delta Tc}$	SPD FWHM improvement
Low temperature Thermal ECC (Cooled from 650K)	25K	45.4K	38.4K	$\left(1-\frac{38.4}{48}\right)\times 100 = 20\%$
Single layer FePt (9nm) (Cooled from 850K)	40.4K	62.6K	48K	

Table 3. SPD FWHM values for different media and media variations[149]

The switching performance of the low temperature thermal ECC media is compared to the switching performance of a 9 nm single layer FePt structure ($T_c = 700K$) whose switching performance is calculated by a cooling process from 850K to 300K with a similar cooling rate. Table 3 shows the comparison of the switching performance. $\delta T_{w,thermal}$ represents the FWHM of the SPD in the absence of any media variations (σ_{Ku} and $\sigma_{Tc} = 0\%$), thus reflecting the effect of the superparamagnetic trap on the switching behavior. The low temperature thermal ECC media shows a definite improvement in the FWHM compared to the corresponding value for the single layer FePt structure. δT_w represents the FWHM of the SPD in the presence of a $\sigma_{Tc} = 3\%$ in both the write and storage layer. $\delta T_{w,\delta Tc}$ represents the increase in the FWHM due to the effect of T_c variation only; Eq. (6.1) relates the three FWHM values[150] assuming the effect of the superparamagnetic trap and T_c variation are independent effects.

$$\delta T_{w,\delta Tc} = \sqrt{\delta T_w^2 - \delta T_{w,thermal}^2} \tag{6.1}$$

The expected improvement[150] in the SPD is given by the expression $(1-T_{write}/T_c) \times 100\%$, which is $\sim$19% (for $T_{write} = 487$ K & $T_c = 600$ K). Intuitively, this improvement signifies the decrease in the writing temperature from the expected writing

temperature in HAMR (=T_c). This matches the improvement obtained via the switching simulations (=20%). Further, Fig. 6.5 shows the switching behavior for a 9 nm low temperature FePt structure with T_c = 500 K and cooled down from a peak temperature of 650 K down to 300 K (same as the proposed low temperature thermal ECC media structure). It is observed that at both high and low switching temperatures,

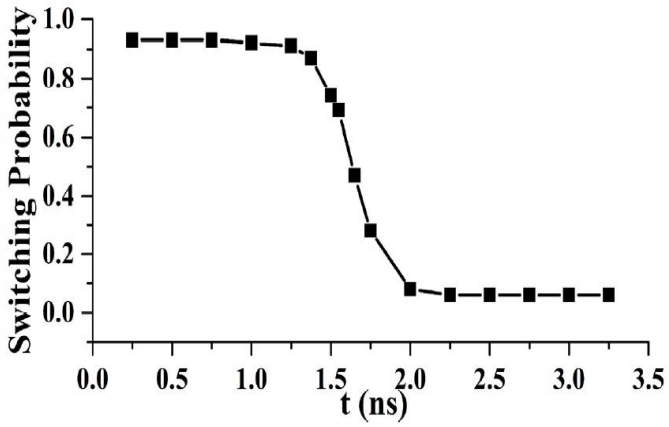

Fig. 6.5 Switching performance for single layer FePt media cooled from 650K with CLR = 200K/ns[149]

the switching probabilities fail to attain the maximum and minimum value of 1 and 0 respectively. This indicates the presence of significant thermal fluctuations in the low temperature FePt structure, thus helping conclude that the low temperature thermal ECC media shows a switching performance improvement greater than 20% when compared to a low temperature FePt structure. In addition to the switching performance, another performance parameter is the transition jitter. In general, the high temperature Thermal ECC media structure performs far better than the single layer FePt structure in terms of jitter values.

6.3 Low temperature Thermal ECC media recording performance

The recording performance of a HAMR media is evaluated in terms of the SNR and transition jitter (referred to as simply jitter) obtained for a set of written patterns. To evaluate the transition jitter, it is necessary to have a significant number of transitions to

account for better statistics. Thus, a single tone sequence is used instead of a PRBS to represent the written patterns. To ensure an easy capture of the written sequence and to easily distinguish each bit from the next one, a relatively large Bit Length (BL) = 20nm is used in the writing process.

Fig. 6.6 (a) shows the jitter performance and Fig. 6.6 (b) shows the SNR for a transition pattern written in the presence of a heat spot with different FWHM values. In each case, the readback width (RW) for the read head is maintained to be half of the FWHM. Introducing intergranular exchange coupling helps combat the DC noise. Based on the jitter variation, we can see a relatively flat dependence on intergranular exchange with a

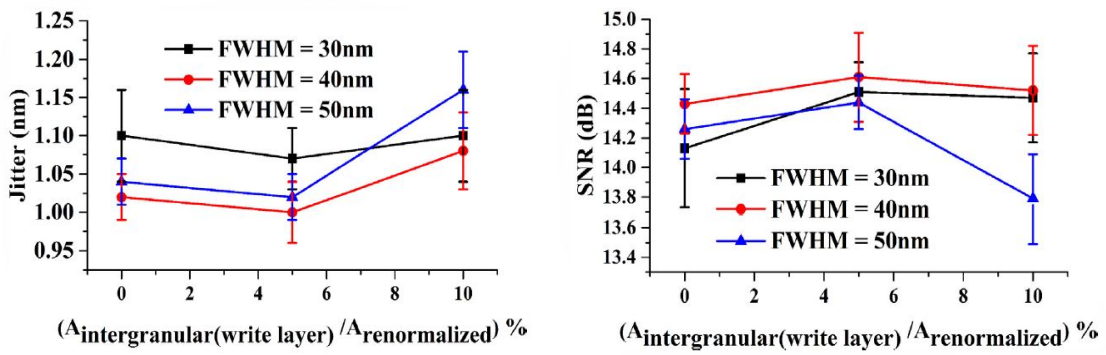

(a) (b)

Fig. 6.6 Recording performance of the low T_c ECC media for different heat spot FWHM (a) Jitter (b) SNR [149]

minimum jitter value at an intergranular exchange coupling value of 5% of the renormalized value for each FWHM value. At this intergranular exchange coupling value, the FWHM of the SPD is 42.2K (from Fig. 6.4 (b)) with a T_{write} = 486K. The switching performance of the proposed low temperature thermal ECC media is thus found to be comparable to the performance of the high temperature thermal ECC media with the FWHM of the SPD = 44K[140].

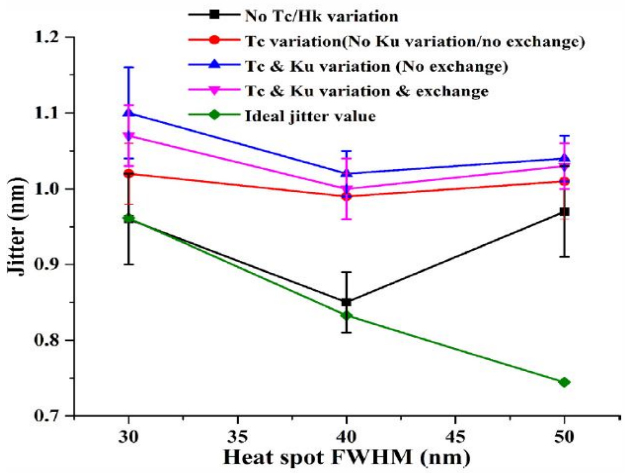

Fig. 6.7 Recording performance of the low temperature Thermal ECC media for different media variations [149]

The study of the recording behavior of the low temperature thermal ECC media under different media variations presents an interesting picture. Fig. 6.7 shows the recording performance of the low temperature Thermal ECC media under varying material properties. In the absence of any media variations, the jitter values for the heat spot FWHM of 30nm & 40nm, attained at a peak heat spot temperature Thermal ECC structure reaches a peak performance in spite of containing Voronoi grains with irregular shapes and variable grain diameters. In the presence of T_c and K_u variations, the jitter value shows an increase of about 0.2nm, which is quite small, compared to the effect these variations have on a single layer FePt media. Based on Fig. 2(b) of [141], adding a 3% T_c variation in a 9 nm single layer FePt media increases the jitter by ~0.17 nm which is further worsened as a 15% K_u variation is included in the simulation when the heat spot FWHM = 40nm. This is higher than the ~0.14nm jitter increase for the same heat spot dimension for the low temperature Thermal ECC media, based on Fig. 6.7. Introducing intergranular exchange coupling with an optimum 5% value seems to reduce the jitter to a point where the effect of K_u variation is almost eliminated.

To compare the performances of the low temperature Thermal ECC media with the previously proposed high temperature Thermal ECC media[140], similar micromagnetic simulations are implemented for the high temperature Thermal ECC media with $T_{c,wl} = 900K$ and $T_{c,sl} = 700K$. Optimum intergranular exchange coupling is introduced to

improve the performance of this structure. Fig. 6.8 shows the comparison of the recording performance of the high temperature thermal ECC media with the proposed low temperature thermal ECC media. At different heat spot FWHM's, the two structures seem to perform equally well. This indicates the practical nature of the low temperature thermal ECC media that writes at a lower write temperature (486K compared to 738K) in the presence of a heat spot at lowered peak temperature (650K as opposed to 850K).

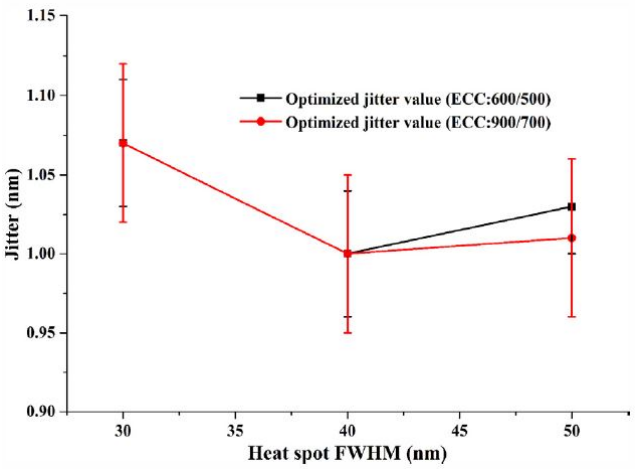

Fig. 6.8 Recording performance comparison of the previously proposed high T_c ECC media (red curve) and the newly proposed low T_c ECC media (black curve)[149]

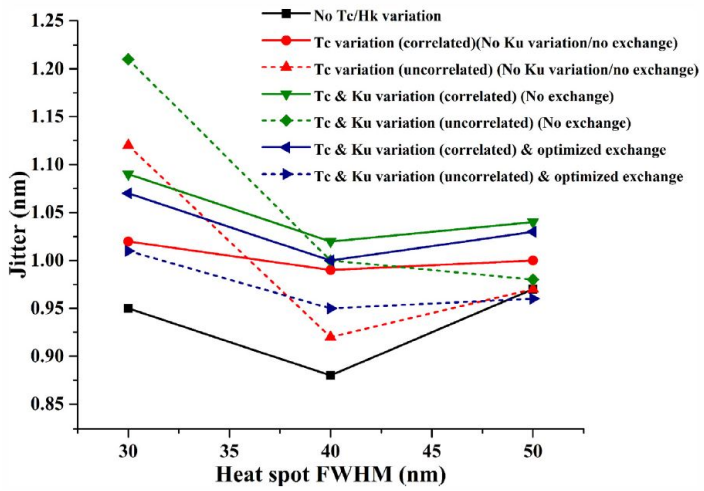

Fig. 6.9 Recording performance of the low T_c Thermal ECC media for correlated and uncorrelated media variations in the write and storage layer[149]

6.4 Recording performance with uncorrelated media variations

To further observe the effect of media variations, an uncorrelated T_c and K_u variation is introduced in the write and storage layer. Uncorrelated variations mean that T_c and K_u vary independently in the write and storage layer. The understanding behind this simulation set is that grains in the write and storage layer are fabricated independently; hence, the variation of temperature and anisotropy for the grains of the write and storage layer may be different. However, Fig. 6.9 shows that this thermal ECC media has a remarkably small variation in the recording performance when the effect of correlated and uncorrelated variation is compared. It implies that success of the media will depend little on the source of the variations.

6.5 Reduction of storage layer anisotropy

The low temperature Thermal ECC media design could be fabricated by doping the FePt media to reduce its T_c to 500K. However, this doping is a complex step and experimental variations during fabrication often leads to a difficulty in maintaining precise magnetic properties. This is particularly true when it comes to retaining high anisotropy values in the process of doping to reduce the T_c value. The research related to this aspect of the low temperature Thermal ECC media was performed in coordination with Dr. Warunee Tipcharoen. Reducing the T_c of FePt to 500K from 700K reduces the anisotropy from about $4.11 \times 10^7 erg/cm^3$ down to about $3 .1 \times 10^7 erg/cm^3$ at 300K. Fabrication issues, like an incomplete annealing process (required for fabricating the high anisotropy $L1_0$ phase of FePt) and variations in the DC sputtering process conditions can lead to a decrease in the anisotropy, a variation in the grain diameters, and intrinsic T_c variation in the media. In this section, an additional reduction in the storage layer (FePt) anisotropy to values around $2 \times 10^7 erg/cm^3$ at 300K is considered. The viability of a lowered storage layer anisotropy Thermal ECC structure is considered by studying the effect of applied field and field angle on the switching and recording performance. This investigation helps

define a lower limit for K_u values for the storage layer of the Thermal ECC media, as well as the lower limit for the corresponding writing temperature.

Micromagnetic simulations with the low temperature Thermal ECC media with reduced storage layer anisotropy yields an interesting tradeoff between the writing temperature and the switching performance (FWHM of SPD) as well as the writing temperature and recording performance (transition jitter) when the behavior of the media is plotted with respect to different applied field magnitudes[149]. These simulations also help establish a constant field of 8kOe as the optimum field for obtaining the best switching and recording performance for the low temperature Thermal ECC media with and without the lowering of the storage layer anisotropy. Evaluating the behavior of this low temperature Thermal ECC media with reduced storage layer anisotropy for different applied field angles and Grain Pitch values also helps conclude the following (i) the writing temperature decreases as the applied field angle increases, and the effect is far more pronounced for the lower storage layer anisotropy structures compared to the higher storage layer anisotropy structure (ii) in general, the larger grain pitch material has a larger writing temperature due to a higher energy barrier. This tradeoff clearly restricts any further cooling of this structure unless degrading the recording and switching performance is a worthwhile compromise.

6.6 Summary

This work was supported by Seagate and ASTC. The switching behavior of the low temperature Thermal ECC media structure indicates a write temperature lowering of about 34% with a FWHM of the SPD = 42.2 K indicating a comparable switching behavior to the ECC structure switched at higher temperatures. The recording performance of the optimized low temperature Thermal ECC structure is commensurate with the optimized performance for the high temperature Thermal ECC structure. This helps establish the validity of the low temperature Thermal ECC media structure as a substitute for the high temperature Thermal ECC media structure, thus eliminating the heating and consequent noise issues currently impeding the successful implementation of

HAMR. Lowering the storage layer anisotropy for the Thermal ECC structure affects the switching probability distribution slightly, adversely affects the jitter, and creates a higher switching and recording performance dependence on the applied field and angle. The commercial release of HAMR is an urgent necessity for the data storage industry to ensure that the HDD maintains its position as the primary mode of data storage. In this context, the proposal of a low temperature Thermal ECC media is a positive step forward. Although further analysis for this media in terms of performance for multitrack writing and writing in the presence of realistic thermal gradients is necessary, the single-track performance for the media indicates that it would be a worthy investment to find techniques to fabricate such a media.

Chapter 7

Analytical formulation for estimation of transition jitter for HAMR

In the HAMR process, the transition jitter describes the variation in the locations at which transitions occur on the media. This is an important representation of the efficiency of the recording process. This makes the accurate calculation of transition jitter an extremely important post processing component of the HAMR process once data has been encoded, detected and readback. In the HAMR system, different factors can contribute to the eventual jitter value. To understand the total noise in the recording process, micromagnetic simulations are implemented that involve writing specific patterns (preferably patterns with high number of transitions thus ensuring enough sampling to calculate the jitter value), readback of the written patterns and observing the locations at which transitions occur in these patterns. The process to implement these micromagnetic simulations has been described before in Chapter 3. These simulations are quite time consuming to implement, especially when the media size is large. On average, considering good sampling size and accurate jitter values with low error bars requires ~300ns. This issue becomes worse if multitrack writing is involved. Additionally, these calculations also involve a contribution due to thermal fluctuations. The magnitude of the thermal field contributing to the jitter depends on a random number generator and thus may vary depending on different electronic systems and algorithms used in the random number generation. Thus, the jitter in the micromagnetic simulations contains a small component that depends on the system used to implement the simulations. Furthermore, jitter calculation also includes the effect of the demagnetization field, which makes the computational process complex, slow and often necessitates the use of parallel computing units like GPU's for faster calculations. In other words, to ensure a uniformity in the jitter values independent of the system used, jitter needs to be calculated by an alternate

technique that is fast, less complex than the code blocks for micromagnetic simulations, and independent of the systems used to implement the simulations.

In the PMR system, jitter depends on different factors like the grain size[151][152], size distribution[151], coercivity[153], thermal fluctuations and so on. For the PMR system, an analytical formulation can be used to calculate the jitter as given below

$$\sigma_{\text{jitter}} = \sqrt{\frac{(<D>+GB)}{RW}\left(\left(\frac{\delta H_c}{\frac{dH_c}{dx}}\right)^2 + \frac{(<D>+GB)^2}{(12)} \times \beta\right)} \tag{7.1}$$

In this formula, β is a function of the Grain Size Distribution, GB denotes the non-magnetic grain boundary width, RW is the Read Width. H_c is the coercivity field for which the expression is given as

$$H_c(T) = H_k\left(1 - \left[\frac{k_B T}{K_u V}\ln(At)\right]\right)^n \tag{7.2}$$

H_k is a function of Curie temperature T_c and thus the jitter in PMR would depend on σ_{Tc} and σ_{Hk} .

In the HAMR process, there is a complete lack of any such analytical formulation that can help calculate the jitter value. While there have been efforts to relate the effect of individual factors like media variations[154] and thermal fluctuations[155] to the jitter value, these expressions do not establish the analytical effect of individual factors on the jitter value and lead to complicated expressions for calculating jitter. In this chapter, an analytical formulation to estimate jitter in the HAMR process is derived that can act as a cross check for the values obtained from the micromagnetic simulations. The derivation is designed to be simple, easy and extremely fast to use and takes into account the effect of different factors specific to the HAMR process on the eventual jitter value.

7.1 Dependence of jitter on different factors

Similar to the PMR process, it is necessary to identify factors specific to the HAMR process which would affect the jitter value. This would help derive the analytical

formulation by modeling the effect of these individual factors and combining these effects the get the final jitter value. The first factor to affect the jitter value is the Grain Size (D). In the micromagnetic simulations, the Voronoi media generated to represent the HAMR media consists of grains with an average Grain Size (D), a non-magnetic grain boundary = 1nm and a finite Grain Size Distribution (GSD) = δD/D which is normally around 20% (δD refers to the grain size variation). Since the magnetic grains and non-magnetic grain boundaries both contribute to the jitter value, their combined effect is considered by calculating the Grain pitch (GP) defined as the average Grain Diameter (D) + non-magnetic grain boundary (1nm). It can also be understood as the average center to center distance between two grains surrounded by a non-magnetic grain boundary.

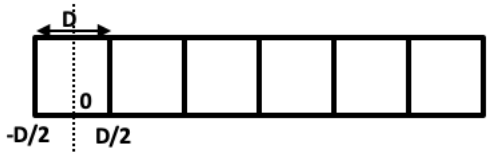

Fig. 7.1 Schematic of a microtrack with grains of equally sized diameter D[156]

Fig. 7.1 shows the illustration of a microtrack that is useful to understand the effect of Grain Pitch on the jitter value. Each grain is identical with a grain diameter = D. Since the grains are identical, the transition center (location of the transition) is uniformly distributed within a length = GP. Thus, the corresponding probability distribution function (PDF) f(x) for the transition location can be written as

$$f(x) = \frac{1}{GP} \tag{7.3}$$

Considering the definition of variance with a pdf f(x), for the pdf in equation (7.3)

$$\mathrm{Var}\big(f(x)\big) = \int_0^{GP} x^2 \times f(x)dx - \int_0^{GP} (x \times f(x))^2 dx \tag{7.4}$$

$$\mathrm{Var}\left(\frac{1}{GP}\right) = \int_0^{GP} x^2 \times \frac{1}{GP} dx - \int_0^{GP} (x \times \frac{1}{GP})^2 dx \tag{7.5}$$

Working out the integral in equation (7.5) yields the jitter in the downtrack (DT) direction due to the finite GP

$$\sigma^2_{jit,GP,DT} = \frac{GP^2}{12} \tag{7.6}$$

Considering the effect of readback in the crosstrack (CT) direction, the number of microtracks contributing to the jitter value depends on the width of the reader (RW) and the grain pitch (GP). Considering this factor and averaging over the number of microtracks in the CT direction (N), the total jitter due to the finite grain pitch is

$$\sigma^2_{jit,GP} = \left(\frac{1}{N}\right) \times \frac{GP^2}{12} = \left(\frac{GP}{RW}\right) \times \frac{GP^2}{12} = \frac{GP^3}{(RW \times 12)} \tag{7.7}$$

This jitter formulation matches the jitter value obtained in [151].

The next effect specific to the HAMR process is that of the heat spot. An ideal heat spot with an infinite thermal gradient (FWHM~0) would ensure a sharp transition with no additional jitter. Thus, it would appear that higher the thermal gradient, lower is the noise in the recording process. However, a high thermal gradient (dT/dx) also indicates lesser time for the grains to cool down (dT/dt) thus causing grains to retain an incorrect magnetization configuration and increasing the DC noise. Thus, it is necessary to take into account, the effect of both the thermal gradient of the heat spot (dT/dx) and the cooling rate for the grains (dT/dt). The finite thermal gradient and heat spot FWHM value, lead to a positional gradient in the SP. To find this gradient, the chain rule is used to relate the switching probability SP [P(T)] as a function of position to the switching probability distribution (SPD) where dP(T)/dT denotes the SPD and where dT/dx is the gradient at write temperature.

$$\frac{dP(T,x)}{dx} = \frac{\partial P}{\partial T} \times \frac{\partial T}{\partial x} \tag{7.8}$$

Since the SPD calculation already takes into account the effect of other recording factors, such as cooling rate and thermal fluctuations, no separate equations need to be derived to relate these factors to the jitter value. This calculation can also account for variations of intrinsic magnetic parameters, thus reducing the overall complexity in calculating the noise in the HAMR process. This calculation is faster (~1ns), does not involve the calculation of magnetostatic interactions, and is largely system independent. This

simplifies the proposed analytical formulation. Since the SPD is Gaussian in nature[140] and the thermal gradient at the writing temperature is constant, the positional gradient is Gaussian. Using the chain rule and normalizing the jitter in the CT direction yield the jitter due to the heat spot geometry. The equation for the jitter in the DT direction is given below. $\sigma_{dP/dT}$ denotes the standard deviation of the SPD

$$\sigma_{dP/dx,DT} = \frac{\sigma_{dP/dT}}{\frac{dT}{dx}} \tag{7.9}$$

Considering the effect of the reader in the CT direction and the averaging effect of N microtracks, the jitter due to the thermal gradient is

$$\sigma_{dP/dx} = \frac{1}{\sqrt{N}} \times \left(\frac{\sigma_{dP/dT}}{\frac{dT}{dx}} \right) = \sqrt{\frac{GP}{RW}} \times \left(\frac{\sigma_{dP/dT}}{\frac{dT}{dx}} \right) \tag{7.10}$$

Since the HAMR medium consists of Voronoi grains with varying GP, the final jitter value experiences an additional jitter due to the nonuniformity of the Voronoi grains. This nonuniformity is expressed by the GSD (=δD/D). The effect of GSD on the jitter due to the heat spot thermal gradient has already been considered when the SPD calculations are implemented for the Voronoi media. The effect of the GSD on the jitter due to the GP needs to be considered. Mathematically a Taylor expansion for the GP in equation (7.7) is considered

$$\sigma_{jit}^2 = \sigma_{jit,GP}^2 + \frac{D^3}{(RW \times 12)} \times \left[\left(\frac{\delta D}{D} \right)^3 + 3 \times \left(\frac{\delta D}{D} \right)^2 + \left(\frac{\delta D}{D} \right) \right] \tag{7.11}$$

Since δD can be both positive and negative, to account for the effect of GSD on jitter, the average of δD over all possible values is computed for the three different terms in equation (7.11)

$$< \left(\frac{\delta D}{D}\right)^3 > = \frac{1}{D^3} \left(\frac{\int_{-\infty}^{\infty} (D - D_{avg})^3 e^{-\left(\frac{1}{2}\left(\frac{D - D_{avg}}{\delta D}\right)^2\right)} dD}{\int_{-\infty}^{\infty} e^{-\left(\frac{1}{2}\left(\frac{D - D_{avg}}{\delta D}\right)^2\right)} dD} \right) = 0 \tag{7.12}$$

$$< (\frac{\delta D}{D})^2 > = \frac{1}{D^3}\left(\frac{\int_{-\infty}^{\infty} (D-D_{avg})^2 e^{-\left(\frac{1}{2}\left(\frac{D-D_{avg}}{\delta D}\right)^2\right)} dD}{\int_{-\infty}^{\infty} e^{-\left(\frac{1}{2}\left(\frac{D-D_{avg}}{\delta D}\right)^2\right)} dD} \right) = 3(\frac{\delta D}{D})^2 \quad (7.13)$$

$$< (\frac{\delta D}{D})^1 > = \frac{1}{D^3}\left(\frac{\int_{-\infty}^{\infty} (D-D_{avg}) e^{-\left(\frac{1}{2}\left(\frac{D-D_{avg}}{\delta D}\right)^2\right)} dD}{\int_{-\infty}^{\infty} e^{-\left(\frac{1}{2}\left(\frac{D-D_{avg}}{\delta D}\right)^2\right)} dD} \right) = 0 \quad (7.14)$$

Based on the integrals in equation (7.12) – (7.14), the additional jitter due to the GSD can be written as

$$\sigma^2_{jit,\delta D} = \frac{GP^3}{(RW \times 12)} \times \left[3 \times \left(\frac{\delta D}{D}\right)^2\right] \quad (7.15)$$

Here (δD/D) denotes the GSD. The total jitter due to the analytical formulation can now be written as

$$\sigma^2_{jit,theory} = \sigma^2_{jit,GP} + \sigma^2_{jit,dP/dx} + \sigma^2_{jit,\delta D} \quad (7.16)$$

7.2 Comparison with micromagnetic simulations

The analytical formulation provides a cross check to the jitter values generated by the micromagnetic simulations. Equation (7.16) and the explanation that followed to derive the analytical equation described the simple and versatile nature of the formulation. To verify the correctness of the analytical formulation, it is necessary to compare the results obtained from the formulation to the results obtained by implementing micromagnetic simulations.

The micromagnetic simulations estimate jitter (σ) for the single-layer FePt media (384nm downtrack (DT) × 48nm crosstrack (CT) × 9nm thickness) on which a single-tone sequence is written. The media consist of Voronoi grains, and a 1nm nonmagnetic grain boundary is used around the grains. The Bit Length used in the simulation is 21nm, and the head velocity is 20m/s. A Gaussian heat spot with DT and CT Full-Width at Half-

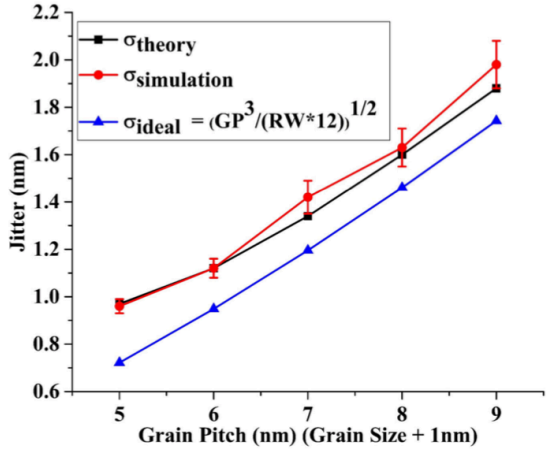

Fig. 7.2 Jitter comparison (σ_{theory} and $\sigma_{simulation}$) for different GP (T_{peak} =850K, Heat spot FWHM = 40nm, RW=20nm)[156]

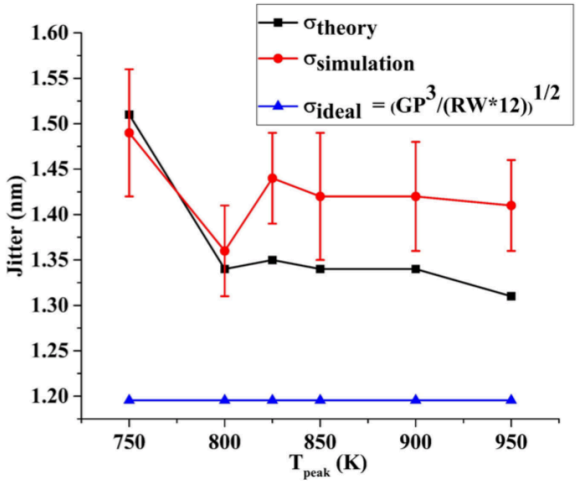

Fig. 7.3 Jitter comparison (σ_{theory} and $\sigma_{simulation}$) for different T_{peak} (GP=7nm, RW=20nm) [156]

Maximum (FWHM) of 40nm, and peak temperature of 850K was used to heat the media. Readback is implemented with a shield-to-shield spacing of 21nm and a read width (RW) of 20nm. For the switching probability (SP) calculations, the medium is cooled down with a constant cooling rate (CLR) from a peak temperature (T_{peak}) down to room temperature (300K), and at a certain temperature, the direction of the uniform applied field (Happl = 8kOe) is reversed. Differentiating this SP curve yields the SP distribution (SPD).

The comparisons are implemented for jitter calculated from two sources: The analytical formulation or equation (7.16) (denoted as σ_{theory}) and micromagnetic simulations (denoted as $\sigma_{simulation}$). For the simulations, jitter is calculated considering at least 200

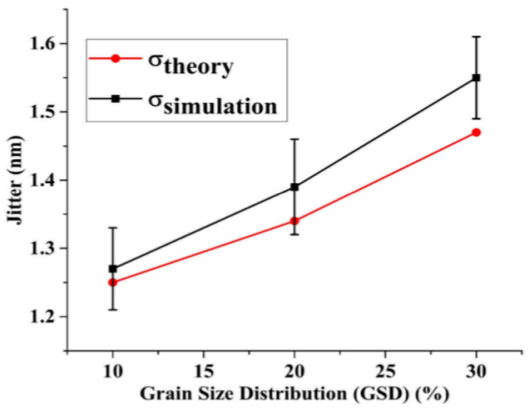

(a)

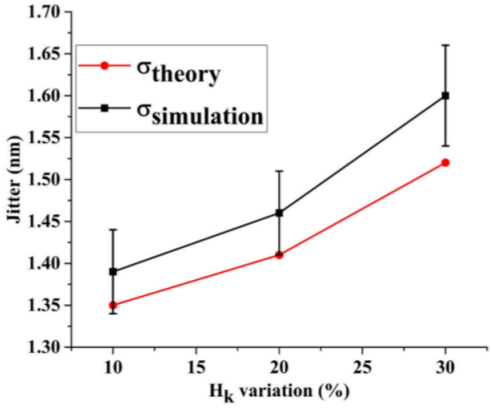

(b)

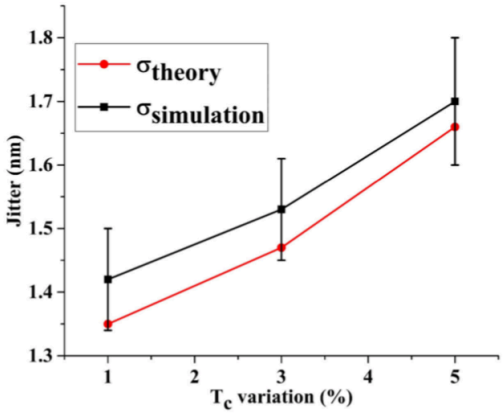

(c)

Fig. 7.4 (a) - (c) Jitter comparison (σ_{theory} and $\sigma_{simulation}$) for different media variations (GP=7nm, RW=20nm) [156]

zero crossings. Fig. 7.2 shows a comparison of jitter values calculated for different GP values with GSD = 20%. σ_{ideal} denotes the jitter value for a Gaussian heat spot with an infinite thermal gradient which is used to write patterns on a HAMR media with uniform grains and no GSD. This corresponds to equation (7.7). For the SP simulations, the cooling rate CLR = (dT/dx) (at writing temperature) × dx/dt (head velocity) = 390 K/ns (dT/dx ~19.5 K/nm and dx/dt = 20 m/s). In Fig. 7.2, the close agreement of the jitter

values obtained from the two different techniques helps define the accuracy of the analytical equations.

The next comparison is implemented for different values of the heat spot gradient. To do so, simulations are implemented for a media with average GP = 7 nm and different T_{peak} (peak temperature of heat spot). To maintain the same width of the write spot, the FWHM and the corresponding CLR value is varied. Fig. 7.3 shows a comparison of the jitter obtained with the analytical formulation and the simulations. Once again, the values are comparable to each other, showing the accuracy of the derived analytical equations.

An important source of noise in the HAMR process is the variations in the magnetic and granular properties of grains. The effect of variation in magnetic parameters due to the granular T_c variation has been studied before[113]. These media variations arise due to improper fabrication processes and a variation in the shape and size of the grains. Jitter values calculated using micromagnetic simulations are compared to the analytical estimate for different GSD, σ_{Tc} and σ_{Hk}. Fig. 7.4 (a) - (c) show the comparison of jitter calculated from the analytical formulation and the micromagnetic simulations for different extents of media variations. The analytical formulation predicts jitter values close to the values provided by the micromagnetic simulations. The analytical formulation assumes the jitter due to GP ($\sigma_{jit,GP}$) and heat spot thermal gradient ($\sigma_{jit,dP/dx}$) to be independent. In reality though, they are not completely independent and exhibit a minor correlation. Correlations in grain position can also affect the jitter[157]. This can explain the small discrepancy between the jitter values obtained from the two sources in Figs. 7.2, 7.3 and 7.4 (a) – (c).

7.3 Effect of read head misalignment

In the HAMR process, a constant field and field gradient are applied in the CT direction. In this direction, the transitions are often curved in nature due to the Gaussian nature of the heat spot. As the heat spot FWHM decreases, the curvature of the transitions increases, and the curvature radius decreases. The effect of the transition curvature worsens as the Read Width (RW) in the CT direction increases since the curved transition

is not read back properly. Some solutions have been proposed for this issue including changes to the head design and using multiple readers and oversampling in the CT direction[158]. However, the misalignment of the reader with respect to the written track center creates additional issues in the calculation of the jitter.

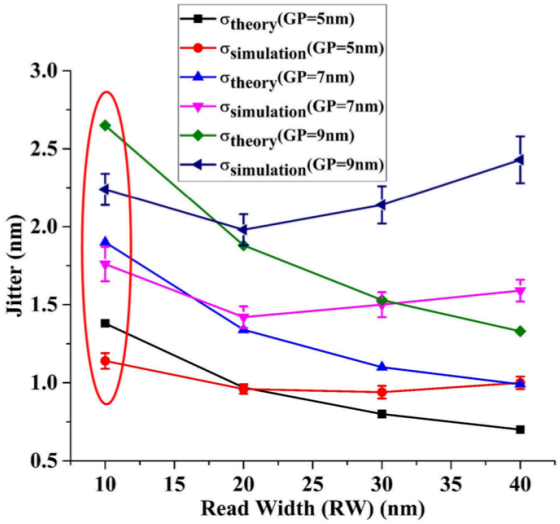

Fig. 7.5 Jitter comparison (σ_{theory} and $\sigma_{simulation}$) for different GP and RW values (Ellipse indicates discrepancy of interest which is investigated further)[156]

Fig. 7.5 shows the effect on jitter as RW varies from 10nm to 40nm for different GP values. The ideal RW value (RW_{ideal}) is about half the heat spot FWHM where the written transition is read back perfectly. RW_{ideal} ~20nm when the heat spot FWHM equals 40 nm and T_{peak} = 850K. For RW > RW_{ideal}, the linear reader detects additional noise due to curved transitions that is not reflected in the analytical estimate, which assumes a straight transition. Hence, $\sigma_{simulation} > \sigma_{theory}$. The detection of extra noise due to the curved nature of the transition in the HAMR process has been studied in detail previously[118]. The case for small RW (< RW_{ideal}) is interesting. From Fig. 7.4, for RW = 10nm, the analytical formulation predicts a jitter value greater than the actual value for different GP values. This is unexpected for small RW, where the curved nature of the transition has little effect on the detected noise. For this RW (~GP), the discrepancy can be explained by understanding the nonlinear behavior of the playback for small RW.

Fig. 7.6 shows the shape of the potential curve assumed in the analytical formulation. The analytical formulation assumed the square potential to be perfectly aligned with respect to

the microtracks. In reality though, the head potential is frequently misaligned, as shown in Fig. 7.6. To understand the corresponding jitter calculation, the calculation of signal power (SP_{sq}) and noise power (NP_{sq}) due to the misaligned potential curve is considered.

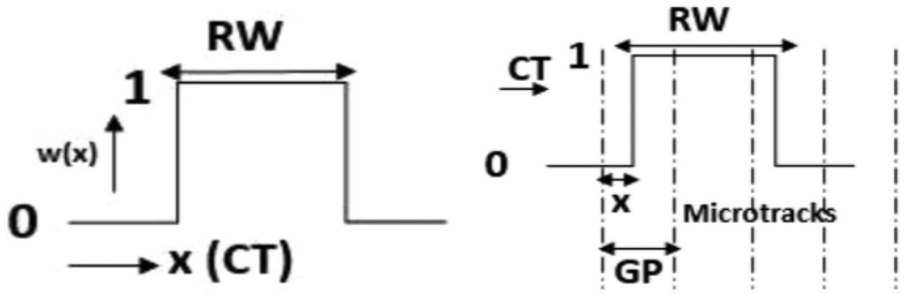

Fig. 7.6 Assumed square pulse potential for the analytical formulation[156]

For a microtrack length equal to GP, the RW can be defined as RW = N × GP + F. Thus, for the square pulse, the Signal Power (SP) and Noise Power (NP) are, respectively, given by equation (7.17) and (7.18) where n_{DT}^2 represents the normalized NP in the CT direction.

$$SP_{sq} = \frac{1}{GP} \times [\ (\int_0^{GP-F}\big((GP - x) + (N-1)GP + (F + x)\big)^2 dx + (\ \int_{GP-F}^{GP}((GP - x) + (N)GP + (F + x - GP))^2 dx)] \quad (7.17)$$

$$NP_{sq} = n_{DT}^2 \times [\frac{1}{GP} \times \left(\int_0^{GP-F}((GP - x)^2 + (F + x)^2 dx)\right) + \frac{GP-F}{GP} \times (N-1)GP^2 + \frac{1}{GP} \times \left(\int_{GP-F}^{GP}((GP - x)^2 + (F + x - GP)^2 dx)\right) + \frac{F}{GP} \times (N)GP^2\ ] \quad (7.18)$$

The SP_{sq} is the total area under the potential curve. The SP_{sq} and NP_{sq} can be simplified to

$$SP_{sq} = (RW)^2 \quad (7.19)$$

$$NP_{sq} = n_{DT}^2 \times GP \times RW \times (1 - \frac{GP}{3RW}) \quad (7.20)$$

Equation (7.20) matches the noise power due to the square potential as referenced in [159]. The squared jitter value given by the ratio of the value in equation (7.20) to the value in equation (7.19)

$$\sigma^2_{\text{theory,nonlin}} = n^2_{DT} \times \frac{GP}{RW} \times \left(1 - \frac{GP}{3RW}\right) \quad (7.21)$$

Considering the effect of GSD in equation (7.21), the final squared jitter value taking into account the effect of read head misalignment is

$$\sigma^2_{\text{theory,nonlin,tot}} = n^2_{DT} \times \frac{GP}{RW} \times \left(1 - \frac{GP}{3RW}\right) + \frac{GP^3}{(RW \times 12)} \times 3 \times \left(\frac{\delta D}{D}\right)^2 \times \left(1 - \frac{2GP}{3RW}\right) \quad (7.22)$$

Since equation (7.22) shows the CT squared jitter (σ^2) effect to be proportional to $(GP/RW)^2$, we can conclude the reader displays a nonlinear readback response instead of the assumed linear response. Table 4 shows the correction for the analytically calculated jitter and the successful comparison of the jitter value for RW = 10nm.

GP (nm)	σ_{theory} (nm)	$\sigma_{\text{theory,nonlin,tot}}$ (nm)	$\sigma_{\text{simulation}}$ (nm) (From Fig. 7.5)
5	1.38	1.24	1.14 ± 0.04
6	1.55	1.37	1.32 ± 0.06
7	1.9	1.66	1.76 ± 0.11
8	2.25	1.88	1.9 ± 0.1
9	2.65	2.18	2.24 ± 0.1

Table 4. Corrected jitter values for RW=10nm and different GP[156]

7.4 Summary

This work was supported by ASTC. The analytical formulation for jitter derived in this chapter is a useful tool for quick calculation of jitter for different HAMR media. Its generalized nature and ability to factor in the effects of various causes of jitter makes this a complete formulation. This impact of different physical factors has been included without making any simplified assumptions or without excluding any significant effects. Since the transition jitter has usually been estimated using simulations and rarely

calculated using analytical equations, these derivations provide a unique outlook toward understanding the causes of jitter. It is observed that these analytical calculations work well for estimating the jitter when comparisons are made to simulation results under different recording conditions and media variations. This theory should produce significant saving of computational time and resources for those developing recording media and systems. Additionally, it provides a cross-check for verifying the accuracy of jitter predictions obtained via other techniques, such as micromagnetic simulations.

Chapter 8

Analysis of ATE in the HAMR media

An important objective of the HAMR process is to offer improved storage densities for new HDD designs. Chapter 2 described in detail, the HDD system and in particular, the structure of the magnetic surface used to store data. This data is stored on the disk drive surface on consecutive tracks which are circular in shape. The size of these disk surfaces has decreased over a period of time, leading to smaller tracks and multiple disks stacked on one another in the form of a platter. However, mechanical and structural limitations have ensured that to attain the best possible storage densities, each disk surface should have multiple tracks. To record the maximum amount of data on each surface, the writing process stores information on multiple tracks that partially overlap each other thus improving the track density.

In the HAMR process, different factors involved in the recording process have different effects on the integrity of the written data. A sharp Gaussian heat spot with low FWHM would lead to minimum temperature spread and a high thermal gradient at the writing temperature. However, a high gradient indicates a small recording time window which may lead to incomplete freezing of the grains that would lead to the incorrect magnetization configuration. Thus, it is necessary to implement the recording process with an optimum FWHM. The other important factor is the field magnitude and direction used in the recording process. While a low field magnitude would lead to an inability for grains to switch the magnetization in the desired direction, a field magnitude higher than the optimum value would lead to a transition broadening after write where grains that are already written change their configuration due to the presence of a high magnitude field[160]. Another important factor affecting the efficacy of the recorded data is the grain size variation and the corresponding granular T_c variation. These variations affect the magnetic properties of individual grains of the media including the coercivity. Each

grain has a different anisotropy which needs to be overcome to switch the grain magnetization.

These issues are more consequential when multiple tracks partially overlapping each other are written in the HAMR process. In this writing process, when a track is being written, there is a finite tendency to erase the adjacent partially overlapping track/s which already have the data recorded on them. This phenomenon is called Adjacent Track Erasure (ATE) and it significantly reduces the achievable Areal Densities (AD) and restricts the CT writing process. ATE is especially critical in the HAMR process which also involves heating the media to reduce its coercivity. It is necessary to ensure that in the heating process, the lateral heat conduction is significantly lower than the axial (vertical) heat conduction for obtaining the desired recording pattern[161]. The ATE effect in the HAMR process is a consequence of a poor thermal gradient in the CT direction, variation in magnetic properties of the recording media as well as the track spacing. To obtain the expected AD improvements with the HAMR process, it is necessary to establish the presence and the numerical extent of ATE for different HAMR media. Once the understanding behind the presence of ATE in different HAMR media is established, efforts can be undertaken to reduce the ATE and make the media more resistant to this effect. Three different HAMR media are addressed to examine the presence and extent of ATE. These media are the conventional single layer FePt media, the high temperature (or high T_c) Thermal ECC media and the low temperature (or low T_c) Thermal ECC media. At different points in the thesis, these media and their magnetic properties have been introduced in detail.

8.1 Simulation Setup to study ATE

The simulation setup focuses on different parameters used to implement the micromagnetic simulations. The limitations in terms of available computational resources and simulation time is an important factor while implementing the ATE simulations, since they involve repeated writing of multiple tracks. Thus, knowledge from previously published literature is used to set the basis for some of the factors used to implement the

ATE related simulations. In the HAMR process, the ATE effect is present primarily in tracks that are immediately adjacent to the track being overwritten[162]. This allows the implementation of simulations to study the ATE by writing two tracks where one track is overwritten, and the effect of this overwriting is observed on the adjacent partially overlapping track. To establish the positions of the two tracks, an illustration of the HAMR multitrack writing process used to improve the AD values in [141] is used as reference. As the adjacent tracks start overlapping each other to a greater extent, the current pattern being written starts affecting the patterns previously being written, leading to an increase in the Bit Error rate (BER). However, to a limited extent, reducing the track spacing up to about 70% of the heat spot FWHM keeps the BER constant and the reduced spacing leads to an improved AD[141]. Below this spacing, the BER increases leading to a sudden drop in the AD values. Thus, for the HAMR process, in the presence of a noise free reader, the optimum track spacing is 70% of the heat spot FWHM[141]. The heat spot FWHM is kept at a minimum reasonable value equal to 30nm, leading to a track spacing of 21nm between Track 1 and Track 2. The positioning of these tracks is shown in Fig. 8.1.

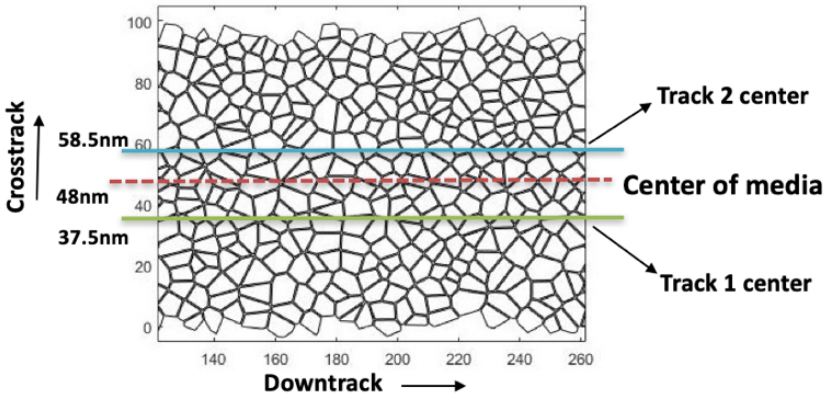

Fig. 8.1 Track positioning for Track 1 and Track 2. The tracks are positioned on either side of the media center and are equidistant from the center. The track spacing (21nm) is 70% of the Heat spot FWHM (30nm)

Micromagnetic simulations are implemented in order to establish the presence and numerical extent of ATE in different HAMR media. The downtrack (DT) and crosstrack (CT) dimensions of the media are maintained at 384nm and 96nm respectively. The media is overlaid with a renormalized cell system where each cell has a dimension of 1.5nm×1.5nm×1.5nm. The renormalization parameters for these cells are calculated from [108] and [113]. The thickness of the media varies depending on the media under analysis. For the single layer FePt media, three different thicknesses: 6nm, 7.5nm and 9nm are analyzed. For the Thermal ECC media (both the low and high temperature models), a lower thickness would mean higher susceptibility to thermal fluctuations and possibly the ATE effect. Hence the thickness for the Thermal ECC media for the write and storage layer is 3nm and 6nm respectively. Previously, the issues with the fabrication of thicker media have been explored[149][51]. Thus, estimating the ATE extent in thinner Thermal ECC media also helps present a realistic picture of this issue in the ECC media, rather than a suppressed picture for the thicker Thermal ECC media which is naturally more stable and less susceptible to ATE. An average grain size of 6nm and Grain Pitch of 7nm is used for generating the grains of the Voronoi media. To ensure the patterns can be easily used to calculate the SNR, the Bit Length (BL) used is 20nm. The head velocity is 20m/s which indicates a bit is written every 1ns. Finally, to account for the variation of the magnetic properties and renormalization parameters due to fabrication processes, a 3% T_c and 15% H_k variation is included in all the layers in the HAMR media.

The recording process consists of two steps. A constant applied field of 10kOe with a field angle of 22º is used to write different patterns as described. In the first step, a single tone sequence (101010…) is written on Track 1 with BL=20nm. A large BL makes it easier to identify the transition and remanance noise in the written patterns. This is followed by writing a 16-bit Pseudo Random Bit Sequence (PRBS) with padding bits on the adjacent partially overlapping Track 2. Track 2 is then overwritten multiple times with the same PRBS (unless specified otherwise) and the effect of this overwriting on the single tone sequence written on Track 1 is observed. This effect helps establish the extent

of ATE in the HAMR media under consideration. The playback signals for the written patterns are obtained using the reciprocity principle and assume a noise free reader. The numerical extent of ATE is established by calculating the SNR of the single tone sequence written on Track 1 every time the adjacent Track 2 is overwritten.

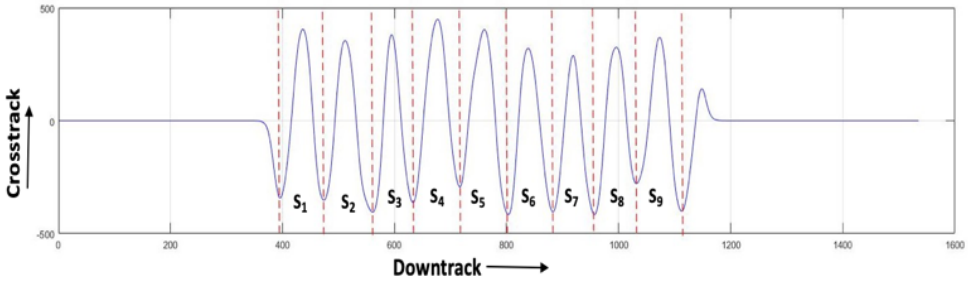

Fig. 8.2 SNR calculation for one playback signal. The results in the thesis sample signals from ten media (180 transitions) to calculate the SNR

Fig. 8.2 shows the process of calculating the SNR for the single tone sequence. Each sequence consisting of 18 transitions (excluding the boundary transitions) is divided into multiple signals each containing two transitions. Playback signals from ten HAMR media (or 180 transitions in total) with different individual Voronoi grains but similar average grain pitch and grain size distribution (20%) are combined to calculate the Signal to Noise Ratio (SNR). The equation for fitting the SNR of the Track 1 playback signal based on different overwrites of Track 2 is given as

$$\mathrm{SNR(dB)} = \mathrm{A} + \mathrm{B} \times \ln(\text{Write Number}) \tag{8.1}$$

where Write Number denotes the number of times Track 2 is written. For example, a Write Number = 1 indicates Track 1 is written once and Track 2 is written once. The value of parameter 'A' denotes the starting SNR (Write Number = 1) in the absence of overwrites of Track 2 whereas B denotes the extent of ATE. The higher the magnitude of B, the higher the SNR decrease for each overwrite and the higher the ATE effect. In the micromagnetic simulations implemented in this paper, the number of overwrites of Track 2 are restricted to 8 since it helps establish a trend in the SNR reduction while establishing an upper limit to the simulation time.

8.2 ATE presence in the HAMR media

As mentioned before, implementing micromagnetic simulations to study the presence and extent of ATE requires an investment of a significant amount of computational resources

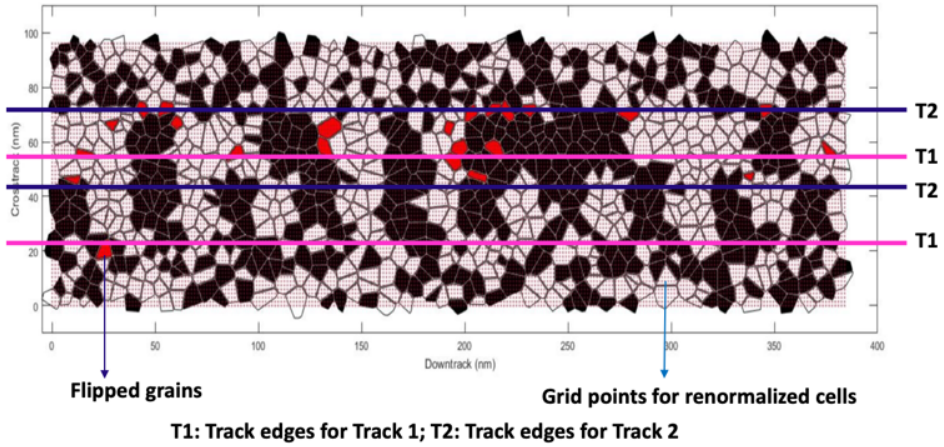

Fig. 8.3 Magnetization patterns on a Voronoi media overlaid with the dotted grid points for renormalized cells. The red grains denote grains whose magnetizations switch as Track 2 is overwritten once.

and time. Thus, before these simulations are implemented, it is necessary to establish the presence of ATE in the HAME media. The lack of a significant ATE presence would preclude the need for complex micromagnetic simulations that are computationally intensive. To establish the presence of ATE, the HAMR process is implemented for writing the single tone and PRBS sequences on the single layer FePt media. Fig. 8.3 shows the transition patterns as Track 1 and Track 2 are each written once followed by the overwriting of Track 2. The grains whose magnetizations switch in this process (change their color from black to white or vice versa) are marked in red. It is clear from Fig. 8.3 that a finite number of grains experience a change in their magnetization direction. Table 5 shows the number of grains whose magnetizations switch (flip) as Track 2 is overwritten multiple times with different track spacings between Track 1 & 2. As the track spacing decreases, this number increases, indicating the effect of decreasing track spacing. The fact that the number of grains whose magnetizations flip varies

Track2 write (Track 1 written once)	Bit Length=20nm Track spacing = 28nm	Bit Length=20nm Track spacing = 21nm
One-Two	3	13
Two-Three	4	8
Three-Four	0	12
Four-Five	3	10

Table 5. Number of grains whose magnetizations flip. One-Two denotes the magnetizations flipping when Track 2 is written once and then written again.

randomly even when the same PRBS is used for overwriting Track 2 indicates that deterministic overwriting cannot be the only contributing factor in this phenomenon. This observation helps visually establish the presence of ATE in the HAMR media before spending significant computational resources for its calculation.

8.3 Numerical extent of ATE in the HAMR media

The ATE in the single layer FePt media is calculated by implementing the writing process described previously Fig. 8.4 shows the variation in the SNR as Track 2 is overwritten multiple times. Although the error bars are not shown here (to avoid

Media	Thickness (nm)	RW = 15nm	RW = 20nm
Single Layer FePt	6	-0.30dB	-0.39dB
Single Layer FePt	7.5	-0.27dB	-0.40dB
Single Layer FePt	9	-0.08dB	-0.23dB
High T_c Thermal ECC	3 (Write Layer) 6 (Storage Layer)	-0.19dB	-0.25dB
Low T_c Thermal ECC	3 (Write Layer) 6 (Storage Layer)	-0.50dB	-0.46dB

Table 6. ATE in different HAMR media as measured by value of parameter B. The higher the magnitude of SNR decrease, the higher the ATE effect.

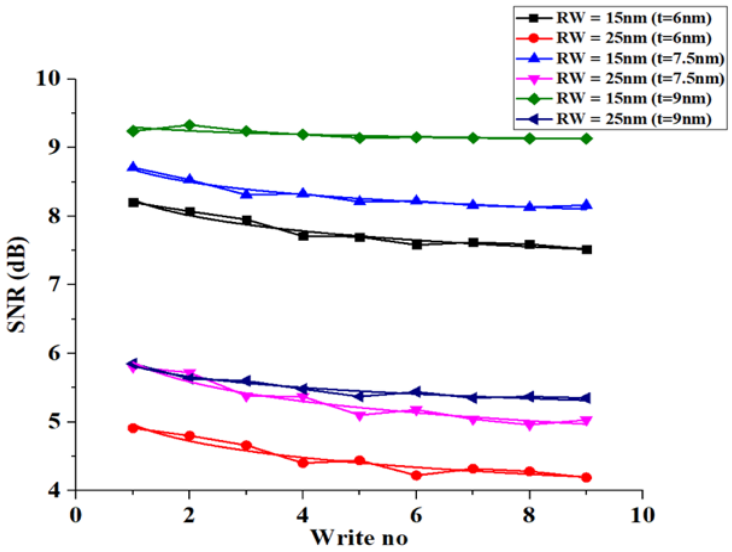

Fig. 8.4 SNR variation for different thicknesses for the single layer FePt media. Write No denotes the number of times Track 2 is written.

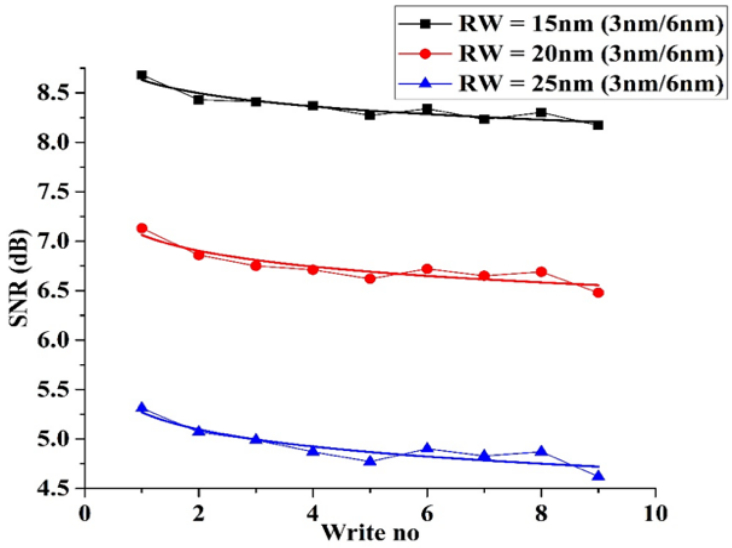

Fig. 8.5 SNR variation for different RW values for the high temperature Thermal ECC media.

congestion of data in the plot), the use of 180 transitions or ten HAMR media for sampling is enough to generate low error bars for the SNR. Similarly, the SNR observations for Read Width (RW) =20nm is not shown to avoid congestion in the plot.

The solid lines without the symbols indicate the fitting with equation (8.1) to find the fitting parameters A & B. Table 6 shows the value of parameter B or the numerical extent of ATE for different thicknesses of the single layer FePt media and for different RW values. It is clear that the FePt media becomes more susceptible to ATE as its thickness decreases. This can be traced to the decreasing thermal stability and the higher susceptibility of media with lower thicknesses to thermal fluctuations. These fluctuations affect the written patterns on the media causing higher transition noise for decreasing FePt thicknesses.

For the Thermal ECC media, the same writing technique as used for the single layer FePt media is used. Fig. 8.5 shows the SNR variation for the high temperature Thermal ECC media as Track 2 is written multiple times. Table 6 shows the numerical extent of ATE for the different Thermal ECC media analyzed in this chapter. It is easy to see that increasing the RW indicates a higher detection of noise in the playback process leading to a higher ATE. Comparing the values of ATE shows that the high temperature Thermal ECC media is more susceptible to the ATE effect than the single layer FePt media of equivalent thickness (9nm). This apparently matches the observations made by groups within the industry who have verified that the Thermal ECC media is more susceptible to ATE than the single layer FePt media. However, it is also interesting to see that the high temperature Thermal ECC media has a lower ATE than the single layer FePt media with lower equivalent thicknesses of 7.5nm and 6nm. This indicates that although only the write layer is involved in the writing process for the thermal ECC media, the stability contributed by the presence of the 6nm storage layer helps reduce the ATE.

For the low temperature Thermal ECC media, the T_c of the write layer is reduced from 900K (for the high temperature Thermal ECC media) to 600K and the storage layer T_c is reduced from 700K (for the high temperature Thermal ECC media) to 500K. In this process, the storage layer anisotropy reduces from 4.11×10^7erg/cm^3 to 3.1×10^7erg/cm^3 at 300K. This reduction makes the structure susceptible to thermal fluctuations. Although the use of optimization techniques and controlled variation of magnetic parameters can help the low temperature Thermal ECC media achieve comparable single-track writing

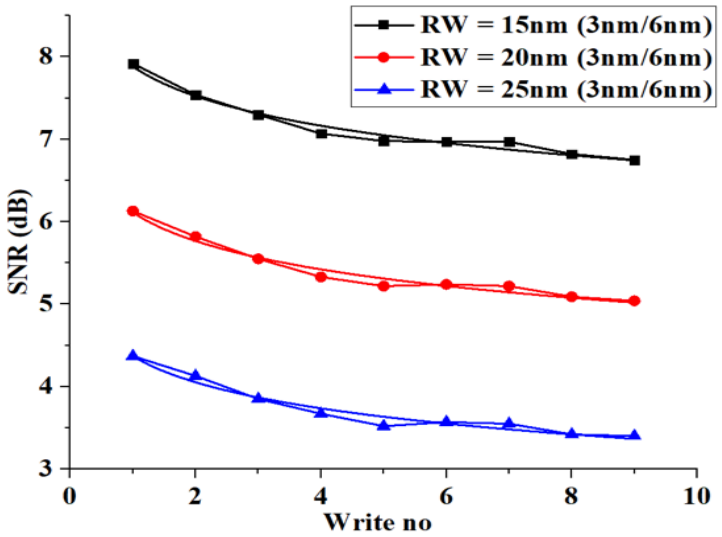

Fig. 8.6 SNR variation for different RW values for the low temperature Thermal ECC media.

performance as the high temperature Thermal ECC media[149], the reduced anisotropy (H_k) for individual grains makes the structure more susceptible to ATE. The reduction of the storage layer thickness to 6nm also reduces the thermal stability of this structure. Fig. 8.6 shows the SNR decrease for the low temperature Thermal ECC media.

As expected, Table 6 shows that the low temperature Thermal ECC media is significantly more susceptible to ATE than the high temperature Thermal ECC media. The high ATE susceptibility can be explained by understanding the issues with both the media and the NFT. In the context of this media, the reduced H_k for individual grains and the reduced thermal stability due to the low storage layer thickness contributes to the high ATE. With respect to the NFT, the peak temperature used to write on this media is 650K instead of 850K for the single layer FePt media and the high temperature Thermal ECC media. This leads to a reduced thermal gradient at the writing temperature (16.4K/nm instead of 25K/nm for the single layer FePt media) leading to a degradation of the written patterns. Both these issues contribute to the high ATE for this media.

In the HAMR process, another common phenomenon experienced by writing tracks closely spaced in the CT direction is the Adjacent Track Interference (ATI) effect[163]. This effect is experienced when the heat spot spreads laterally in the CT direction

affecting the temperature on different tracks and consequently the written patterns. This effect is the consequence of a poor heatsink layer and a low thermal gradient for the heat spot. Unlike the ATE effect which is a stochastic phenomenon leading to a significant SNR decrease, the ATI phenomena is repeatable. To understand the component of ATI effect in the multitrack writing process implemented in this paper, we implement a similar writing process as described before but alter the PRBS used to write on Track 2.

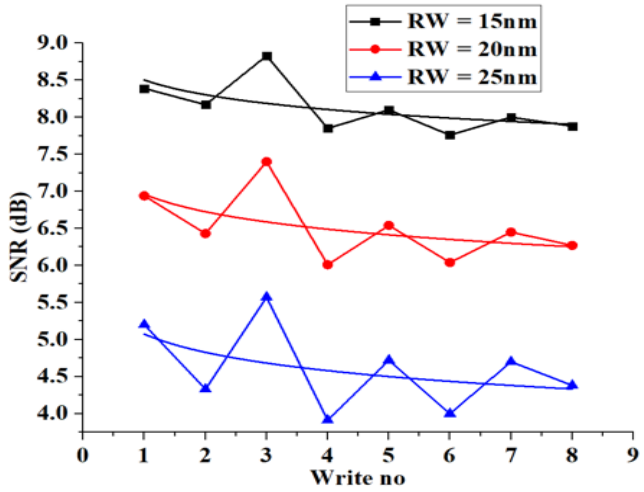

Fig. 8.7 SNR variation for the 6nm single layer FePt media with a staggered PRBS used to overwrite Track 2.

PRBS on Track 2	RW=15nm	RW = 20nm	RW = 25nm
Same very time	-0.30dB	-0.36dB	-0.39dB
Staggered	-0.28dB	-0.30dB	-0.35dB

Table 7. Numerical extent of ATE in the 6nm single layer FePt media for different nature of PRBS used to overwrite Track 2

Unlike the previous cases, different randomized bit sequences are used to overwrite Track 2. Fig. 8.7 shows the SNR variation for this writing process. Table 7 compares the SNR decrease with each write of Track 2 (value of parameter B) for the cases where the PRBS is staggered and PRBS is the same. Comparing the two values for different RW

makes it obvious that ATE is the dominant effect in the multitrack writing process for HAMR and ATI is minimal.

8.4 Optimizing HAMR media to reduce ATE

The presence of a finite ATE effect in all the HAMR media analyzed until this point raises several concerns with respect to the achievable performances for these media especially in the presence of realistic thermal gradients and imperfect fabrication processes. The ATE effect is clearly a limiting factor to the achievable storage densities for different HAMR media designs. Consequently, it is important to introduce optimization techniques to counter the ATE and make these media resistant to ATE. There are three main optimization techniques that are implemented in an effort to reduce the ATE effect in different HAMR media. Their efficacy is measured by the increase in the starting SNR (when Write Number = 1 or both Track 1 & 2 are written once) and the reduction in ATE. The aim is to maximize the SNR after eight overwrites of Track 2. For the single layer FePt media, since a low thickness leads to the highest ATE, the 6nm media is analyzed to explore ATE reduction. This also helps reduce the simulation time.

Applied field angle (in °)	RW=15nm	RW = 20nm	RW = 25nm
0°	-0.18dB	-0.30dB	-0.38dB
15°	-0.31dB	-0.34dB	-0.37dB
22°	-0.30dB	-0.36dB	-0.39dB
30°	-0.34dB	-0.40dB	-0.42dB
45°	-0.27dB	-0.36dB	-0.39dB

Table 8. ATE for different applied field angles for the 6nm single layer FePt media

8.4.1 Change Applied Field Angle

Changing the applied field angle helps alter the written track width and thus the integrity of the written patterns. By default, the applied field angle is 22º since it has been identified as the optimum applied field angle for single-track writing on different HAMR media[104][149]. For writing two tracks in the CT direction, the applied field angle is

varied from 0º to 45º. Here the applied field angle refers to the angle for the applied field with respect to the z axis in the X-Z plane where X denotes the downtrack direction and Z is the vertical direction. Fig. 8.8 (a) – (d) shows the recording performance for the 6nm thick single layer FePt media for different applied field angles. Fig. 8.4 refers to the performance of this media for the applied field angle of 22º. Table 8 shows a comparison for the ATE effect for different applied field angles and RW values. From Fig. 8.4 and Fig. 8.8 (a) – (d) as well as Table 8, it is clear that the ATE effect in the single layer FePt media is mostly impervious to the applied field angle except for a small dip at 0º.

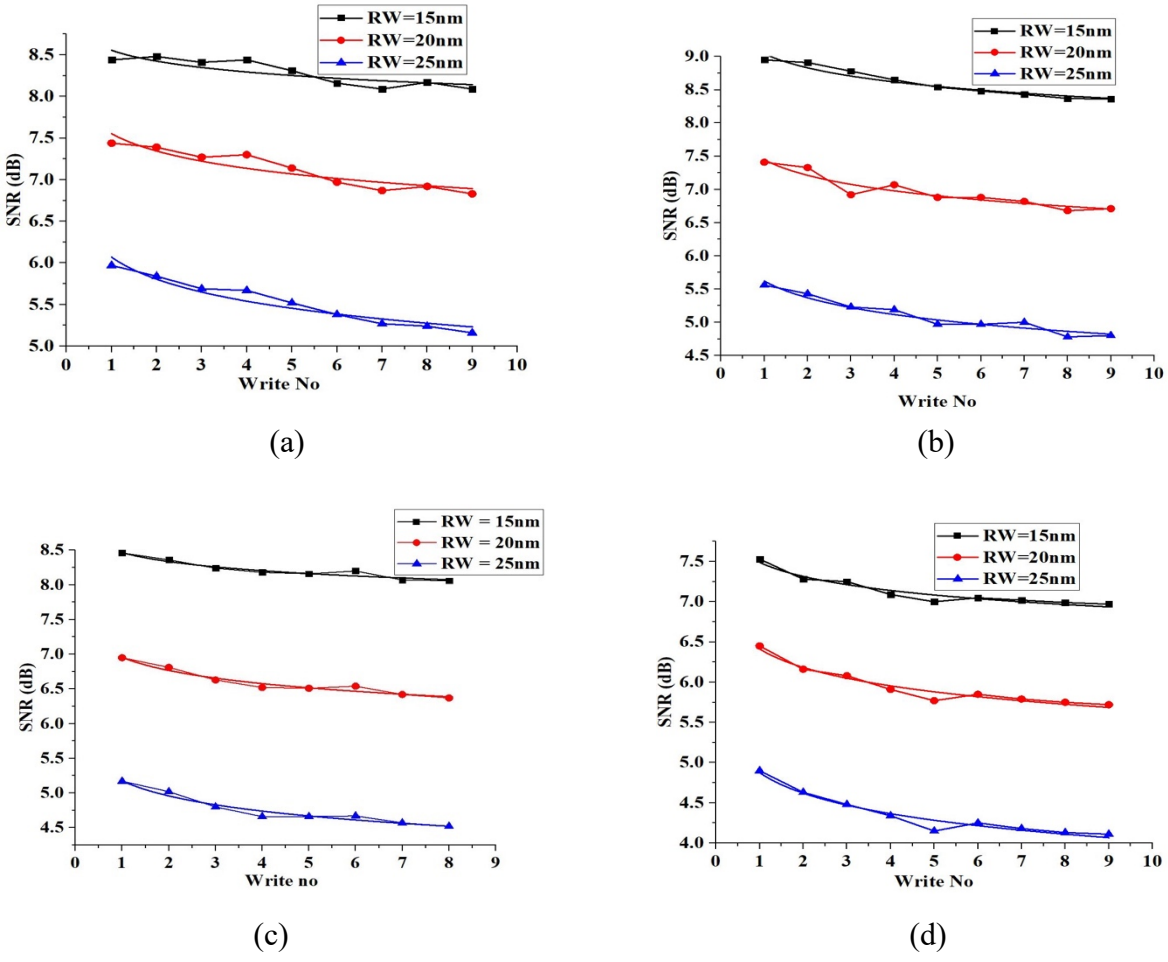

Fig. 8.8 SNR variation for different values of applied field angles for the single layer FePt media (a) 0º (b) 15º (c) 30º (d) 45º

Applied field angle (in °)	RW=15nm	RW = 20nm	RW = 25nm
0°	-0.13dB	-0.23dB	-0.30dB
15°	-0.20dB	-0.28dB	-0.32dB
22°	-0.19dB	-0.24dB	-0.25dB
30°	-0.33dB	-0.39dB	-0.40dB
45°	-0.34dB	-0.41dB	-0.40dB

Table 9. ATE effect for different applied field angles for the 3nm-6nm high temperature Thermal ECC media

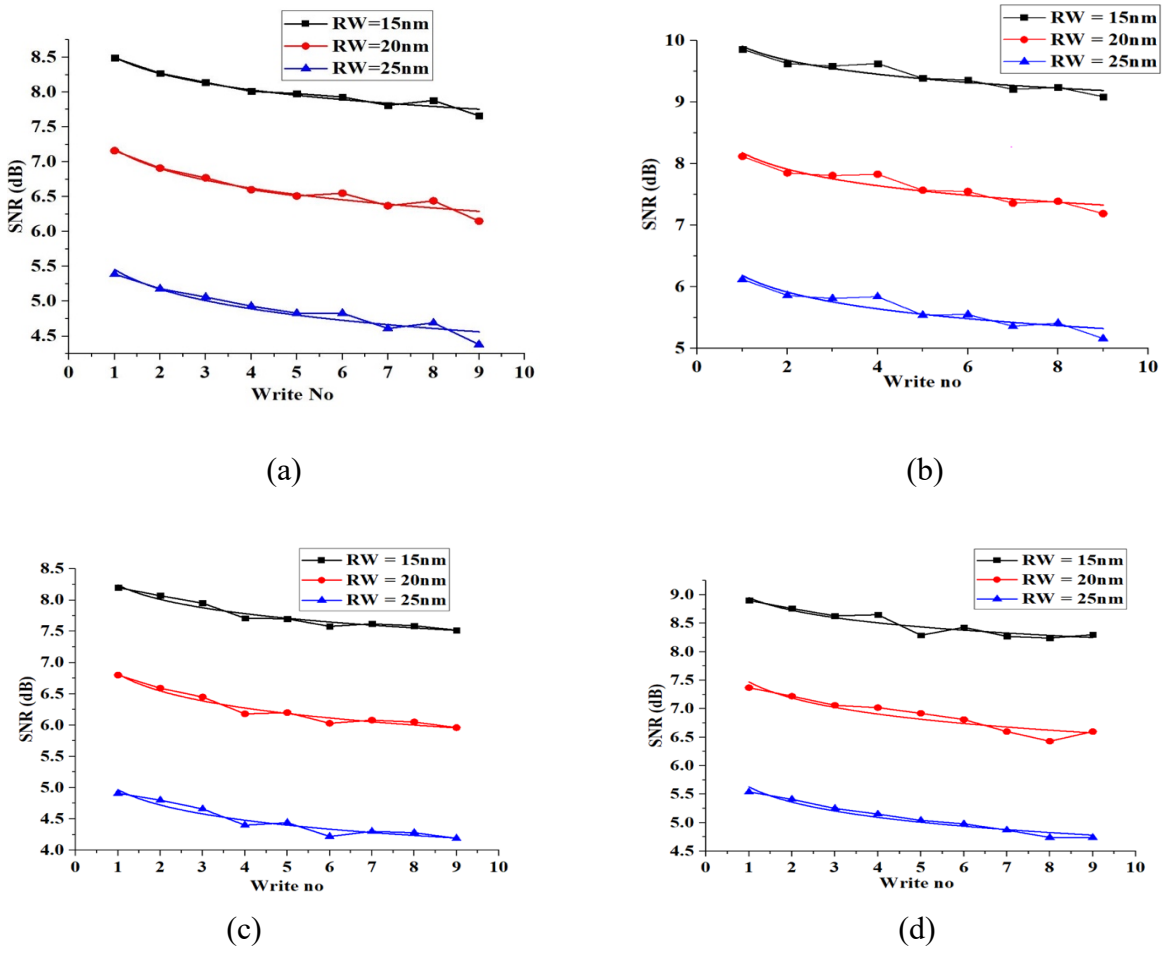

Fig. 8.9 SNR variation for different values of applied field angles for the high T_c Thermal ECC media (a) 0º (b) 15º (c) 30º (d) 45º

For the high temperature Thermal ECC media, a similar process is used, and the applied field angle is varied. Fig. 8.9 (a) - (d) shows the recording performances for the high temperature Thermal ECC media There is an increase in the starting SNR by almost 1.4dB as the applied field angle changes from 22º to 30º. Table 9 indicates the reduction in ATE for this media as the applied field angle reduces from 22º to 0º. Since a lower ATE would indicate a better recording performance after multiple overwrites, it is necessary to analyze the performances at 30º and 0º to identify the better performance. Comparing the starting SNR and the SNR decrease for both the cases of applied field angle 30º (where the starting SNR is the highest) and 0º (where the ATE is the lowest) yields a result that the SNR with applied field angle 30º would be lower than the SNR with field angle 0º after 42,650 overwrites. Thus, for all practical purposes, applied field angle 30º can ensure a better performance in the presence of hundreds of overwrites.

Applied field angle (in °)	RW=15nm	RW = 20nm	RW = 25nm
0°	-0.46dB	-0.46dB	-0.54dB
15°	-0.48dB	-0.49dB	-0.46dB
22°	-0.50dB	-0.50dB	-0.46dB
30°	-0.63dB	-0.63dB	-0.57dB
45°	-0.66dB	-0.64dB	-0.60dB

Table 10. ATE effect for different applied field angles for the 3nm-6nm low temperature Thermal ECC media

For the low temperature Thermal ECC media, Fig. 8.10 (a) - (d) shows the recording performance for different applied field angles. In this case, there is no improvement in the starting SNR for different applied field angles especially when compared with Fig. 8.6 which shows the recording performance for this media with the default applied field angle. Table 10 also indicates that for different applied field angles, there is no reduction in the ATE susceptibility for this media. This indicates that the low H_k for the individual grains and reduced recording thermal gradient that causes a high ATE for this media cannot be overcome by changing the applied field angle.

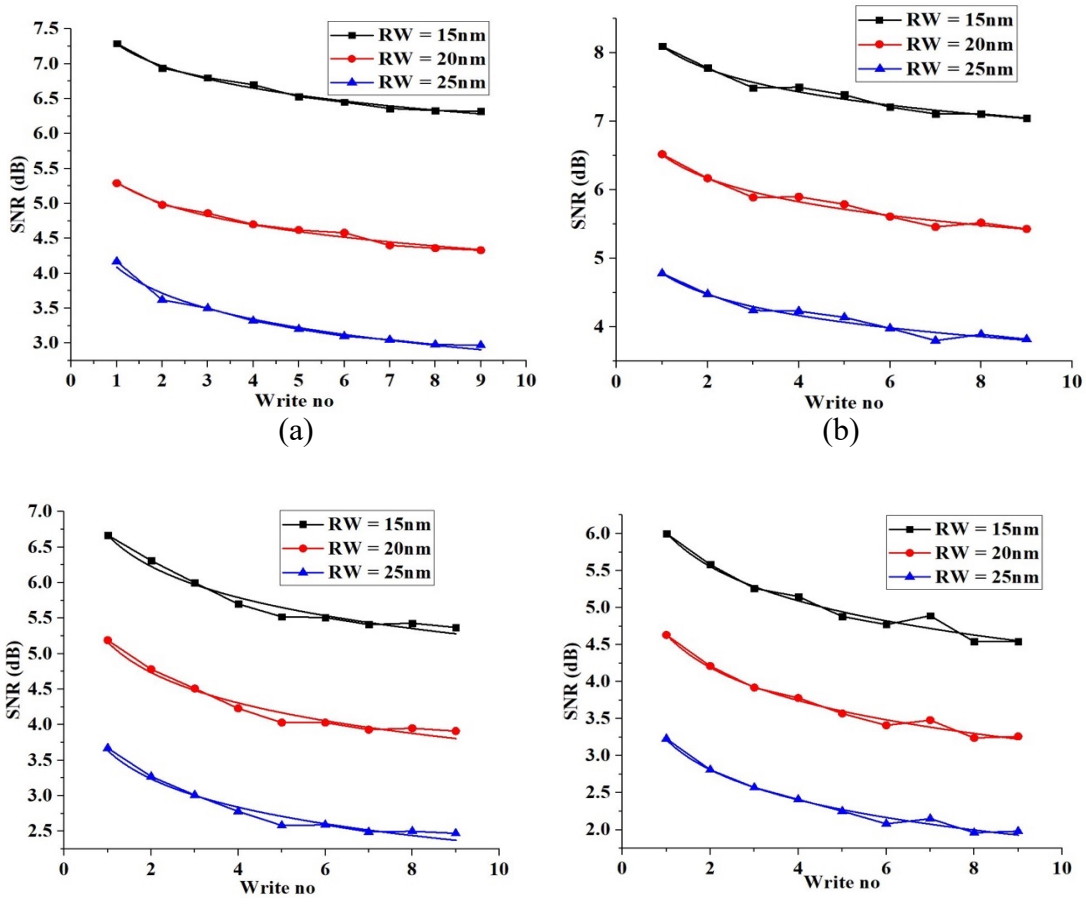

Fig. 8.10 SNR variation for different values of applied field angles for the low T_c Thermal ECC media (a) 0º (b) 15º (c) 30º (d) 45º

8.4.2 Introducing finite Intergranular Exchange Coupling (IGC)

In the implemented micromagnetic simulations, individual grains were assumed to be decoupled from each other. In the Thermal ECC media, there always exists a coupling between the write and storage layer (interlayer exchange coupling) but the grains within the write and storage layer were magnetically isolated. The approach of using finite intergranular exchange coupling (IGC) between the grains of the HAMR media has been used before[142] successfully to improve the SNR in a single-track writing process. This

exchange coupling is introduced as a fraction of the renormalized exchange at different temperatures. Practically, this can be done by introducing a metallic interlayer between the grains of the media, although this may lead to a small thermal bloom. Fig. 8.11 (a) - (c) illustrates the recording performance of the 6nm single layer FePt media with a finite IGC introduced between the grains of the media. There is a slight improvement in the starting SNR by about 0.5dB as a 5% IGC is introduced. Table 11 shows the ATE performance in the presence of the IGC. Clearly introducing a 5% IGC is advantageous to the single layer FePt media since it increases the starting SNR and reduces the ATE significantly.

IGC (%)	RW=15nm	RW = 20nm	RW = 25nm
0	-0.30dB	-0.36dB	-0.39dB
5	-0.20dB	-0.25dB	-0.27dB
10	-0.18dB	-0.26dB	-0.31dB
15	-0.30dB	-0.40dB	-0.46dB

Table 11. ATE effect for different IGC values for the 6nm single layer FePt media

IGC (%)	RW=15nm	RW = 20nm	RW = 25nm
0	-0.19dB	-0.24dB	-0.25dB
5	-0.16dB	-0.23dB	-0.25dB
10	-0.31dB	-0.34dB	-0.35dB
15	-0.19dB	-0.24dB	-0.23dB

Table 12. ATE effect for different intergranular exchange coupling (IGC) values for the 3nm-6nm high temperature Thermal ECC media

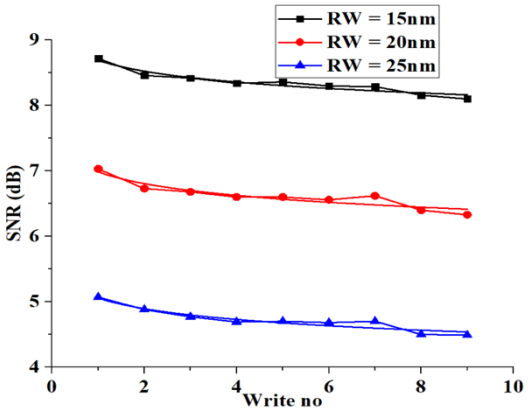

(a)

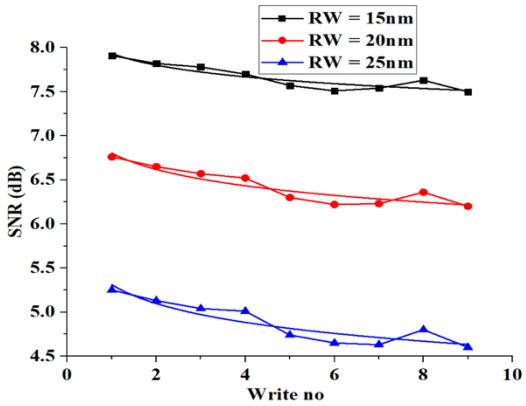

(b)

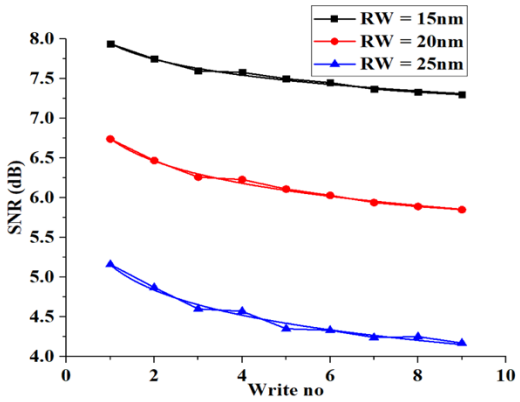

(c)

Fig. 8.11 SNR variation for different values of intergranular exchange coupling (IGC) for the single layer FePt media (a) IGC = 5% (b) IGC = 10% (c) IGC=15%

IGC (%)	RW=15nm	RW = 20nm	RW = 25nm
0	-0.50dB	-0.50dB	-0.47dB
5	-0.49dB	-0.47dB	-0.43dB
10	-0.73dB	-0.71dB	-0.68dB
15	-0.57dB	-0.66dB	-0.54dB

Table 13. ATE effect for different intergranular exchange coupling (IGC) values for the 3nm-6nm low temperature Thermal ECC media

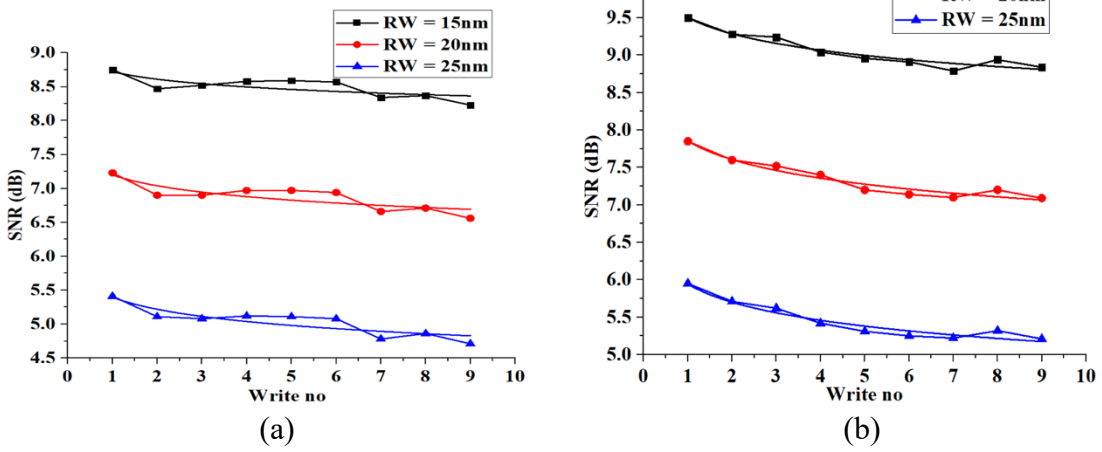

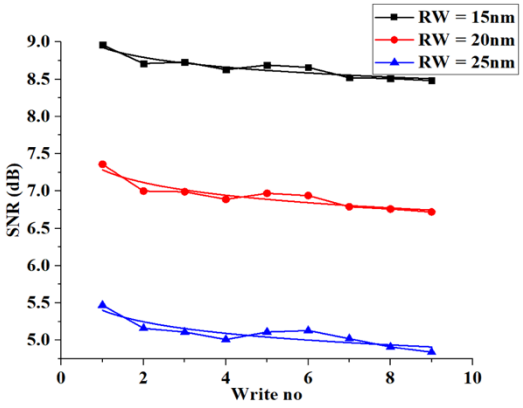

(c)

Fig. 8.12 SNR variation for different values of intergranular exchange coupling (IGC) for the high T_c Thermal ECC media (a) IGC = 5% (b) IGC = 10% (c) IGC=15%

Fig. 8.12 (a) - (c) shows a similar recording performance for the high temperature Thermal ECC media. In this case, IGC is introduced only between the grains of the write layer, since it can help attain the high SNR values without involving the design flexibility of the storage layer. As expected, the starting SNR increases by about 1dB if a 10% IGC is introduced between the grains of the write layer in this media. However, as can be seen from Table 12, this introduction of 10% IGC also makes the structure more susceptible to ATE. Comparing the SNR in the absence of IGC (and the lowest ATE) to the SNR when IGC = 10%, it is found that the SNR with IGC = 10% is lower than the SNR in the absence of IGC after 1179 overwrites. Thus, once again, improving the starting SNR helps attain a better recording performance after multiple overwrites on this media.

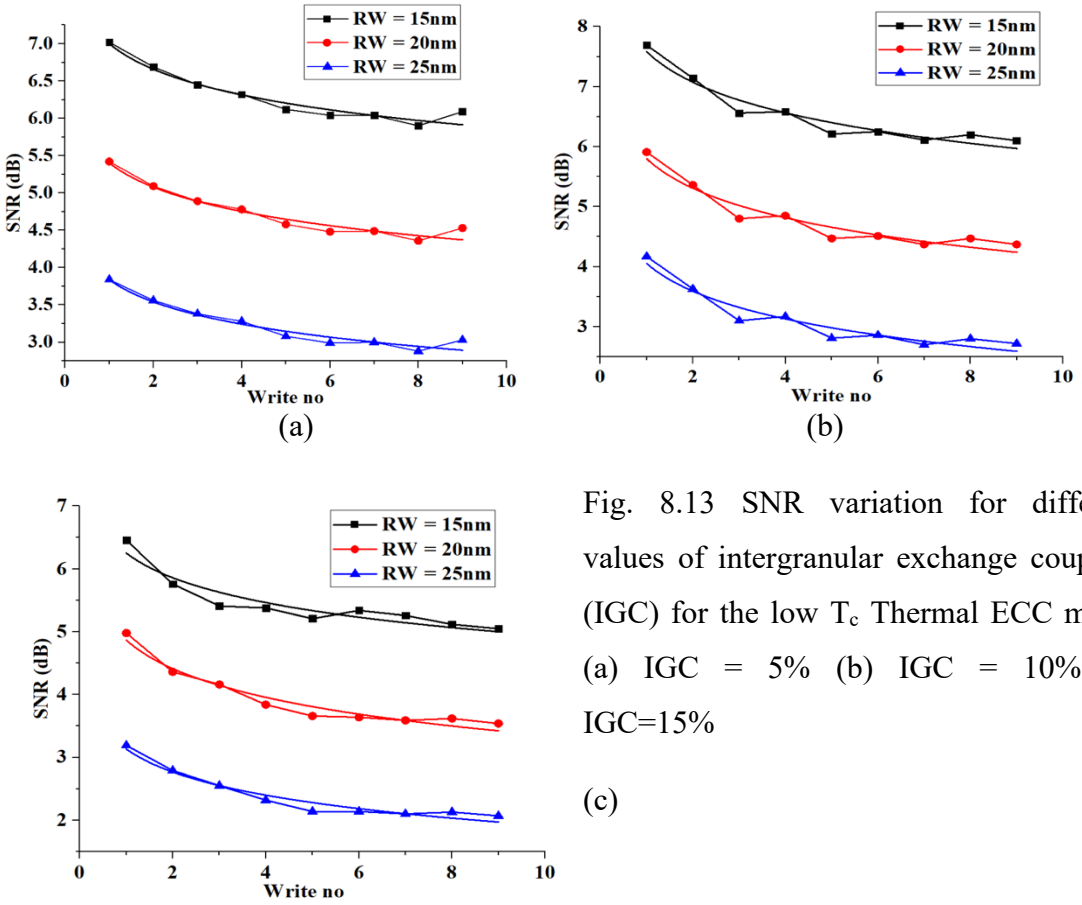

Fig. 8.13 SNR variation for different values of intergranular exchange coupling (IGC) for the low T_c Thermal ECC media (a) IGC = 5% (b) IGC = 10% (c) IGC=15%

Fig. 8.13 (a) - (c) shows the recording performance for the low temperature Thermal ECC media in the presence of a finite IGC value. In this case, there is no improvement in the starting SNR. Table 13 shows that the structure still remains quite susceptible to ATE in spite of the presence of IGC. Thus, similar to the variation in the applied field angle, the low H_k for the individual grains and poor recording thermal gradient are major issues that the media has to contend with despite any remediation offered by exchange coupling.

8.4.3 Explaining the high SNR-high ATE phenomena

In the process of optimizing the HAMR media to reduce the ATE susceptibility and improve the starting SNR, one interesting observation is that increase in the starting SNR

is sometimes accompanied by an increase in the ATE susceptibility. This is especially true in the case of the high temperature Thermal ECC media where increasing the applied field angle from 22º to 30º increases the starting SNR but also increases the ATE susceptibility. Similarly, introducing a 10% IGC increases the starting SNR and the ATE effect. To understand why the higher SNR materials have a higher ATE susceptibility, we consider the individual Signal Power (SP) and Noise Power (NP) used to calculate the SNR and the corresponding ATE effect. Since the SP values for the computation of SNR's for different field angles and IGC values are very similar, the NP is the only significant factor. Fig. 8.14 (a) shows the different NP values for different applied field angles for the high temperature Thermal ECC media. Fig. 8.14 (b) shows the NP values for the case where IGC = 0 and IGC = 10%. Both figures show that the set of parameters that yield the lowest noise power result in the highest starting SNR.

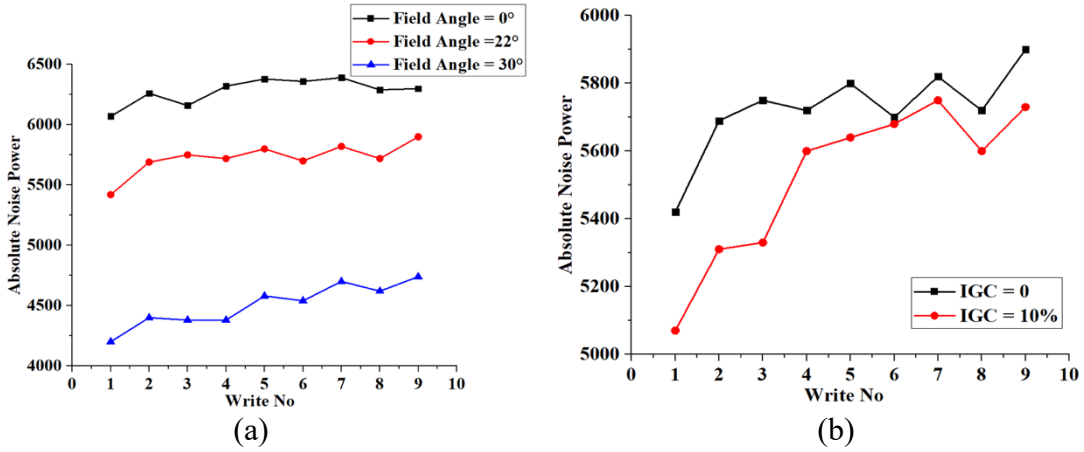

Fig. 8.14 Absolute Noise Power (arbitrary units) for different cases of (a) applied field angles (b) different cases of intergranular exchange coupling in the write layer. Higher the noise power, lower the starting SNR

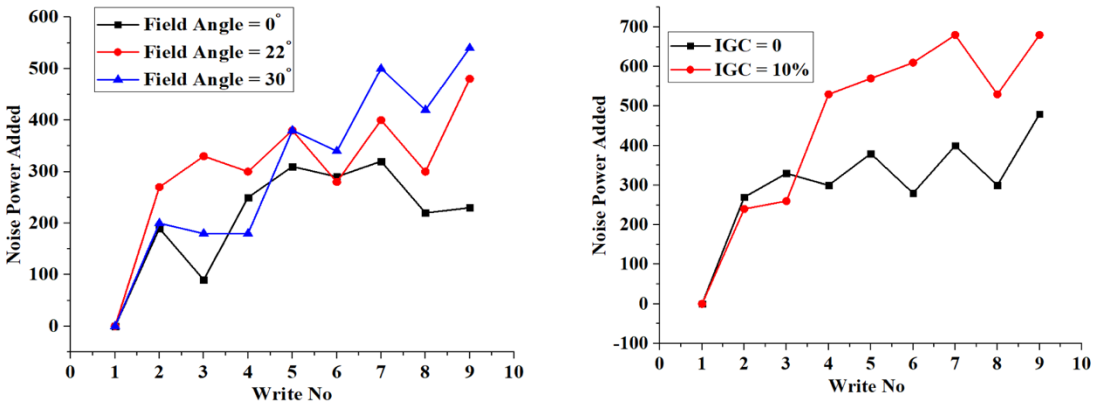

(a) (b)

Fig. 8.15 Noise Power added for (a) different values of applied field angles (b) different values of write layer intergranular exchange coupling. The added noise power value is calculated relative to the noise power in the absence of overwrites (Write No = 1). Higher the added noise power, higher the SNR decay and higher the ATE effect

To understand why they also generate the highest SNR decrease, an analysis is implemented for the Noise Power added every time Track 2 is overwritten. In other words, the added Noise Power when Write No = 1 is assumed to be zero and the added Noise Power with respect to the value when Write No = 1 is plotted. Fig. 8.15 (a) and (b) show the increase in the noise power for the two different cases of field angles and IGC values under consideration. It is clear that the parameters that lead to the highest SNR decay also have the highest added Noise Power. Thus, we see that there is genuinely more noise added to the high SNR media, as opposed to merely more relative noise.

8.5 ATE reduction using a pulsed laser

In the HAMR process, the laser is used to heat up the HAMR media to decrease its coercivity. Normally, the laser is switched on for a specific amount of time and the relative motion of the head and the media allows the laser guided by the NFT to heat up different spots on the HAMR media. An alternate HAMR process has been implemented in previous research where instead of the laser continuously heating the media beneath

the Near Field Transducer, a pulsed laser is used[127][164][165][166]. With the use of the pulsed laser, the media temperature both rises and falls more abruptly.

The accurate modeling of media temperature using a laser pulse has not been reported in the HAMR literature. Simulations have been implemented previously with the use of a pulsed laser, but the characteristic constants seem to not be carefully obtained. For example, it is speculated that since the temperature of the media rises faster than the fall in the temperature, the temperature variation can be characterized by two different time constants, one for the rise time and one for the fall time. Additionally, looking at the decreasing temperature variation from Fig. 15a in [88], the time constant for the falling temperature curve has been speculated to be about 0.7ns. However, linear processes (or energy conservation) demand that the rise and fall time constants should have the same value. Thus, before micromagnetic simulations are implemented using a pulsed laser, the idea behind laser pulsing is understood in detail. The speculations made in this context are revisited and an analytical formulation is derived to calculate the media temperature as a function of the in-plane coordinates (x,y) and time (t).

8.5.1 Analytical formulation

To realize the temperature variation due to laser pulsing, it is understood that when the laser heats up the HAMR media, it delivers power to the media in the form of a temperature rise via a Gaussian spot. In the analytical formulation, a fitting constant ‘A’ is assumed to represent the increase in temperature from 300K due to the laser power. The decay constant for the temperature variation is assumed to be τ. As explained before, the same constant is assumed for both the rising and falling parts of the temperature curve. To make an accurate estimation of the media temperature, an analytical formulation that can help capture the temperature at different instants of time is derived. To do so, it is understood that the temperature (T) at a time (t) is equal to the room temperature (300K) plus the additional power supplied by the laser in the form of temperature till time ‘t’. In other words, it is a sum of the room temperature and all the

Gaussians generated till time t. The general form of this Gaussian is written below in equation 8.2

$$T(x,y,t) = 300 + \left(\frac{A-300}{B}\right) \times \left[\int_0^t e^{\frac{-((x-vt')^2)}{2\times\sigma^2}} \times e^{\frac{-(y^2)}{2\times\sigma^2}} \times e^{-\frac{t-t'}{\tau}} dt'\right] \quad (8.2)$$

Here A, B, σ and τ are the fitting parameters. σ relates to the heat spot FWHM. The integral in equation (8.2) can be solved by completing the squares in the index of the exponential inside the integral. Doing so allows the temperature at a time instant 't' to be written as

$$T(x,y,t) = 300 + \left[(A') \times e^{\frac{-y^2}{2\sigma^2}} e^{\frac{-1}{2v\tau}\left(2vt-2x-\frac{\sigma^2}{v\tau}\right)} \left(\frac{\sqrt{\pi}}{2}\right)\left(\frac{\sqrt{2}\sigma}{v}\right) \times \left[\operatorname{erf}\left(\frac{\left(x+\frac{\sigma^2}{v\tau}\right)}{\sqrt{2}\sigma}\right) - \operatorname{erf}\left(\frac{\left(x+\frac{\sigma^2}{v\tau}-vt\right)}{\sqrt{2}\sigma}\right)\right]\right] \quad (8.3)$$

Here, the fitting constant ((A-300)/B) is written as A′. This analytical formulation is derived without making any explicit assumptions about the values of the parameter constants involved or without assuming the nature of the temperature curve.

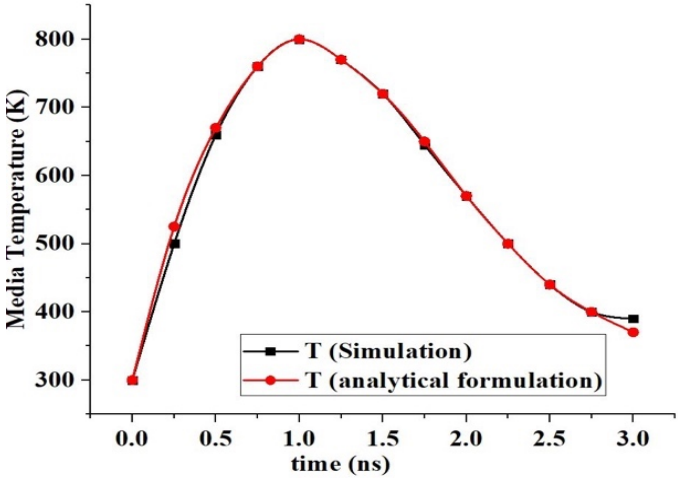

Fig. 8.16 Comparison of media temperature for temperature calculated from two sources. T(Simulation) refers to Fig. 15a from [88] and T(analytical formulation) refers to temperature calculated from equation (8.3)

8.5.2 Result comparison for continuous laser power

The accuracy of the analytical formulation in equation (8.3) can be verified by comparing to previously published values. The comparison is implemented for temperature values calculated from the analytical formulation with the temperature values from Fig. 15a in [88]. Fig. 8.16 shows the comparison of the temperature values. The black curve with the square symbols shows the temperature values from Fig. 15a in [88] calculated by a Finite Difference Time Domain (FDTD) method with a 0.5nm length scale and a thermal heat flow simulation. The red curve with the circular symbols shows the values calculated from the analytical formulation. The value of the time constant for the analytical formulation derived from this comparison is 0.38ns. This value for the time constant is interesting in two aspects (i) It is smaller than the naive value of 0.7ns (ii) It confirms the theory that the same time constant can be used to describe both the rising and falling curves in the temperature variation curve, where the asymmetry is only due to the motion of the head relative to the media. The values of fitting parameters 'A' and 'B' from equation (8.2) are estimated to be 700K and 0.17ns respectively.

8.5.3 Temperature calculation for discontinuous laser power

The pulsed laser technique used to write on the HAMR media involves the use of a pulse that is continuously switched on and off with a certain duration/frequency. The analytical formulation derived in equation (8.3) is done so by integrating all the Gaussians generated till time 't'. When the laser is switched off, no additional power is delivered to the HAMR media. In other words, there is no possibility for an increase in the media temperature and the temperature decreases with a certain rate as decided by the decay constant (τ) in the analytical formulation. In the micromagnetic simulations implemented with the use of a pulsed laser, the laser is assumed to be switched on at t=0ns and then switched on and off every 0.5ns. As an example, assume the time instance between $1.5\text{ns} \leq t \leq 2\text{ns}$, in this case the laser is switched on twice (from 0ns to 0.5ns and from 1.0ns to 1.5ns) and the media temperature is a sum of the temperatures decaying from 0.5ns onward and 1.5ns onward. In general, for a discontinuous power laser pulse where

the laser is switched on and off every 0.5ns, the general technique to write the analytical formulation is shown in equation (8.4). The […] terms indicate a sum of error functions that are generated when the laser is switched on and off every time.

$$T(x,y,t) = 300 + A' \times e^{\frac{-y^2}{2\sigma^2}} \times e^{\frac{-1}{2v\tau}\left(2vt-2x-\frac{\sigma^2}{v\tau}\right)} \left(\frac{\sqrt{\pi}}{2}\right)\left(\frac{\sqrt{2}\sigma}{v}\right) \times \left[\left[\operatorname{erf}\left(\frac{\left(x+\frac{\sigma^2}{v\tau}\right)}{\sqrt{2}\sigma}\right) - \operatorname{erf}\left(\frac{\left(x+\frac{\sigma^2}{v\tau}-v(0.5ns)\right)}{\sqrt{2}\sigma}\right)\right] + \left[\operatorname{erf}\left(\frac{\left((x-v(1.0ns))+\frac{\sigma^2}{v\tau}\right)}{\sqrt{2}\sigma}\right) - \operatorname{erf}\left(\frac{\left((x)+\frac{\sigma^2}{v\tau}-v(1.5ns)\right)}{\sqrt{2}\sigma}\right)\right] + [\ldots]\right] \quad (8.4)$$

Fig. 8.17 shows the temperature curve for a pulsed laser process derived from the analytical formulation. Since the pulse is switched on and off every 0.5ns, the rise and fall in temperature is clearly visible in the figure. The temperature is obtained by averaging over a spot directly below the NFT at different instants of time.

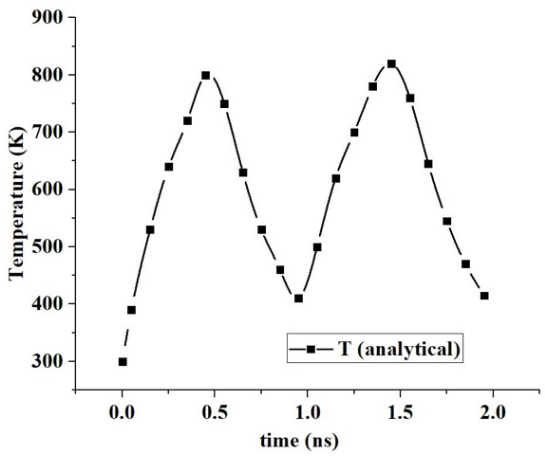

Fig. 8.17 Media temperature calculated from the analytical formulation for pulsed laser switched on and off every 0.5ns.

8.5.4 Pulsed Laser recording performance

The objective of using a pulsed laser technique is to explore possible reductions in the ATE susceptibility for different HAMR media. For a Gaussian heat spot used to write on different HAMR media, previous efforts[104] have identified the optimum peak

Obs. No	Simulation Condition	Parameter A value	SNR (dB)
1	Laser continuously on	700K	10.3
2	Pulsed laser switched on and off every 0.5ns	900K	9.6
3		1000K	9.8
4		1200K	10.0
5		1500K	9.2

Table 14. Single track recording performance for the 6nm single layer FePt media written using the pulsed laser. In lines 2-5, laser was switched on and off every 0.5ns.

temperature of 850K that can yield the best SNR. However, for the pulsed laser, before the ATE performance can be measured, it is necessary to identify the optimum temperature (value of parameter A in equation (8.2)) for the micromagnetic simulations. To identify this value, a single-track recording simulation is implemented where a single tone sequence is written on the HAMR media. The values of the other parameters are taken to be the same as the ones that generated the fitting curve in Fig. 8.16. Table 14 shows the SNR variation for the single-track writing implemented for different values of parameter A, assuming the pulse is synchronized to the change in field direction. These values are calculated for the 6nm single layer FePt media, read back at RW=15nm. The SNR values are compared to the SNR calculated for a similar single-track writing process where the laser is continuously illuminated. It is clear that single track writing with pulsed laser recording can yield SNR values comparable to the case where the laser is continuously on.

A similar process to calculate the ATE as explained before is implemented for the 6nm single layer FePt media where tracks are written using the pulsed laser for different values of parameter (A) and RW=15nm. Early estimates in Table 15 show that the starting SNR (calculated for the single tone sequence written on Track 1 when Track 1 and Track 2 are both written once) has a poor value compared to its counterpart SNR value when the 6nm FePt media is written using continuous illumination. This may be attributed to the written track width modulating with the pulsing. Clearly, there is both

Obs. No	Simulation Condition	Parameter A value	SNR (dB)
1	Laser continuously on	575K	7.5
	Pulsed laser switched on and off every 0.5ns	700K	7.9
2		900K	5.2
3		1000K	6.5
4		1200K	4.8

Table 15. SNR for the single tone sequence written on Track 1 when both Track 1 and Track 2 are written once. This SNR is referred to as the starting SNR in the text.

opportunity and need for optimization that might improve the recording performance when closely spaced tracks are written using pulsed laser recording.

8.6 Hypothesis for ATE in HAMR

The numerical extent of ATE has been established for different thicknesses of the HAMR media as well as the low temperature and high temperature Thermal ECC media. It is

Media	Thickness (nm)	$T_{write} - 50K$	K_uV/k_BT
Single Layer FePt	6	623.3K	31.36
Single Layer FePt	7.5	623.9K	39.2
Single Layer FePt	9	624.5K	47.05
High T_c Thermal ECC	3 (Write Layer) 6 (Storage Layer)	633K	31.8
Low T_c Thermal ECC	3 (Write Layer) 6 (Storage Layer)	445K	49.45

Table 16. Thermal stability factors for different HAMR media assuming coherent rotation. A larger stability factor should indicate a lower ATE susceptibility.

clear that the finite presence of ATE is detrimental to the recording performance of these media. In order to reduce the ATE, it is necessary to explain why ATE exists in different HAMR media. This analysis would help understand the factors that have a dominant

effect on the ATE in different media thus guiding the media designers to explore ways to counter ATE by modifying these factors.

The ATE depends mainly on the integrity of the written patterns and the ability of different grains in a certain track to maintain their magnetizations in the presence of the writing process being implemented on an adjacent track. Thus, it is possible the ATE effect depends on the thermal stability of the grains in the HAMR media or the thermal stability factor. Since most of the writing process takes place at temperatures close to and slightly lower than the writing temperature (T_{write}), a hypothesis is established that the ATE in HAMR media is proportional to the thermal stability factor (K_uV/k_BT) at a temperature T just below (about 50K below) the write temperature.

To test the hypothesis, we identify the thermal stability factor for different HAMR media based on the value of T_{write}. For the Thermal ECC media, we assume coherent rotation in the write and storage layer. Table 16 shows the ATE effect based on the established hypothesis. It is clear that the hypothesis can explain the ATE effect in different thicknesses of the FePt media correctly. However, coherent rotation cannot correctly account for the ATE in the Thermal ECC media. For the Thermal ECC media, other mathematical techniques that capture incoherent rotation will be needed to calculate the thermal stability factor and verify this hypothesis. Establishing this hypothesis helps understand the scientific principle behind the existence of ATE in HAMR and should help reduce the ATE for different HAMR media.

8.7 Summary

This work was supported by Seagate Technology. The chapter explores the presence and extent of the ATE issue in the HAMR media. The finite extent of ATE in different HAMR media leads to an inevitable conclusion: efforts must be made to improve the heat spot profile, attain a better control over the magnetic properties of the granular media as well as control the applied field magnitude and angle to ensure the lowest erasure. The ATE presence in the high temperature Thermal ECC media seems to be higher than the single layer FePt media with equivalent thickness but lower than the single layer FePt

media with lower equivalent thickness. This ATE phenomena has a significantly high presence in the low temperature Thermal ECC media, that displayed a comparable single-track recording performance as the high temperature Thermal ECC media. Since the reduction in writing temperature and the use of the low temperature Thermal ECC media is a necessary development, other techniques must be explored to reduce the ATE especially for this media. Changing the applied field angle and introducing finite intergranular exchange coupling are techniques that show promising results to reduce the ATE for both the single layer FePt media and the high temperature Thermal ECC media.

An improved understanding of heat flow allows the implementation of a pulsed laser within micromagnetic simulations. The use of a pulsed laser technique instead of a laser that is continuously illuminating the HAMR media shows promising results especially for the single-track writing. Future studies for the laser pulsing technique include optimization of the peak temperature of the pulse and variation in the synchronization of the head field and pulse duration to further improve the performance using this technique. The detailed analysis of the ATE effect will be instrumental in improving the AD values in the HAMR process.

Chapter 9

Conclusion & Outlook

Different chapters in this thesis have focused on different aspects of the HAMR system. HAMR is an exciting technology and the primary hope for the HDD storage industry that has invested a lot of monetary capital and research in this area. Chapter 1 described the basic concepts in the field of magnetism including the concepts closely related to the field of HAMR like thermal stability and switching probability. Chapter 2 described in detail, different components of the HDD system and the function of each of the components that contribute to the data recording process. Chapter 3 introduced the concept of HAMR and different components specific to the HAMR system. The HAMR system has additional components compared to the PMR system like the light delivery path (including the NFT), the media with high anisotropy and additional layers like the heatsink and recording layer lubricant that have specific demands in terms of their magnetic, thermal and mechanical properties.

Chapter 4 describes the magnetic parameters calculated for a doped/non-stoichiometric model of anisotropic FePt. This parameter calculation helps increase the accuracy of micromagnetic simulations implemented for realistic FePt models with granular T_c variation. Chapter 5 enumerated different approaches for optimizing a thinner version of high temperature Thermal ECC media. This thinner media is easier to fabricate and ensures higher throughput in the fabrication process compared to a thicker media. The optimization approaches included scaling the damping and introducing finite intergranular exchange coupling between the grains of the recorded media that helped reduce the DC noise and improve the recorded SNR. Chapter 6 describes a new proposed structure for Thermal ECC media called the low temperature Thermal ECC media. The objective of proposing this media is to reduce the writing and recording temperature in the HAMR process. The high temperatures involved in the HAMR process can not only potentially degrade the lubricant used to protect the media, but also demand the use of a

highly conducting heat sink in the presence of insulating seed layers like MgO. Additionally, these high temperatures can also lead to a melting of the NFT material which is normally gold (Au). Overall, the high temperatures constitute the biggest impediment to the commercial success of HAMR and the low temperature Thermal ECC media can act as a potential solution to this issue. Chapter 7 derived an analytical formulation to calculate the transition jitter in the HAMR process. This analytical formulation is tested by comparing the results for different media variations and simulation conditions to micromagnetic simulations that are far more complex and time consuming. This analytical formulation is useful in filling the void currently present in the HAMR literature for a simple fast analytical method to estimate transition jitter.

The final chapter of the thesis deals with the analysis of Adjacent Track Erasure (ATE) in the HAMR media, which is a consequence of writing closely spaced tracks. In the effort to improve the HAMR storage density, ATE is a natural consequence and hence its reduction is an extremely important aim for research groups throughout the data storage industry. In the thesis, the numerical extent of ATE in different HAMR media is established and different techniques are used to reduce the susceptibility of different HAMR media to the ATE effect. A new interesting technique of using a pulsed laser to write on the HAMR media is discussed in this chapter. This technique has tremendous potential based on the early positive results obtained for the single layer FePt media. This technique can be implemented for other HAMR media and can be used in conjunction with other techniques to reduce the ATE effect in different HAMR media.

Overall, there is enormous potential for further optimization in the HAMR process to achieve an improved recording performance. The research pertaining to the HAMR technology has been instrumental in establishing the basis for future recording technologies like the Heated Dot Magnetic Recording (HDMR) technology which can improve the HDD storage density even further. Essentially, the HAMR technology is here to stay and has a promising future ahead.

Bibliography

[1] “https://www.computerhistory.org/revolution/birth-of-the-computer/4/78.” .

[2] V. Chen, B.M., Lee, T.H., Peng, K., Venkataramanan, *Hard Disk Drive Servo Systems*. 2006.

[3] “http://www.computersciencelabs.com/hard_drive.” .

[4] “https://www.domo.com/learn/data-never-sleeps-5.” .

[5] “https://www.horizontechnology.com/news/hdd-remains-dominant-storage-technology-1219/.” .

[6] “https://www.zdnet.com/article/by-2025-nearly-30-percent-of-data-generated-will-be-real-time-idc-says/.” .

[7] “https://blog.imarticus.org/role-of-analytics-in-todays-scenario/.” .

[8] “https://i.imgur.com/hibMRfu.png.” .

[9] “https://en.wikipedia.org/wiki/Hard_disk_drive.” .

[10] B. Marilyn, *Introduction to IBM Direct Access Storage Devices*. Sra, 1980.

[11] “http://everything.explained.today/Hard_disk_drive/.” .

[12] “https://www.anandtech.com/show/13764/western-digital-2019-16tb-hdd-mamr-hamr.” .

[13] “https://jcmit.net/disk2015.htm.” .

[14] “https://blocksandfiles.com/2019/08/28/nearline-disk-drives-ssd-attack/.”

[15] B. Schroeder, R. Lagisetty, and A. Merchant, “Flash reliability in production: The expected and the unexpected,” *Proc. 14th USENIX Conf. File Storage Technol. FAST 2016*, pp. 67–80, 2019.

[16] E. Grochowski, “The Magnetic Hard Disk Drive,” pp. 1–27, 2016.

[17] B. Marchon, T. Pitchford, Y. T. Hsia, and S. Gangopadhyay, “The head-disk interface roadmap to an areal density of 4 Tbit/in 2,” *Adv. Tribol.*, no. March 2013, 2013, doi: 10.1155/2013/521086.

[18] A. Fert, “The present and the future of spintronics,” *Thin Solid Films*, vol. 517, no. 1, pp. 2–5, 2008, doi: 10.1016/j.tsf.2008.08.172.

[19] M. A. M. Gijs, S. K. J. Lenczowski, and J. B. Giesbers, “Perpendicular giant magnetoresistance of microstructured Fe/Cr magnetic multilayers from 4.2 to 300 K,” *Phys. Rev. Lett.*, vol. 70, no. 21, pp. 3343–3346, 1993, doi: 10.1103/PhysRevLett.70.3343.

[20] A. Vedyayev, M. Chshiev, N. Ryzhanova, B. Dieny, C. Cowache, and F. Brouers, "A unified theory of CIP and CPP giant magnetoresistance in magnetic sandwiches," *J. Magn. Magn. Mater.*, vol. 172, pp. 53–60, 1997.

[21] P. M. Levy, S. Zhang, T. Ono, and T. Shinjo, "Electrical transport in corrugated multilayered structures," *Phys. Rev. B*, vol. 52, no. 22, pp. 16049–16054, 1995, doi: 10.1103/PhysRevB.52.16049.

[22] M. T. Kief and R. H. Victora, "Materials for heat-assisted magnetic recording," *MRS Bull.*, vol. 43, no. 2, pp. 87–92, 2018, doi: 10.1557/mrs.2018.2.

[23] Z. Shi, M. Salo, J. Zhang, A. Yang, S. Duan, and K. Johnson, "Media noise analysis in shingled magnetic recording," *IEEE Trans. Magn.*, vol. 47, no. 10, pp. 2992–2995, 2011, doi: 10.1109/TMAG.2011.2145362.

[24] H. Nobuhara *et al.*, "Influence of writing ITI effects in shingled magnetic recording," *IEEE Trans. Magn.*, vol. 49, no. 7, pp. 3814–3817, 2013, doi: 10.1109/TMAG.2013.2242439.

[25] M. Salo *et al.*, "The structure of shingled magnetic recording tracks," *IEEE Trans. Magn.*, vol. 50, no. 3, pp. 18–23, 2014, doi: 10.1109/TMAG.2013.2283074.

[26] "https://www.primaryio.com/hard-disk-trends/." .

[27] "https://blog.dshr.org/2018/05/longer-talk-at-msst2018.html." .

[28] "https://www.kitguru.net/components/hard-drives/anton-shilov/tdk-hamr-technology-could-enable-15tb-hard-drives-already-in-2015/." .

[29] "https://www.anandtech.com/show/15064/seagate-18-tb-hdd-due-in-first-half-2020-20-tb-drive-to-ship-in-late-2020." .

[30] "https://blocksandfiles.com/2019/09/03/western-digital-18tb-and-20tb-mamr-disk-drives/." .

[31] "https://computerprojectsduff.fandom.com/wiki/Hard_Drive." .

[32] Y. Jiao, "Simulation of Heat Assisted Magnetic Recording System," 2018.

[33] Z. Vladimir, *Control Systems Design*. Springer, 2005.

[34] "https://www.tomshardware.com/reviews/ssd-reliability-failure-rate,2923-9.html."

[35] H. N. Bertram, *Theory of Magnetic Recording*. Cambridge University Press, 1994.

[36] G. Di Fratta, "Giovanni Di Fratta On the nature of magnetization states minimizing the micromagnetic free energy functional," no. September, 2015, doi: 10.13140/RG.2.1.1606.4488.

[37] "https://encyclopedia2.thefreedictionary.com/Perpendicular+magnetic+recording."

[38] C. H. Hee, J. P. Wang, H. Gong, and T. S. Low, "Effect of orientation ratio on

recording performance for longitudinal thin film media," *IEEE Trans. Magn.*, vol. 36, no. 5 I, pp. 2291–2293, 2000, doi: 10.1109/20.908402.

[39] H. Takano, T. T. Lam, J. G. Zhu, and J. H. Judy, "Effect of orientation ratio on the recording characteristics of longitudinal thin film media," *IEEE Trans. Magn.*, vol. 29, no. 6, pp. 3709–3711, 1993, doi: 10.1109/20.281277.

[40] H. J. Richter, E. Girt, and H. Zhou, "Simplified analysis of two-layer antiferromagnetically coupled media," *Appl. Phys. Lett.*, vol. 80, no. 14, pp. 2529–2531, 2002, doi: 10.1063/1.1467977.

[41] M. E. Schabes, E. E. Fullerton, and D. T. Margulies, "Theory of antiferromagnetically coupled magnetic recording media," *IEEE Trans. Magn.*, vol. 37, no. 4 I, pp. 1432–1434, 2001, doi: 10.1109/20.950862.

[42] E. E. Fullerton *et al.*, "Antiferromagnetically coupled magnetic media layers for thermally stable high-density recording," *Appl. Phys. Lett.*, vol. 77, no. 23, pp. 3806–3808, 2000, doi: 10.1063/1.1329868.

[43] E. N. Abarra, I. Okamoto, and Y. Mizoshita, "Longitudinal magnetic recording media with thermal stabilization," *Dig. Intermag Conf.*, vol. 2581, no. July 2000, pp. 4–7, 2000, doi: 10.1109/intmag.2000.871786.

[44] N. R. Belk, P. K. George, and G. S. Mowry, "Noise in high performance thin-film longitudinal magnetic recording media (invited)," *IEEE Trans. Magn.*, vol. 21, no. 5, pp. 1350–1355, 1985, doi: 10.1109/TMAG.1985.1063973.

[45] D. Weller and M. F. Doerner, "E Xtremely H Igh -D Ensity L Ongitudinal M Agnetic R Ecording M Edia," 2000.

[46] H. N. Bertram, H. Zhou, and R. Gustafson, "Signal to Noise Ratio Scaling and Density Limit Estimates in Longitudinal Magnetic Recording," *IEEE Trans. Magn.*, vol. 34, no. 4 PART 1, pp. 1845–1847, 1998, doi: 10.1109/20.706722.

[47] B. R. Acharya, J. N. Zhou, M. Zheng, G. Choe, E. N. Abarra, and K. E. Johnson, "Anti-parallel coupled soft under layers for high-density perpendicular recording," *IEEE Trans. Magn.*, vol. 40, no. 4 II, pp. 2383–2385, 2004, doi: 10.1109/TMAG.2004.832165.

[48] M. Mallary, A. Torabi, and M. Benakli, "One terabit per square inch perpendicular recording conceptual design," *IEEE Trans. Magn.*, vol. 38, no. 4 I, pp. 1719–1724, 2002, doi: 10.1109/TMAG.2002.1017762.

[49] M. H. Kryder and R. W. Gustafson, "High-density perpendicular recording - Advances, issues, and extensibility," *J. Magn. Magn. Mater.*, vol. 287, no. SPEC. ISS., pp. 449–458, 2005, doi: 10.1016/j.jmmm.2004.10.075.

[50] B. Marchon and T. Olson, "Magnetic spacing trends: From LMR to PMR and beyond," *IEEE Trans. Magn.*, vol. 45, no. 10, pp. 3608–3611, 2009, doi: 10.1109/TMAG.2009.2023624.

[51] S. N. Piramanayagam, “Perpendicular recording media for hard disk drives,” *J. Appl. Phys.*, vol. 102, no. 1, 2007, doi: 10.1063/1.2750414.

[52] H. J. Richter, “The transition from longitudinal to perpendicular recording,” *J. Phys. D. Appl. Phys.*, vol. 40, no. 9, 2007, doi: 10.1088/0022-3727/40/9/R01.

[53] J. Zhang, J. W. Xu, J. K. P. Ng, S. B. Hu, H. X. Yuan, and S. N. Piramanayagam, “Lubrication for Heat-Assisted Magnetic Recording Media,” *IEEE Trans. Magn.*, vol. 42, no. 10, pp. 2546–2548, 2006, doi: 10.1109/TMAG.2006.878650.

[54] S. N. Piramanayagam, C. K. Pock, L. Lu, C. Y. Ong, J. Z. Shi, and C. S. Mah, “Grain size reduction in CoCrPt:SiO2 perpendicular recording media with oxide-based intermediate layers,” *Appl. Phys. Lett.*, vol. 89, no. 16, pp. 88–91, 2006, doi: 10.1063/1.2362643.

[55] J. Z. Shi *et al.*, “Influence of dual-Ru intermediate layers on magnetic properties and recording performance of CoCrPt-SiO2 perpendicular recording media,” *Appl. Phys. Lett.*, vol. 87, no. 22, pp. 1–3, 2005, doi: 10.1063/1.2137447.

[56] S. N. Piramanayagam, H. B. Zhao, J. Z. Shi, and C. S. Mah, “Advanced perpendicular recording media structure with a magnetic intermediate layer,” *Appl. Phys. Lett.*, vol. 88, no. 9, 2006, doi: 10.1063/1.2179112.

[57] R. Mukai, T. Uzumaki, and A. Tanaka, “Microstructure improvement of thin Ru underlayer for CoCrPt-SiO2 granular perpendicular media,” *INTERMAG ASIA 2005 Dig. IEEE Int. Magn. Conf.*, vol. 41, no. 10, p. 788, 2005, doi: 10.1109/intmag.2005.1464221.

[58] O. Kitakami, M. Koizumi, and N. Tsumita, “Noise from Underlayer of Perpendicular Magnetic Recording Medium (2),” *IEEE Transl. J. Magn. Japan*, vol. 1, no. 3, pp. 319–320, 1985, doi: 10.1109/TJMJ.1985.4548576.

[59] R. H. Victora, K. Senanan, and J. Xue, “Areal density limits for perpendicular magnetic recording,” *INTERMAG Eur. 2002 - IEEE Int. Magn. Conf.*, vol. 38, no. 5, pp. 1886–1891, 2002, doi: 10.1109/INTMAG.2002.1001395.

[60] “http://www.nanoscience.de/HTML/research/spin_dynamics.html.” .

[61] J. C. Mallinson, “A New theory of recording media noise,” *IEEE Trans. Magn.*, vol. 27, no. 4, pp. 3519–3531, 1991, doi: 10.1109/20.102923.

[62] D. Weller *et al.*, “Review Article: FePt heat assisted magnetic recording media,” *J. Vac. Sci. Technol. B, Nanotechnol. Microelectron. Mater. Process. Meas. Phenom.*, vol. 34, no. 6, p. 060801, 2016, doi: 10.1116/1.4965980.

[63] T. Matsumoto, F. Akagi, M. Mochizuki, H. Miyamoto, and B. Stipe, “Integrated head design using a nanobeak antenna for thermally assisted magnetic recording,” *Opt. Express*, vol. 20, no. 17, p. 18946, 2012, doi: 10.1364/oe.20.018946.

[64] B. C. Stipe *et al.*, “Magnetic recording at 1.5Pbm-2 using an integrated plasmonic

antenna," *Nat. Photonics*, vol. 4, no. 7, pp. 484–488, 2010, doi: 10.1038/nphoton.2010.90.

[65] W. A. Challener *et al.*, "Heat-assisted magnetic recording by a near-field transducer with efficient optical energy transfer," *Nat. Photonics*, vol. 3, no. 4, pp. 220–224, 2009, doi: 10.1038/nphoton.2009.26.

[66] M. C. Kautzky and M. G. Blaber, "Materials for heat-assisted magnetic recording heads," *MRS Bull.*, vol. 43, no. 2, pp. 100–105, 2018, doi: 10.1557/mrs.2018.1.

[67] N. Zhou *et al.*, "Plasmonic near-field transducer for heat-assisted magnetic recording," *Nanophotonics*, vol. 3, no. 3, pp. 141–155, 2014, doi: 10.1515/nanoph-2014-0001.

[68] B. D. Terris, H. J. Mamin, and D. Rugar, "Optical data storage using a solid immersion lens," *Optoelectron. - Devices Technol.*, vol. 10, no. 3, pp. 303–310, 1995.

[69] S. M. Mansfield and G. S. Kino, "Solid immersion microscope," *Appl. Phys. Lett.*, vol. 57, no. 24, pp. 2615–2616, 1990, doi: 10.1063/1.103828.

[70] M. Shinoda, K. Saito, T. Kondo, T. Ishimoto, and A. Nakaoki, "High-density near-field readout over 50 GB capacity using solid immersion lens with high refractive index," *Japanese J. Appl. Physics, Part 1 Regul. Pap. Short Notes Rev. Pap.*, vol. 42, no. 2 B, pp. 1101–1104, 2003, doi: 10.1143/jjap.42.1101.

[71] B. H. A, "Theory of Diffraction by Small Holes," *Phys. Rev. JOURNALS*, 1944, doi: https://doi-org.ezp1.lib.umn.edu/10.1103/PhysRev.66.163.

[72] "https://en.wikipedia.org/wiki/Surface_plasmon." .

[73] L. Shi *et al.*, "Evaluating broader impacts of nanoscale thermal transport research," *Nanoscale Microscale Thermophys. Eng.*, vol. 19, no. 2, pp. 127–165, 2015, doi: 10.1080/15567265.2015.1031857.

[74] C. Peng, "Surface-plasmon resonance of a planar lollipop near-field transducer," *Appl. Phys. Lett.*, vol. 94, no. 17, pp. 10–13, 2009, doi: 10.1063/1.3126483.

[75] D. Weller, O. Mosendz, G. Parker, S. Pisana, and T. S. Santos, "L10 FePtX-Y media for heat-assisted magnetic recording," *Phys. Status Solidi Appl. Mater. Sci.*, vol. 210, no. 7, pp. 1245–1260, 2013, doi: 10.1002/pssa.201329106.

[76] M. H. Kryder *et al.*, "Heat Assisted Magnetic Recording," vol. 96, no. 11, 2008.

[77] J. Lyubina, B. Rellinghaus, O. Gutfleisch, and M. Albrecht, *Handbook of Magnetic Materials*. Elsevier B.V., 2011.

[78] T. Klemmer, D. Hoydick, H. Okumura, B. Zhang, and W. A. Soffa, "Magnetic Hardening and Coercitiy in $L1_0$ ordered FePd Ferromagents," vol. 33, pp. 1793–1805, 1995.

[79] D. Weller *et al.*, “High ku materials approach to 100 gbits/in2,” *IEEE Trans. Magn.*, vol. 36, no. 1 PART 1, pp. 10–15, 2000, doi: 10.1109/20.824418.

[80] K. Barmak, J. Kim, S. Shell, E. B. Svedberg, and J. K. Howard, “Calorimetric studies of the A1 to L10 transformation in FePt and CoPt thin films,” *Appl. Phys. Lett.*, vol. 80, no. 22, pp. 4268–4270, 2002, doi: 10.1063/1.1483924.

[81] J. Zhu, P. Quarterman, and J. P. Wang, “Ion-Assisted Plasma Etch Modeling of L10 Phase FePt Magnetic Media Fabrication with Embedded Mask Patterning Method,” *IEEE Trans. Magn.*, vol. 51, no. 11, pp. 6–10, 2015, doi: 10.1109/TMAG.2015.2438061.

[82] J. Zhu, P. Quarterman, and J. P. Wang, “Effect of Mask Erosion on Patterning of FePt for Heat-Assisted Magnetic Recording Media Using Embedded Mask Patterning,” *IEEE Trans. Magn.*, vol. 52, no. 7, 2016, doi: 10.1109/TMAG.2016.2517016.

[83] L. Huang *et al.*, “HAMR thermal modeling including media hot spot,” *IEEE Trans. Magn.*, vol. 49, no. 6, pp. 2565–2568, 2013, doi: 10.1109/TMAG.2013.2252886.

[84] D. Weller and A. Moser, “Thermal effect limits in ultrahigh-density magnetic recording,” *IEEE Trans. Magn.*, vol. 35, no. 6, pp. 4423–4439, 1999, doi: 10.1109/20.809134.

[85] E. Sallica Leva, R. C. Valente, F. Martínez Tabares, M. Vásquez Mansilla, S. Roshdestwensky, and A. Butera, “Magnetic domain crossover in FePt thin films,” *Phys. Rev. B - Condens. Matter Mater. Phys.*, vol. 82, no. 14, 2010, doi: 10.1103/PhysRevB.82.144410.

[86] H. N. Bertram, M. Marrow, J. Ohno, and J. K. Wolf, “Analysis of DC noise in thin film media,” *IEEE Trans. Magn.*, vol. 40, no. 4 II, pp. 2311–2313, 2004, doi: 10.1109/TMAG.2004.833171.

[87] W. F. Brown Jr, “Thermal Fluctuations of a Single Domain Particle,” *Phys. Rev.*, vol. 130, no. 5, 1963.

[88] R. H. Victora and A. Ghoreyshi, “Optical Analysis of HAMR Media,” *IEEE Trans. Magn.*, vol. 55, no. 3, 2019, doi: 10.1109/TMAG.2018.2869662.

[89] “https://en.wikipedia.org/wiki/Shot_noise.” .

[90] “https://hal.archives-ouvertes.fr/jpa-00235996/document.” .

[91] K. H, *Handbook of Magnetism and Advanced Magnetic Materials*. John Wiley & Sons, 2007.

[92] D. V Berkov, *Handbook of Magnetism and Advanced Magnetic Materials*. John Wiley & Sons, 2007.

[93] T. Qu and R. H. Victora, “Dependence of Kambersky damping on Fermi level and spin orientation,” *J. Appl. Phys.*, vol. 115, no. 17, p. 17C506, 2014, doi: 10.1063/1.4863264.

[94] “https://www.iue.tuwien.ac.at/phd/makarov/dissertationch5.html.” .

[95] “https://en.wikipedia.org/wiki/Runge-Kutta_methods.” .

[96] J. L. García-Palacios and F. J. Lázaro, “Langevin-dynamics study of the dynamical properties of small magnetic particles,” *Phys. Rev. B - Condens. Matter Mater. Phys.*, vol. 58, no. 22, pp. 14937–14958, 1998, doi: 10.1103/PhysRevB.58.14937.

[97] G. D. Fuchs *et al.*, “Adjustable spin torque in magnetic tunnel junctions with two fixed layers,” *Appl. Phys. Lett.*, vol. 86, no. 15, pp. 1–3, 2005, doi: 10.1063/1.1899764.

[98] G. Finocchio, B. Azzerboni, G. D. Fuchs, R. A. Buhrman, and L. Torres, “Micromagnetic modeling of magnetization switching driven by spin-polarized current in magnetic tunnel junctions,” *J. Appl. Phys.*, vol. 101, no. 6, 2007, doi: 10.1063/1.2496202.

[99] P. W. Huang, “Micromagnetic study of heat assisted magnetic recording using renormalized media cells,” University of Minnesota, 2014.

[100] A. Munshi, B. Gaster, T. Mattson, J. Fung, and D. Ginsburg, *OpenCL Programming Guide*. Addison-Wesley Professional, 2011.

[101] D. R. V. L. B. Thambawita, R. Ragel, and D. Elkaduwe, “To use or not to use: Graphics processing units (GPUs) for pattern matching algorithms,” *2014 7th Int. Conf. Inf. Autom. Sustain. "Sharpening Futur. with Sustain. Technol. ICIAfS 2014*, no. February 2015, pp. 1–5, 2014, doi: 10.1109/ICIAFS.2014.7069585.

[102] J. Barker, R. F. L. Evans, R. W. Chantrell, D. Hinzke, and U. Nowak, “Atomistic spin model simulation of magnetic reversal modes near the Curie point,” *Appl. Phys. Lett.*, vol. 97, no. 19, pp. 1–4, 2010, doi: 10.1063/1.3515928.

[103] T. W. McDaniel, “Application of Landau-Lifshitz-Bloch dynamics to grain switching in heat-assisted magnetic recording,” *J. Appl. Phys.*, vol. 112, no. 1, 2012, doi: 10.1063/1.4733311.

[104] R. H. Victora and P. W. Huang, “Simulation of heat-assisted magnetic recording using renormalized media cells,” *IEEE Trans. Magn.*, vol. 49, no. 2, pp. 751–757, 2013, doi: 10.1109/TMAG.2012.2219300.

[105] X. Feng and P. B. Visscher, “Coarse-graining Landau-Lifshitz damping,” *J. Appl. Phys.*, vol. 89, no. 11, pp. 6988–6990, 2001, doi: 10.1063/1.1355328.

[106] R. F. L. Evans, “ATOMISTIC MODELLING OF NANOGRANULAR MAGNETIC MATERIALS,” University of York, 2008.

[107] O. N. Mryasov, U. Nowak, K. Y. Guslienko, and R. W. Chantrell, "Temperature-dependent magnetic properties of FePt: Effective spin Hamiltonian model," *Europhys. Lett.*, vol. 69, no. 5, pp. 805–811, 2005, doi: 10.1209/epl/i2004-10404-2.

[108] Y. Jiao, Z. Liu, and R. H. Victora, "Renormalized anisotropic exchange for representing heat assisted magnetic recording media," *J. Appl. Phys.*, vol. 117, no. 17, 2015, doi: 10.1063/1.4916184.

[109] D. Weller *et al.*, "A HAMR media technology roadmap to an areal density of 4 Tb/in2," *IEEE Trans. Magn.*, vol. 50, no. 1, 2014, doi: 10.1109/TMAG.2013.2281027.

[110] M. L. Yan, Y. F. Xu, X. Z. Li, and D. J. Sellmyer, "Highly (001)-oriented Ni-doped L1 0 FePt films and their magnetic properties," *J. Appl. Phys.*, vol. 97, no. 10, pp. 11–14, 2005, doi: 10.1063/1.1855271.

[111] J. U. Thiele, K. R. Coffey, M. F. Toney, J. A. Hedstrom, and A. J. Kellock, "Temperature dependent magnetic properties of highly chemically ordered Fe55-xNixPt45L10 films," *J. Appl. Phys.*, vol. 91, no. 10, pp. 6595–6600, 2002, doi: 10.1063/1.1470254.

[112] T. Ono *et al.*, "Experimental investigation of off-stoichiometry and 3d transition metal (Mn, Ni, Cu)-substitution in single-crystalline FePt thin films," *AIP Adv.*, vol. 6, no. 5, pp. 6–11, 2016, doi: 10.1063/1.4943535.

[113] N. A. Natekar, W.-H. Hsu, and R. H. Victora, "Calculated dependence of FePt damping on external field magnitude and direction," *AIP Adv.*, vol. 7, no. 5, 2017, doi: 10.1063/1.4973800.

[114] S. Serrano-Guisan, K. Rott, G. Reiss, and H. W. Schumacher, "Inductive and magneto-resistive measurements of Gilbert damping in Ni 81Fe19 thin films and microstructures," *J. Phys. D. Appl. Phys.*, vol. 41, no. 16, 2008, doi: 10.1088/0022-3727/41/16/164015.

[115] T. Qu and R. H. Victora, "Effect of substitutional defects on Kambersky damping in L10 magnetic materials," *Appl. Phys. Lett.*, vol. 106, no. 7, pp. 0–5, 2015, doi: 10.1063/1.4909510.

[116] W. C. Lin, J. G. Zhu, Y. Wang, and M. Seigler, "Precise measurement of the transition curvature in magnetic recording," *IEEE Trans. Magn.*, vol. 47, no. 10, pp. 2977–2980, 2011, doi: 10.1109/TMAG.2011.2157905.

[117] J. G. Zhu and H. Li, "Write head field design for correcting transition curvature in heat assisted magnetic recording," *AIP Adv.*, vol. 7, no. 5, pp. 1–6, 2017, doi: 10.1063/1.4976733.

[118] J. G. J. Zhu and H. Li, "Correcting Transition Curvature in Heat-Assisted Magnetic Recording," *IEEE Trans. Magn.*, vol. 53, no. 2, 2017, doi:

10.1109/TMAG.2016.2614836.

[119] Z. Liu *et al.*, “Curvature and Skew in Heat-Assisted Magnetic Recording,” *IEEE Trans. Magn.*, vol. 55, no. 3, 2019, doi: 10.1109/TMAG.2018.2868128.

[120] C. M. Chow and J. A. Bain, “A split-pole-gapped NFT write head design for transition curvature reduction in heat-assisted magnetic recording,” *IEEE Trans. Magn.*, vol. 54, no. 11, pp. 2018–2021, 2018, doi: 10.1109/TMAG.2018.2835311.

[121] O. Muthsam, C. Vogler, F. Bruckner, and D. Suess, “Write head design for curvature reduction in heat-assisted magnetic recording by topology optimization,” *J. Appl. Phys.*, vol. 126, no. 14, 2019, doi: 10.1063/1.5123556.

[122] R. H. Victora, S. M. Morgan, K. Momsen, E. Cho, and M. F. Erden, “Two-dimensional magnetic recording at 10 Tbits/in 2,” *IEEE Trans. Magn.*, vol. 48, no. 5 PART 1, pp. 1697–1703, 2012, doi: 10.1109/TMAG.2011.2173310.

[123] “https://en.wikipedia.org/wiki/Voronoi_diagram.” .

[124] “https://mathworld.wolfram.com/VoronoiDiagram.html.” .

[125] “https://en.wikipedia.org/wiki/Pseudorandom_binary_sequence.” .

[126] S. Hernandez *et al.*, “Data Rate Effects on Transition and Remanence Noise in a Modeled Heat-Assisted Magnetic Recording System,” *IEEE Trans. Magn.*, vol. 53, no. 11, pp. 19–22, 2017, doi: 10.1109/TMAG.2017.2701202.

[127] Y. Jiao and R. H. Victora, “Dependence of Predicted Areal Density on Common Optimization Strategies for Heat-Assisted Magnetic Recording,” *IEEE Magn. Lett.*, vol. 8, pp. 30–33, 2017, doi: 10.1109/LMAG.2017.2719625.

[128] S. Hernandez *et al.*, “Using Ensemble Waveform Analysis to Compare Heat Assisted Magnetic Recording Characteristics of Modeled and Measured Signals,” *IEEE Trans. Magn.*, vol. 53, no. 2, 2017, doi: 10.1109/TMAG.2016.2612230.

[129] C. H. Hee, Y. Y. Zou, and J. P. Wang, “Tilted media by micromagnetic simulation: A possibility for the extension of longitudinal magnetic recording?,” *J. Appl. Phys.*, vol. 91, no. 10 I, pp. 8004–8006, 2002, doi: 10.1063/1.1447497.

[130] K. Z. Gao and H. N. Bertram, “Magnetic recording configuration for densities beyond 1 Tb/in2 and data rates beyond 1 Gb/s,” *IEEE Trans. Magn.*, vol. 38, no. 6, pp. 3675–3683, 2002, doi: 10.1109/TMAG.2002.804801.

[131] R. H. Victora and S. Xiao, “Composite media for perpendicular magnetic recording,” *IEEE Trans. Magn.*, vol. 41, no. 2, pp. 537–542, doi: 10.1109/TMAG.2004.838075.

[132] J. Lohau, A. Moser, D. T. Margulies, E. E. Fullerton, and M. E. Schabes, “Dynamic coercivity measurements of antiferromagnetically coupled magnetic media layers,” *Appl. Phys. Lett.*, vol. 78, no. 18, pp. 2748–2750, 2001, doi:

10.1063/1.1369391.

[133] A. Inomata, E. N. Abarra, B. R. Acharya, A. Ajan, and I. Okamoto, “Improved thermal stability of synthetic ferrimagnetic media with enhanced exchange coupling strength,” *Appl. Phys. Lett.*, vol. 80, no. 15, pp. 2719–2721, 2002, doi: 10.1063/1.1467696.

[134] M. Kapoor, X. Shen, and R. H. Victora, “Effect of intragranular exchange on exchange-coupled composite media,” *J. Appl. Phys.*, vol. 99, no. 8, 2006, doi: 10.1063/1.2163850.

[135] J. P. Wang, W. K. Shen, J. M. Bai, R. H. Victora, J. H. Judy, and W. L. Song, “Composite media (dynamic tilted media) for magnetic recording,” *Appl. Phys. Lett.*, vol. 86, no. 14, pp. 1–3, 2005, doi: 10.1063/1.1896431.

[136] W. K. Shen and J. P. Wang, “Ferromagnetic interlayer coupling and switching process of exchange coupled composite media,” *J. Appl. Phys.*, vol. 100, no. 9, pp. 14–17, 2006, doi: 10.1063/1.2374931.

[137] J. U. Thiele, S. Maat, and E. E. Fullerton, “FeRh/FePt exchange spring films for thermally assisted magnetic recording media,” *Appl. Phys. Lett.*, vol. 82, no. 17, pp. 2859–2861, 2003, doi: 10.1063/1.1571232.

[138] J. U. Thiele, S. Maat, J. L. Robertson, and E. E. Fullerton, “Magnetic and structural properties of FePt-FeRh exchange spring films for thermally assisted magnetic recording media,” *IEEE Trans. Magn.*, vol. 40, no. 4 II, pp. 2537–2542, 2004, doi: 10.1109/TMAG.2004.829325.

[139] D. Suess, “Micromagnetics of exchange spring media: Optimization and limits,” *J. Magn. Magn. Mater.*, vol. 308, no. 2, pp. 183–197, 2007, doi: 10.1016/j.jmmm.2006.05.021.

[140] Z. Liu and R. H. Victora, “Composite Structure With Superparamagnetic Writing Layer for Heat-Assisted Magnetic Recording,” vol. 52, no. 7, pp. 18–21, 2016.

[141] Z. Liu, Y. Jiao, and R. H. Victora, “Composite media for high density heat assisted magnetic recording,” *Appl. Phys. Lett.*, vol. 108, no. 23, 2016, doi: 10.1063/1.4953231.

[142] N. A. Natekar, Z. Liu, S. Hernandez, and R. H. Victora, “SNR improvement by variation of recording and media parameters for a HAMR exchange coupled composite media,” *AIP Adv.*, vol. 8, no. 5, 2018, doi: 10.1063/1.5007072.

[143] Y. Jiao, Y. Wang, and R. H. Victora, “A Study of SNR and BER in Heat-Assisted Magnetic Recording,” *IEEE Trans. Magn.*, vol. 51, no. 11, pp. 18–21, 2015, doi: 10.1109/TMAG.2015.2451135.

[144] Y. Wang and V. Bhagavatula, “Improving BER performance by using V-shaped read head array in heat assisted magnetic recording,” *2017 IEEE Int. Magn. Conf. INTERMAG 2017*, vol. 53, no. 11, 2017, doi: 10.1109/INTMAG.2017.8007759.

[145] S. Bhargava and E. Yablonovitch, “Lowering HAMR near-field transducer temperature via inverse electromagnetic design,” *IEEE Trans. Magn.*, vol. 51, no. 4, pp. 1–7, 2015, doi: 10.1109/TMAG.2014.2355215.

[146] J. D. Kiely *et al.*, “Write-Induced Head Contamination in Heat-Assisted Magnetic Recording,” *IEEE Trans. Magn.*, vol. 53, no. 2, 2017, doi: 10.1109/TMAG.2016.2618842.

[147] J. D. Kiely *et al.*, “Media roughness and head-media spacing in heat-assisted magnetic recording,” *IEEE Trans. Magn.*, vol. 50, no. 3, pp. 132–136, 2014, doi: 10.1109/TMAG.2013.2291684.

[148] S. Xiong *et al.*, “Setting Write Spacing in Heat Assisted Magnetic Recording,” *IEEE Trans. Magn.*, vol. 54, no. 8, 2018, doi: 10.1109/TMAG.2018.2841367.

[149] N. A. Natekar, W. Tipcharoen, and R. H. Victora, “Composite media with reduced write temperature for heat assisted magnetic recording,” *J. Magn. Magn. Mater.*, vol. 486, 2019, doi: 10.1016/j.jmmm.2019.165253.

[150] Z. Liu, P. W. Huang, G. Ju, and R. H. Victora, “Reduction of recording noise caused by nano-scale variations in Curie temperature,” *Appl. Phys. Lett.*, vol. 114, no. 7, 2019, doi: 10.1063/1.5080559.

[151] B. F. Valcu and N. H. Yeh, “Jitter in a voronoi pattern media-effect of grain size distribution and reader width,” *IEEE Trans. Magn.*, vol. 46, no. 6, pp. 2160–2162, 2010, doi: 10.1109/TMAG.2010.2042794.

[152] X. Wang and H. N. Bertram, “Simple transition parameter expression including grain size and intergranular exchange,” *J. Appl. Phys.*, vol. 93, no. 10 2, pp. 7005–7007, 2003, doi: 10.1063/1.1540139.

[153] M. P. Sharrock, “Time dependence of switching fields in magnetic recording media (invited),” *J. Appl. Phys.*, vol. 76, no. 10, pp. 6413–6418, 1994, doi: 10.1063/1.358282.

[154] Z. Liu, P. W. Huang, G. Ju, and R. H. Victora, “Thermal switching probability distribution of L10 FePt for heat assisted magnetic recording,” *Appl. Phys. Lett.*, vol. 110, no. 18, 2017, doi: 10.1063/1.4983033.

[155] J. Hohlfeld, P. Czoschke, P. Asselin, and M. Benakli, “Improving Our Understanding of Measured Jitter (in HAMR),” *IEEE Trans. Magn.*, vol. 55, no. 3, 2019, doi: 10.1109/TMAG.2018.2872758.

[156] N. A. Natekar and R. H. Victora, “Analytical Estimation of Transition Jitter for the Heat-Assisted Magnetic Recording Process,” *IEEE Magn. Lett.*, vol. 11, pp. 1–4, 2020, doi: 10.1109/lmag.2020.2992221.

[157] A. Hara, H. Muraoka, and S. J. Greaves, “Write synchronization for position-correlated granular media,” *J. Appl. Phys.*, vol. 117, no. 17, pp. 1–5, 2015, doi: 10.1063/1.4916497.

[158] R. Ahmed, M. F. Erden, P. Krivosik, and R. H. Victora, “HAMR Versus PMR: A Comparative Study of Signal-Noise Performance,” *IEEE Trans. Magn.*, vol. 55, no. 12, 2019, doi: 10.1109/TMAG.2019.2935400.

[159] N. H. Yeh, X. Wu, and T. Roscamp, “Jitter analysis and cross-track correlation length extraction through nonlinear noise scaling with reader width,” *IEEE Trans. Magn.*, vol. 50, no. 11, pp. 50–53, 2014, doi: 10.1109/TMAG.2014.2321002.

[160] J. G. Zhu and H. Li, “Understanding signal and noise in heat assisted magnetic recording,” *IEEE Trans. Magn.*, vol. 49, no. 2, pp. 765–772, 2013, doi: 10.1109/TMAG.2012.2231855.

[161] J. D. Kiely, P. M. Jones, and J. Hoehn, “Materials challenges for the heat-assisted magnetic recording head-disk interface,” *MRS Bull.*, vol. 43, no. 2, pp. 119–124, 2018, doi: 10.1557/mrs.2018.4.

[162] S. Kalarickal, A. Tsoukatos, S. Hernandez, C. Hardie, and E. Gage, “Adjacent Track Interference in Heat-Assisted Magnetic Recording: Impact and Implications,” *IEEE Trans. Magn.*, vol. 55, no. 7, 2019, doi: 10.1109/TMAG.2019.2897949.

[163] C. Rea *et al.*, “High Track Pitch Density for HAMR Recording: 1M TPI,” *IEEE Trans. Magn.*, vol. 55, no. 3, pp. 1–8, 2019, doi: 10.1109/TMAG.2018.2867153.

[164] T. Rausch *et al.*, “Recording performance of a pulsed HAMR Architecture,” *IEEE Trans. Magn.*, vol. 51, no. 4, 2015, doi: 10.1109/TMAG.2014.2355173.

[165] B. Xu, H. Wang, Z. Cen, and Z. Liu, “Short-Pulse Laser Heating,” vol. 51, no. 6, pp. 1–5, 2015.

[166] B. Xu *et al.*, “Simulation Study of Pulse Laser Quality Effects on Recording Performances of Heat-Assisted Magnetic Recording by Short-Pulse Laser Heating,” *IEEE Trans. Magn.*, vol. 51, no. 11, 2015, doi: 10.1109/TMAG.2015.2438311.